CENTRO BRASILEIRO DE PESQUISAS FÍSICAS

Coordenação de Física Experimental de Altas Energias

Dissertation presented
as a partial requirement for the degree of
Doctor of Science

Measurement of the Muon Neutrino Double-Differential Charged Current Quasi-Elastic Like Cross Section on a Hydrocarbon Target at $E_\nu \sim 3.5$ GeV

Presented by

Kenyi Paolo Hurtado Anampa

Rio de Janeiro, Brazil

August 2014

Dedicated to my wife, Angela, and our daugther, Amelie
for always being there to support, cheer and love me
no matter what...

Acknowledgements

Even though only my name appears on the cover of this dissertation, there is a lot of people and institutions who have contributed in one way or another to its production. First of all, I would like to thank my thesis advisor Hélio da Motta and my supervisor at Fermilab Jorge Morfin for their continuous guidance and support from the very first day. My sincere thanks and gratitude to my closer collaborator in this work, Jyotsna Osta, not only for her crucial and significant contributions in this analysis, but also for always going above and beyond the call of duty. It has been a pleasure to work with you. Special thanks and acknowledgments to Deborah Harris and Kevin McFarland, the spokespersons of MINERνA , for their constant dedication to the success of the experiment. Also, many thanks to my former Institution: Universidad Nacional de Ingeniería (UNI) and to professor Javier Solano, who introduced me and gave me the opportunity to work on the MINERνA experiment during my Master studies, experience that motivated me to continue on this path pursuing a doctorate degree.

I would like to thank the US Fermi National Accelerator Laboratory for all the support that helped making this work possible.

Many thanks to all MINERνA and CBPF collaborators, especially Arturo Fiorentini, whose work has been enlightening for the realization of this one.

This work has been possible thanks to a scholarship from the Brazilian Federal Agency CAPES received between 2010 and 2014.

Finally, my deepest gratitude to my wife Angela Coaguila, who has always being with me through thick and thin, no matter how difficult. During these years, we have not only grown as a couple but also become parents of a wonderful little girl, our dear Amelie.

Abstract

The MINERνA Experiment (Main Injector Experiment $\nu - A$ interaction) [1] is a highly segmented detector of neutrinos, able to record events with high precision (over than thirteen million event in a four year run), using the NuMI Beam (Neutrino Main Injector) at the Fermi National Accelerator Laboratory [2].

This thesis presents a measurement of the Charged Current Quasi-Elastic Like[1] ν_μ interaction on polystyrene scintillator (CH) in the MINERνA experiment with neutrino energies between 1.5 and 10 GeV. We use data taken between[2] March 2010 and April 2012. The interactions were selected by requiring a negative muon, a reconstructed and identified proton, no michel electrons in the final state (in order to get rid of soft pions decaying) and a low calorimetric recoil energy away from the interaction vertex. The analysis is performed on 66,214 quasi-elastic like event candidates in the detectors tracker region with an estimated purity of 74%.

The final measurement reported is a double differential cross sections in terms of the muon longitudinal and transversal momentum observables.

[1] See Quasi-Elastic Like definition in Section 6.2

[2] Figure 6.1 shows the MINERνA data run periods.

Resumo

O Experimento MINERνA (Main Injector Experiment $\nu - A$ interaction) [1] é um detector de neutrinos altamente segmentado, capaz de registrar eventos com alta precisão (mais de treze millões de eventos em quatro anos), usando o feixe NuMI (Neutrino Main Injector) no Fermi National Accelerator Laboratory [2].

Esta tese apresenta a medida de seção de choque de interações tipo quase-elástica[3] de ν_μ em cintilador de poliestireno (CH) no experimento MINERνA com neutrinso de energia entre 1,5 e 10 GeV. Os dados foram coletados entre[4] março de 2010 e abril de 2012. Foram selecionados eventos com a presença de um múon negativo, um próton identificado e reconstruído, sem elec-trons de Michel no estado final (para excluir píons decaindo) e um corte na energia de recuo longe do vértice. A análise foi feita com 66.214 eventos candidatos na região do rastreador do detector com uma puresa estimada em 74%.

A medida final reportada é uma seção de choque diferencial dupla em função dos momenta longitudinal e transversal do múon.

[3] Ver definição na Seção 6.2

[4] A Figura 6.1 mostra os diversos períodos de tomada de dados do MINERνA .

MINERνA Collaboration

K. Hurtado[1,20], P. Rodriguez[16], I.Albayrak[7], L. Aliaga[21], M. Andrews[5], S. Avvakumov[16], S. Angelidakis[2], Baldin[5], G. Blazey[12], A.Butkevich[8], A. Bodek[16], D. Boehnlein[5], S. Boyd[14], R. Bradford[16], W.K. Brooks[10], A. Bruell[10], D. Buchholtz[13], H. Budd[16], D. Casper[3], C. Castromonte[1], D. Cherdack[19], M.E. Christy[7], J. Chvojka[16], E. Valencia[6], M.A.C. Cummings[12], A.Chamorro[20], D.S. Damiani[21], S. Dytman[14], R.DeMaat[5], R. Ent[10], B.Eberly[14], G.A.Fiorentini[1], J. Felix[6], R. Flight[16], A. Gago[15], H. Gallagher[19], D. Gaskell[10], R. Gilman[17], C. Gingu[5], R. Gran[11], B. Gobbi[12], J. Grange[22], R. Gutierrez[6], N. Grossman[5], D. A. Harris[5], A. Higuera[6], J. Hobbs[12], T. Kafka[19], C.E Keppel[7], J. Kilmer[5], Kopp[18], S.Kulagin[8], G. Kumbartzki[17], M. Kordosky[21], L. Loiacono[18], H. Lee[16], A. Leister[21], S. Manly[16], E. Maher[23], W.A. Mann[19], K. McFarland[16], D. Meekins[10], W. Melnitchouk[10], A. Mislivec[16], G. Moreno[6], J.G. Morfin[5], J. Moussau[22], H. da Motta[1], D. Naples[14], J.K. Nelson[21], G. Niculescu[9], L. Rakotondravohitra[5], D.M Caicedo[1], I. Niculescu[9], W. Oliver[19], B. Osmanov[22], J.Palomino[1], V. Paolone[14], J. Park[16], L. Patrick[13], G. Perdue[16], E. Paschos[4], C. Perez[15], A. Pla-Dalmau[5], M. Proga[18], R. Ransome[17], M. A. Reyes[6], C. Romero[20], C. Rude[11], P. Rubinov[5], H. Ray[22], P. Shanahan[5], H. Schellman[13], E. Schulte[17], C. Simon[3], C. J. Solano[20], P. Stamoulis[2], D. Schmitz[25], N. Tagg[24], G. Tzanakos[2], Z. Urrutia[6], M. Vaz[1], T. Walton[7], S. Wood[10], G. Zavala[6], B. Ziemer[3]

Centro Brasileiro de Pesquisas Fisicas, Rio de Janeiro, Brazil[1]
University of Athens, Athens, Greece[2]
University of California, Irvine, California[3]
University of Dortmund, Dortmund, Germany[4]
Fermi National Accelerator Laboratory, Batavia, Illinois[5]
Universidad de Guanajuato, Guanajuato, Mexico[6]
Hampton University, Hampton, Virginia[7]
Institute for Nuclear Research, Moscow, Russia[8]
James Madison University, Harrisonburg, Virginia[9]
Jefferson Lab, Newport News, Virginia[10]
University of Minnesota Duluth, Duluth, Minnesota[11]
Northern Illinois University, DeKalb, Illinois[12]
Northwestern University, Evanston, IL[13]
University of Pittsburgh, Pittsburgh, Pennsylvania[14]
Pontificia Universidad Catolica del Peru, Lima, Peru[15]
University of Rochester, Rochester, New York[16]
Rutgers University, New Brunswick, New Jersey[17]
University of Texas-Austin, Texas[18]
Tufts University, Medford, Massachusetts[19]
Universidad Nacional de Ingenieria, Lima, Perú[20]
William and Mary College, Williamsburg, Virginia[21]
University of Florida, Gainesville, Florida[22]
Massachusetts College of Liberal Arts, North Adams, Massachusetts[23]
Otterbein College, Westerville, Ohio[24]
University of Chicago, Ilinois[25]

Contents

Acknowledgements **ii**

Abstract **iii**

Resumo **iv**

MINERνA Collaboration **v**

1 Introduction **2**

2 Neutrinos **4**

2.1 Introduction 4

2.1.1 Neutrino Flavors 6

2.1.2 Helicity 6

2.1.3 Solar Neutrinos 6

2.1.4 Atmospheric Neutrinos 7

2.2 Neutrinos in the Standard Model 9

2.3 Neutrino Mass 11

2.4 Neutrino Oscillations 13

2.5 Neutrino Interactions 14

2.5.1 Deep Inelastic Scattering 15

2.5.2 Resonance Production 16

2.5.2.1 Resonance Single Pion Production 16

2.5.3 Coherent Pion Production 17

2.5.4 Quasi-Elastic Scattering 18

2.5.4.1 Charged Current Quasi-Elastic Scattering . . . 18
2.6 Short Range Correlations . . . 20
2.7 Meson Exchange Currents . . . 21
2.8 Analysis Motivation . . . 21

3 The MINERvA Experiment **25**
3.1 General Description of the Experiment . . . 25
3.2 The NuMI Neutrino Beam . . . 25
3.3 The MINERvA Detector . . . 26
3.4 The Inner Detector . . . 27
3.4.1 The Nuclear Targets . . . 27
3.4.2 The Tracker Region . . . 29
3.4.3 Electromagnetic Calorimeters . . . 29
3.4.4 Downstream Hadronic Calorimeter . . . 31
3.5 The Outer Detector . . . 31
3.6 Electronics and DAQ (Data Acquisition) . . . 32
3.6.1 Detector Readout . . . 32
3.6.2 The Data Acquisition System . . . 33

4 Simulation **35**
4.1 The NuMI Flux . . . 35
4.1.1 Hadron Production Reweighting . . . 36
4.2 Neutrino Cross Section Models (GENIE) . . . 39
4.2.1 Quasi-Elastic Scattering . . . 39
4.2.2 Resonance Scattering . . . 40
4.2.3 Coherent Scattering . . . 41
4.2.4 Deep Inelastic Scattering . . . 41
4.2.5 Transition region to DIS . . . 42
4.2.6 Hadron Production . . . 42
4.3 Nuclear Effects . . . 43
4.3.1 Relativistic Fermi Gas Model . . . 43
4.3.2 Final State Interactions . . . 44

5 Event Reconstruction **46**
5.1 Introduction . . . 46
5.2 Classification of hits . . . 46
5.2.1 Clustering by Time . . . 47

5.2.2 Clustering by Position . . . 47
5.2.3 Tracking . . . 48
5.2.3.1 The Tracking Procedure . . . 49
5.2.3.2 The LongTracker . . . 49
5.2.3.3 The Short Trackers . . . 51
5.3 Muon Reconstruction . . . 52
5.4 Proton Reconstruction . . . 53
5.5 Michel Electrons Reconstruction . . . 55
5.6 Recoil Energy Reconstruction . . . 55

6 Event Sample and Selection 58
6.1 Event Sample . . . 58
6.1.1 Monte Carlo . . . 58
6.1.2 Data Set . . . 59
6.2 The Quasi-Elastic Like Signal . . . 60
6.3 Event Selection . . . 60
6.3.1 Fiducial Volume . . . 60
6.3.2 MINOS Matching . . . 61
6.3.3 Insensitive Electronic Regions in Detector . . . 62
6.3.4 Neutrino Helicity . . . 62
6.3.5 Event Multiplicity . . . 62
6.3.6 Primary Proton Identification . . . 63
6.3.7 Secondary Proton Identification . . . 64
6.3.8 Isolated Blobs . . . 64
6.3.9 Michel Electrons . . . 65
6.3.10 Neutrino Energy . . . 65
6.3.11 Recoil Away From The Interaction Vertex . . . 66

7 The Double Differential Cross Section Measurement 71
7.1 Introduction . . . 71
7.2 Background Tuning and Subtraction . . . 72
7.2.1 Background Tuning . . . 72
7.2.2 Background Subtraction . . . 73
7.3 Unfolding . . . 79
7.3.1 The Smearing Matrix . . . 84
7.3.2 Simple Inversion Matrix . . . 84
7.3.3 The Bayesian Technique . . . 86

7.4 Efficiency and Acceptance Correction . . . 86
7.5 Flux and Target Normalization . . . 88
7.6 Systematic Errors . . . 91
7.6.1 Flux . . . 94
7.6.2 Cross Section and FSI Models . . . 96
7.6.3 Muon Reconstruction . . . 97
7.6.4 Energy Response . . . 97
7.6.5 Proton Reconstruction . . . 97
7.6.5.1 Bethe-Block calculation . . . 98
7.6.5.2 Absolute Energy Scale Constant (MEU) . . . 98
7.6.5.3 Detector Mass Model . . . 98
7.6.5.4 Birk's Law Quenching Parameter . . . 98
7.6.5.5 Other Systematics . . . 99

8 Final Results **100**

9 Conclusions **103**

A Proton Range Score Cut **105**

B Recoil Energy cut to enhance the quasi-elastic-like signal **107**

C Systematic Errors Summaries **110**
C.1 Systematic Error Groups after background subtraction, unfolding and efficiency correction . . . 110
C.2 Systematic Error Group Components in the Cross Section . . . 114

D GENIE model parameters **120**

E Summary of contributions to the MINERνA experiment **123**
E.1 Special Runs . . . 123
E.1.1 Introduction . . . 123
E.1.2 Data Quality Checks . . . 124
E.2 Systematic Errors . . . 125
E.2.1 Many Universes Method . . . 125
E.2.2 The covariance Matrix . . . 125
E.3 Unfolding . . . 126
E.3.1 Introduction . . . 126
E.3.2 Unfolding Methods . . . 127

E.3.2.1 Iterative Bayes' theorem 127
E.3.2.2 Single Value Decomposition 128
E.3.2.3 Bin by Bin 128
E.3.2.4 Simple Inversion 129
E.3.3 Using the UnfoldUtils Tool 129

Bibliography **131**

Glossary **140**

List of Figures

2.1 Leon Lederman, Melvin Schwartz and Jack Steinberger, Nobel prize winners for the discovery of the muon neutrino 5
2.2 The atmospheric neutrino anomaly [35]. 8
2.3 Existing muon neutrino charged-current cross section measurements and predictions as a function of neutrino energy. The contributing processes in this energy region include Quasi-Elastic (QE) scattering, Resonance Production (RES), and Deep Inelastic Scattering (DIS)[43] 15
2.4 (left) Charged and (right) Neutral Current resonance pion production 17
2.5 Flux unfolded $\sigma(E_\nu)$ Data for MiniBoone and NOMAD. 22
2.6 Minerva single differential cross section $d\sigma/dQ^2$ 23
2.7 Constant lines of $E_\nu^{QE}, {Q^2}_{QE}$ values in the muon $P_Z - P_T$ phase space. Events shown here are data events taken from March to July 2010 after passing the selection criteria described in Section 6. 24

3.1 MINERvA installation at the NuMI Hall. 26
3.2 The NuMI main components. 26
3.3 Minerva Detector Schematic 27
3.4 Nuclear Targets position and composition. 28
3.5 One active (tracker) module and its three planes: X,U and V. V and U are rotated ±60 degrees with respect to the X. 29
3.6 Triangular scintillator strips from the inner detector. 30
3.7 View of an ECAL detector module. The figure at right shows a cut-away view from the side. 30

3.8 View of an HCAL detector module. The figure at right shows a cut-away view from the side. 31
3.9 Front End Board schematic design 33

4.1 FTFP_BERT and NA49 data for (left) $pC \rightarrow \pi^+X$ and (right) $pC \rightarrow \pi^-X$ cross sections. 37
4.2 Transverse Momentum vs Feynman x for pi^+, which makes a ν_μ in MINERνA. 38
4.3 Neutrino and anti-neutrino hadron reweight factors 39
4.4 Neutrino and anti-neutrino flux: Corrected (after weights applied) vs Uncorrected (before reweights). 40
4.5 Proton and neutron potential wells and states in the Fermi gas model. E_F^p, E_F^n are the Fermi energy of the proton and neutron respectively. B' is the Binding Energy. 43

5.1 Time distribution of hits in a NuMI beam spill. Colored peaks represent the time slices created. 47
5.2 Resolution of the fitted positions along a track relative to the measured cluster positions for a sample of data rock muons [93]. 51
5.3 dE/dx profiles for an identified proton in data. 54
5.4 Momentum resolution (reconstructed momentum - true momentum) for protons (left) and pions (right) from simulated reconstructed tracks stopping in the detector. 54
5.5 Michel electron energy distribution for data and Montecarlo. 55
5.6 Calorimetric energy resolution for simulated charged-current inclusive neutrino events. The dots show the width of a Gaussian fit to the difference between the measured and true recoil energy divided by the true recoil energy, binned by true recoil energy. The line represents a functional fit, $\sigma/E = 0.134 \oplus 0.290/\sqrt{E}$. . . 57

6.1 Neutrino beam data recoded by MINERνA 59
6.2 Schematic of a quasi-elastic event in the MINERνA detector. The event interaction vertex is inside the fiducial volume, the muon is going into the MINOS Near Detector and the proton is contained in the MINERνA detector. 61
6.3 Multiplicity or number of outgoing tracks (top) and its logY scale version (bottom). 63
6.4 Number of isolated blobs. (a) Events with where only the muon was reconstructed. (b) Events with a muon and at least one proton candidate reconstructed. 65

6.5 Events with at least one michel electron vetoed from the selection.(a) Events with where only the muon was reconstructed. (b) Events with a muon and at least one proton candidate reconstructed. 66
6.6 Recoil Energy cut as a function of Q^2. The plots on the left show the quasi-elastic-like events (blue dots) in this phase space and the plots on the right the background (not quasi-elastic-like events). Events below the solid line are accepted. The dotted line is just a reference above 500 MeV. 67
6.7 Event display candidate after passing all selection criteria. 68
6.8 Muon $P_Z - P_T$ phase space for the $\mu^- + X$ sub-sample after all event selection criteria. 69
6.9 Muon $P_Z - P_T$ phase space for the $\mu^- + p + X$ sub-sample after all event selection criteria. 70

7.1 Data an Monte Carlo templates (left) and their ratios (right) for the $\mu^- + X$ sub-sample as a function of the recoil energy for different regions of P_{T_μ} before fitting. 74
7.2 Data an Monte Carlo templates (left) and their ratios (right) for the $\mu^- + X$ sub-sample as a function of the recoil energy for different regions of P_{T_μ} after fitting. 75
7.3 Data and Monte Carlo templates (left) and their ratios (right) for the $\mu^- + p + X$ sub-sample as a function of the recoil energy for different regions of P_{T_μ} before fitting. 76
7.4 Data an Monte Carlo templates (left) and their ratios (right) for the $\mu^- + p + X$ sub-sample as a function of the recoil energy for different regions of P_{T_μ} after fitting. 77
7.5 Background Weights for both sub-samples as a function of P_{T_μ}. 78
7.6 Muon $P_Z - P_T$ phase space for the $\mu^- + X$ sub-sample with predicted backgrounds. 79
7.7 Muon $P_Z - P_T$ phase space for the $\mu^- + p + X$ sub-sample with predicted backgrounds. 80
7.8 Muon $P_Z - P_T$ phase space for the $\mu^- + X$ sub-sample after background subtraction. 81
7.9 Muon $P_Z - P_T$ phase space for the $\mu^- + p + X$ sub-sample after background subtraction. 82
7.10 Muon $P_Z - P_T$ phase space after background subtraction and merging $\mu^- + X$ and $\mu^- + p + X$ sub-samples. 83
7.11 Smearing Matrix for the Muon $P_Z - P_T$ phase space for Signal (QE-Like) Events. 85

7.12 Zoom on Smearing Matrix: This is showing smearing of the true P_Z bins into the reconstructed P_Z bins in the reconstructed P_T region from: 0.6GeV $\leq P_T <$ 0.8GeV (left) and 0.8GeV $\leq P_T <$ 1.4GeV (right). 85
7.13 Muon $P_Z - P_T$ phase space after unfolding. 87
7.14 Efficiency Correction Histogram for the Muon $P_Z - P_T$ phase space for Signal (QE-Like) Events. 89
7.15 Muon $P_Z - P_T$ phase space after efficiency correction. 90
7.16 Neutrino Energy Flux in GeV. 91
7.17 Muon $P_Z - P_T$ Double differential Cross Section $\frac{d^2\sigma}{dP_{Z_\mu} dP_{T_\mu}}$. 92
7.18 Error summary in Data for Muon P_T and P_Z cross section projections. 95
7.19 NuMI neutrino flux prediction using three different hadronic models. The green arrow represents the maximum spread between the peaks of these models. Plot by M.Kordosky from the MINERνA Collaboration. 96

8.1 Muon $P_Z - P_T$ Double differential Cross Section $\frac{d^2\sigma}{dP_{Z_\mu} dP_{T_\mu}}$ 101

A.1 Proton range score as a function of Q^2. 106

B.1 Recoil Energy Cut for different ranges of Q^2. Events have only one reconstructed muon. 108
B.2 Recoil Energy Cut for different ranges of Q^2. Events have one reconstructed muon and, at least, one reconstructed proton. 109

C.1 Error summary in Data for Muon P_T and P_Z projections after background subtraction 111
C.2 Error summary in Data for Muon P_T and P_Z projections after unfolding 112
C.3 Error summary in Data for Muon P_T and P_Z projections after Efficiency Correction 113
C.4 Predicted neutrino flux error summary for Muon P_T and P_Z projections 114
C.5 Predicted Cross Section Models error summary for Muon P_T and P_Z projections 115
C.6 Predicted Final State Interaction Models error summary for Muon P_T and P_Z projections 116
C.7 Muon Energy, Angle and Normalization (described in section 7.6.5.5) error summaries for Muon P_T and P_Z projections 117
C.8 Systematic uncertainties on the cross section for each particle's source which contributes to the systematic uncertainty on the detector response in the recoil energy for Muon P_T and P_Z projections 118
C.9 Systematic uncertainties due to the various sources that contribute to the proton reconstruction systematic uncertainty for Muon P_T and P_Z projections 119

E.1 Target configuration from low to high energy. 124
E.2 $P_T vs P_Z$ phase space for different special run configurations. 124
E.3 Neutrino energy spectrum for special runs data. 125
E.4 Inclusive ν migration histogram in the tracker 127

List of Tables

3.1 Nuclear target masses and expected event rates in the MINERvA detector. . . . 28

4.1 A summary of the dataset used to constrain the NuMI flux measurement 38

6.1 Proton Range Score vs Q^2 cut. 64

7.1 Corrections to the muon reconstruction efficiency in MINERvA and MINOS. . . 88
7.2 Double differential cross section $d^2\sigma/dP_{Z_\mu}dPT_\mu$ content values ± statistical (systematic) errors. 91
7.3 Detector Energy Response Uncertainties. 97
7.4 Mass thickness uncertainty per material in the tracker fiducial region. 98

8.1 Double differential cross section $d^2\sigma/dP_{Z_\mu}dPT_\mu$ content values ± statistical(systematic) errors. 102

D.1 Cross section model uncertainties 121
D.2 Final State Interaction model uncertainties 122

E.1 A summary of energy configurations with respect to the distance between the target and Horn 1 shown in Figure E.1 123

CHAPTER 1

Introduction

Due to the discovery of neutrino oscillations (a discovery that was considered one of the most important developments in particle physics in the last years), neutrino physics has been a very active field both experimentally and theoretically. However, neutrino interactions with matter are not yet well understood in the energy region, between 1 GeV and 20 GeV, where three processes overlap: charged-current quasi-elastic scattering, resonant pion production and deep inelastic scattering. Neutrino interaction cross section measurements in this energy region are fundamental to understand the behavior and structure of nucleons and nuclei in weak interactions and will also help to minimize systematic uncertainties in current and future neutrino oscillation experiments.

Neutrino physics has entered the stage of precision measurements and several experiments using intense neutrino beams created in high energy particle accelerators were built to allow measurements of neutrino interaction cross sections in detail. One of these experiments is the Main Injector Neutrino Experiment for $\nu - A$ (MINERνA): A neutrino scattering experiment that uses the NuMI neutrino beam at Fermilab.

The MINERνA Experiment (Main Injector Experiment $\nu - A$ interaction) [1] is a highly segmented detector of neutrinos, able to record events with high precision (over than thirteen million event in a four year run), using the NuMI Beam (Neutrino Main Injector) at the Fermi National Accelerator Laboratory [2].

This thesis presents a measurement of the Charged Current Quasi-Elastic Like[1] ν_μ interaction on polystyrene scintillator (CH) in the MINERνA experiment with neutrino energies

[1] See Quasi-Elastic Like definition in Section 6.2

between 1.5 and 10 GeV. The neutrino data analyzed for such purpose was taken between March 2010 and April 2012 (See Figure 6.1). The interactions were selected by requiring a negative muon, a proton reconstructed and identified, no michel electrons in the final state (in order to get rid of soft pions decaying) and a low calorimetric recoil energy away from the interaction vertex. The analysis is performed on 66,214 quasi-elastic like event candidates in the detectors tracker region with an estimated purity of 74%.

The final measurement reported is a double differential cross sections in terms of the muon longitudinal and transversal momentum observables.

Chapter **??** briefly introduces basic and general aspects of neutrino physics. Chapter 3 describes the NuMI beamline and the MINERνA detector. Chapter 4 describes the simulation. Chapter 5 describes the reconstructino of neutrino interactions in the MINERνA detector. Chapter 6 describes selection procedure to obtain the analysis sample. Chapter 7 presents the calculation to obtaing the measurement of the double differential cross section $d^2\sigma/dP_{Z_\mu}dP_{T_\mu}$ together with a description of the systematic errors considered. Chapter 8 presents the results obtained. Finally, chapter 9 summarizes the work done.

We add four appendixes to this thesis. Appendix A shows the proton range score for different ranges of Q^2. Apendix B shows the different efficiency and purity values of recoil energy for different regions of Q^2. Appendix C summarizes the systematic errors. Appendix D summarizes GENIE main reweightable uncertainties.

CHAPTER 2

Neutrinos

2.1 Introduction

Experiments in 1911 by Otto Hahn and Lise Meitner [3], and by James Chadwick in 1914 [4] suggested that the beta decay spectrum was continuous rather than discrete. In 1927, Ellis and Wooster confirmed this result[5]. That is, electrons were ejected from the atom with a range of energies, rather than the discrete amounts of energies that were observed in gamma and alpha decays. This was a problem for nuclear physics at the time, because it indicated that energy was not conserved in the beta decays.

On 4th December 1930, the Austrian physicist Wolfgan Ernst Pauli proposed the neutrinos existence, in his famous letter to the "Dear Radioactive Ladies and Gentlemen" who had gathered in a Physics conference in Tübingen (Germany), in order to explain the apparent contradiction to the law of conservation of energy produced in beta decays. This particle should have a neutral electric charge and be extremely light, reason for which in 1933, Enrico Fermi proposed the name of *neutrino* to this particle, which is the italian equivalent of "little neutral one". Fermi developed a beta decay theory, in which the neutrino played an important role.

Frederick Reines and Clyde Cowan reported the first neutrino evidence in 1956, using a fission reactor as (anti)neutrinos source. The anti-neutrinos interacted with the protons inside a target made of water mixed with cadmium chloride, originating a positron (e^+) and a neutron

Figure 2.1: Leon Lederman, Melvin Schwartz and Jack Steinberger, Nobel prize winners for the discovery of the muon neutrino

(Equation ỉefeq:beta).[1].

$$\overline{\nu}_e + p \rightarrow n + e^+ \tag{2.1}$$

In 1957, the Italian physicist Bruno Pontecorvo formulates a theory of *neutrino oscillations*, showing that neutrino-antineutrino transitions may occur, if different flavors of neutrinos exist [6]. Although such matter-antimatter oscillation has not been observed, this idea formed the foundation for the quantitative theory of neutrino flavor oscillation, which was first developed by Maki, Nakagawa, and Sakata in 1962 [7] and further elaborated by Pontecorvo in 1967 [8]

The muon-neutrino (ν_μ) was discovered in 1962 by a group of scientist of Brookhaven Laboratory and Columbia University, using a proton beam at the Brookhaven's **Alternating Gradient Synchrotron** [9] in order to produce a shower of pions that traveled about 21 meters through a 5 tons wall of steel. In the process, they decayed into muons and neutrinos, but only the neutrinos went through the whole wall, reaching a *spark chamber* detector.

There, the neutrino interaction with the aluminium plates produced a trace of muons that were detected and photographed, demonstrating the muon neutrino existence (ν_μ). Leon Lederman, Melvin Schwartz and Jack Steinberger won the Nobel prize for this discovery (see Figure 2.1).

In 1973, a group at CERN [10], used a buble chamber (Gargamelle) with a muon neutrino beam produced by the CERN Proton Synchrotron in the search of weak neutral currents. This led to the experimental observation of the weak neutral currents that was announced in July 1973, shortly after their theoretical prediction by Sheldon Glashow, Abdus Salam and Steven

[1]The positron interacts via electron-positron annihilation producing two photons. The neutron decelerates before being eventually captured by a cadmium nucleus, originating a photon emission about 15 μ s after the positron. These photons are detected and the 15 μs of difference identify the neutrino interaction

Weinberg.

Two years later, the τ lepton is discovered by a group led by the physicist Martin Perl at SLAC[2], which later led to the evidence of a third neutrino flavor, the tau neutrino ν_τ [11] which was discovered in 2000 in the DONUT [12] experiment at FERMILAB [13].

2.1.1 Neutrino Flavors

The number of neutrinos participating in the electroweak interaction can be determined by the Z^0 decay width. It was confirmed at LEP (CERN) [14][15][16][17] long before the observation of the ν_τ, that there are only three light neutrinos.

LSND claimed in 1995 that three neutrinos were not enough to explain their results and introduced a sterile neutrino [18]. This sterile neutrino does not undergo weak interactions nor interacts in any other way but gravity. However, MiniBooNE results from late March 2007 showed no evidence of muon neutrino to electron neutrino oscillations in the LSND region, refuting a simple 2-neutrino oscillation interpretation of the LSND results. More advanced analyses of their data are currently being undertaken by the MiniBooNE collaboration [19].

2.1.2 Helicity

An experiment carried by C.S Wu [20] in 1957 determined that the weak interaction maximally violates parity conservation. Applying this result to massless neutrinos leads to the condition that neutrinos must be fully polarised with a helicity of $+1$ or -1. In 1958, an experiment by Goldhaber [21] measured the helicity of the neutrino and determined that only left-handed neutrinos (spin anti-parallel to neutrino direction) and right-handed anti-neutrinos (spin parallel to anti-neutrino direction) participate in the weak interaction.

2.1.3 Solar Neutrinos

The Sun is a powerful source of electron neutrinos with energies of about 1 MeV, produced in thermonuclear fusion reactions in the core of the Sun [22]. Since neutrino interactions with matter are extremely weak, most of the neutrinos pass through the Sun and go to space.

The flux of solar neutrinos that get to the Earth is enormous but its detection is quite difficult and require big detectors due to the low cross section rates neutrinos have. These detector

[2]SLAC: Stanford Linear Accelerator Center

are installed underground in order to protect them from cosmic rays.

The pioneering experiment in this field was performed deep in the Homestake Gold Mine in South Dakota starting in the early 1970s [23]. A large tank was filled with 100,000 gallons of C_2Cl_4, an ordinary cleaning fluid. Electron neutrinos reacted with the chlorine in the solution to produce Argon-37. The tank was periodically purged with Helium gas and any Argon atoms were captured in a charcoal trap, that then decayed producing electrons and detected. The number of electrons were proportional to the electron neutrino flux at the mine. But the average neutrino flux measured was only 28% of the flux predicted by the standard solar model[24].

In the 1990s, different experiments, SAGE [25], GALLEX [26], Kamiokande, Super-KamioKande [27], also measured solar neutrino rates with the similar results. SAGE measuremtns were only 51% of the flux predicted by the standard solar model, GALLEX 53%, KamioKande 42% and Super-K 37%.

The discrepancies related to the solar neutrinos remained until the SNO experiment (Sudbury Neutrino Observatory [28]) contributed significantly into the topic. The detector consisted of 1,000 tonnes of heavy water (D_2O) enclosed in a transparent plastic vessel measuring 12 meters across. The vessel was itself enclosed in 7,000 tonnes of pure normal water, lodged in an immense 22 meters wide and 34 meters high cavity. The acrylic vessel was surrounded by a geodesic dome equipped with 9,600 detectors that sensed the presence of neutrinos. The frequency of neutrino detection was one per hour. Unlike previous experiments, SNO was able to detect the tree flavors of neutrinos. Electron neutrinos ν_e are produced at the core of the Sun, but during their travel to Earth, they could oscillate into ν_μ and ν_τ, explaining these discrepancies.

2.1.4 Atmospheric Neutrinos

Another source of neutrinos is the upper atmosphere. Primary cosmic rays consisting mainly of high energy protons and electrons bombard the earth's atmosphere continuously from all directions. The protons interact with nuclei in the superior atmosphere producing mainly pions that decay as [29]:

$$\pi^+ \rightarrow \mu^+ + \nu_\mu \quad , \quad \pi^- \rightarrow \mu^- + \bar{\nu}_\mu \tag{2.2}$$

Muons decay into electrons and electron neutrinos through the following process:

$$\mu^+ \rightarrow e^+ + \nu_e + \bar{\nu}_\mu \quad , \quad \mu^- \rightarrow e^- + \bar{\nu}_e + \nu_\mu \tag{2.3}$$

Many experiments measured the ratio of muon to electron events. A double ratio R was also conventionally calculated, which is the ratio of the μ/e ratio measured by experiment to the μ/e ratio predicted by Monte Carlo simulations, and is expected to be 1 if the data is correctly described by the Monte Carlo. Figure 2.2 shows the double ratio R for different experiments: Kamiokande Sub-GeV, Super-Kamiokande Sub-GeV (where Sub-GeV means the visible energy measured is less than 1330 MeV), Kamiokande Multi-GeV, Super-Kamiokande Multi-GeV (where Multi-GeV means the visible energy $E_{vis} > 1330$ MeV) [30], IMB (Sub-GeV and Multi-GeV) [31], Soudan 2 [32], Fréjus [33], NUSEX [34], where only NUSEX and Fréjus didn't see a significant deviation from the unity.

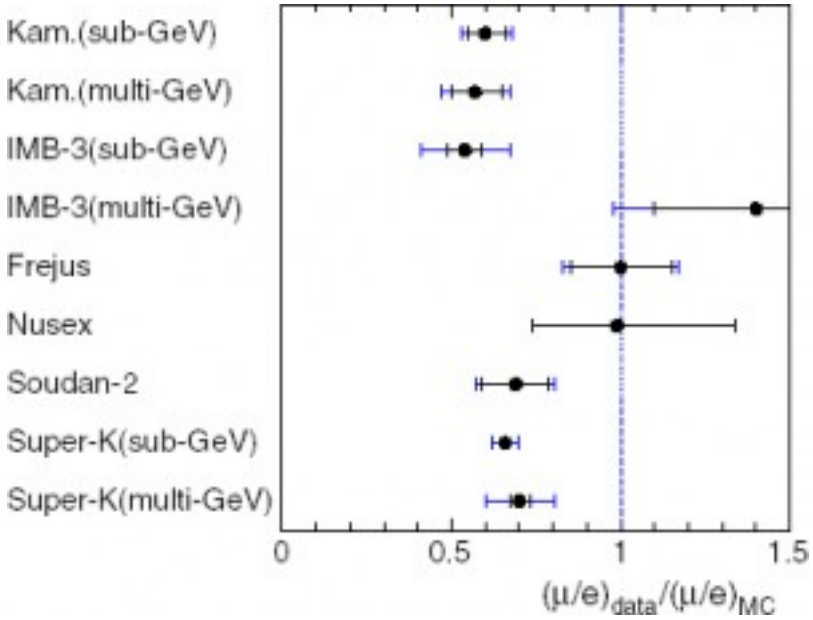

Figure 2.2: The atmospheric neutrino anomaly [35].

The Super-Kamiokande [36] experiment delivered the most precise results on the Atmospheric Neutrinos Anomaly. Super-Kamiokande is a 50 Kiloton water Cherenkov detector constructed under Mt. Ikenoyama located at the central part of Japan, giving it a rock over-burden of 2,700 m water-equivalent. The fiducial mass of the detector for atmospheric neutrino analysis is 22.5 kiloton. The experiment found substantial difference between the flux of neutrinos produced above the detector and the ones produced in the antipode region in South Atlantic. This observation could be explained with the oscillation of ν_μ neutrinos into ν_τ when traveling more than 12 km through the earth.

2.2 Neutrinos in the Standard Model

In the seventies, S. Glashow, S. Weinberg and A. Salam, proposed the electro-weak model, which unify electromagnetic and weak interactions postulating four massless gauge bosons, ordered in an isovector triplet under the SU(2) group and an isoscalar singlet under the U(1) group. The model is referred to the group $SU(2)_L \otimes U(1)_Y$.

The spontaneous symmetry breaking $SU(2)_L \otimes U(1)_Y$ allow bosons to acquire mass while interacting with a scalar field (Higgs boson) that permeates the whole space. The massive bosons are denoted $W^{\pm}_{\mu}$ and Z^0_{μ} while one, the photon A_{μ} remains massless [37].

.

In relativistic quantum mechanics, fermions with spin $\frac{1}{2}$ and mass m are described by the Dirac equation (using Einstein notation and considering $\hbar = c = 1$) [38]:

$$\left(i\gamma^u \frac{\partial}{\partial x^u} - m\right)\psi = 0 \tag{2.4}$$

where ψ denotes a spinor of four components and γ^u are the matrices 4×4 denoted by[3]:

$$\gamma^0 = \begin{pmatrix} 0 & \sigma^0 \\ \sigma^0 & 0 \end{pmatrix} \qquad \gamma^i = \begin{pmatrix} 0 & \sigma^i \\ -\sigma^i & 0 \end{pmatrix} \tag{2.5}$$

where σ_i, are the Pauli matrices 2×2 [29]:

$$\sigma^0 = I = \begin{pmatrix} 1 & 0 \\ 0 & 1 \end{pmatrix} \quad \sigma^1 = \begin{pmatrix} 0 & 1 \\ 1 & 0 \end{pmatrix} \quad \sigma^2 = \begin{pmatrix} 0 & -i \\ i & 0 \end{pmatrix} \quad \sigma^3 = \begin{pmatrix} 1 & 0 \\ 0 & -1 \end{pmatrix} \tag{2.6}$$

The four components of ψ, correspond to particles and anti-particles with two possible projections $J_Z = \pm\frac{1}{2}$, equivalent to the two helicities $\mathcal{H} = \frac{\mathbf{s}\cdot\mathbf{p}}{|\mathbf{p}|} = \pm 1$ where, $\mathbf{s}$ and $\mathbf{p}$ are the particle spin and momentum. Neutrinos are leptons of spin $\frac{1}{2}$ as other fermions, however, it is an experimental fact that only left-handed neutrinos ($\mathcal{H} = -1$) and right-handed anti-neutrinos are observed ($\mathcal{H} = +1$) [38].

Hence, a spinor of two components (Weyl spinors) should be enough to describe them. In a four-components theory, this is obtained with the help of the operators $P_{L,R} = \frac{1}{2}(1 \mp \gamma^5)$ [29].

$$\psi = (P_L + P_R)\psi = \frac{1}{2}(1 - \gamma^5)\psi + \frac{1}{2}(1 + \gamma^5)\psi = \psi_L + \psi_R \tag{2.7}$$

[3]This is the quiral representation (Weyl) for γ^u.

where $\gamma^5 = i\gamma^0\gamma^1\gamma^2\gamma^3 = \begin{pmatrix} -\sigma^0 & 0 \\ 0 & \sigma^0 \end{pmatrix}$

The elementary particles are arranged in a weak isospin $SU(2)_I$ that consists of doublets for chiral left-handed fields and singlets for right-handed fields in the form:

$$\begin{array}{cccccccccc} \begin{pmatrix} e \\ \nu'_e \end{pmatrix}_L & \begin{pmatrix} \mu \\ \nu_\mu \end{pmatrix}_L & \begin{pmatrix} \tau \\ \nu'_\tau \end{pmatrix}_L & \begin{pmatrix} u \\ d' \end{pmatrix}_L & \begin{pmatrix} c \\ s' \end{pmatrix}_L & \begin{pmatrix} t \\ b' \end{pmatrix}_L \\ e_R & \mu_R & \tau_R & u_R & d_R & s_R & c_R & b_R & t_R \end{array} \tag{2.8}$$

The Glashow-Weinberg-Salam lagrangian using electromagnetic charged and neutral currents is:

$$\mathcal{L} \;=\; -e\mathcal{J}^\mu_{EM}A_\mu - \frac{g}{\cos(\theta_W)}\mathcal{J}^\mu_{NC}\mathcal{Z}_u - \frac{g}{\sqrt{2}}\left(J^{\mu\dagger}_{CC}W^+_\mu + J^\mu_{CC}W^-_\mu\right) \tag{2.9}$$

where, $\mathcal{J}^\mu_{EM}$ is the electromagnetic current, $\mathcal{J}^\mu_{NC}$ the weak neutral current, and $J^{\mu\dagger}$,J^μ the weak charged current and the coupling associated with the photon field A_μ, the field of the boson $W^\pm_\mu$ and the boson Z_μ.

The lepton currents (quiral representation) are given by [38, 39]:

$$\begin{array}{rcl} \mathcal{J}^\mu_{EM} & = & \bar{l}_L\gamma^\mu l_L + \bar{l}_R\gamma^\mu l_R \;=\; \bar{l}\gamma^\mu l \\ \mathcal{J}^\mu_{NC} & = & \frac{1}{2}\bar{\nu}_{l_L}\gamma^\mu\nu_{l_L} - \frac{1}{2}\bar{l_L}\gamma^\mu l_L - sin^2\theta_W\mathcal{J}^\mu_{EM} \\ J^{\mu\dagger}_{CC} & = & \bar{\nu}_{lL}\gamma^\mu l_L \\ J^\mu_{CC} & = & \bar{l}_L\gamma^\mu\nu_{lL} \end{array} \tag{2.10}$$

Or in Dirac representation [40]:

$$\begin{array}{rcl} \mathcal{J}^\mu_{EM} & = & \bar{l}_L\gamma^\mu l_L + \bar{l}_R\gamma^\mu l_R \;=\; \bar{l}\gamma^\mu l \\ \mathcal{J}^\mu_{NC} & = & \frac{1}{2}\bar{\nu}_l\gamma^\mu\left(\frac{1-\gamma^5}{2}\right)\nu_l - \frac{1}{2}(1-2\sin^2\theta_W)\bar{l}\gamma^\mu\left(\frac{1-\gamma^5}{2}\right)l + \sin^2\theta_W\gamma^\mu\left(\frac{1-\gamma^5}{2}\right)l \\ J^{\mu\dagger}_{CC} & = & \bar{\nu}_l\gamma^\mu\left(\frac{1-\gamma^5}{2}\right)l \\ J^\mu_{CC} & = & \bar{l}\gamma^\mu\left(\frac{1-\gamma^5}{2}\right)\nu_l \end{array} \tag{2.11}$$

Where θ_W is the *Weingerg angle*, such that: $\sin\theta_W \;=\; \frac{e}{g}$

2.3 Neutrino Mass

Massless particles in the Standard Model formulation [41] guarantees gauge invariance under $SU(2)$ or $U(1)$ transformations; however, it is an experimental fact that particles and gauge bosons $W^{\pm}, Z^0$ do have mass (which makes the weak force to be short range)[4].

In the standard model, mass addition is accomplished through the spontaneous symmetry breaking via Higgs Mechanism. In order to break $SU(2)$ symmetry, a fundamental complex weak doublet of scalar (spin-0) fields for the charged and neutral states is introduced:

$$\phi \;=\; \begin{pmatrix} \phi^{\dagger} \\ \phi^{0} \end{pmatrix} \tag{2.12}$$

which leads us to add the so called Yukawa coupling to the Standard Model lagrangian for each lepton family:

$$\mathcal{L}_{Yuk} \;=\; -c_l \left[\bar{\nu_L}\phi^{\dagger} l_R + \bar{l}_L \phi^0 l_R\right] + h.c \tag{2.13}$$

where c_l is an arbitrary constant coupling and $h.c$ the hermitian conjugate.

After the spontaneous symmetry breaking, the values for the ϕ field come from a particular configuration selected called *vacuum space*, motivated by the fact that such space has an electrically neutral state, where the vacuum expectation values of the Higgs field are: $< \phi^{\dagger} >= 0$ and $< \phi^0 >= v/\sqrt{2}$, where $v \simeq 246$ GeV, making neutrinos massless and leptons with charge e, μ, τ with a mass term coming from:

$$\mathcal{L}_D = -(m_D^l)\bar{l}_L l_R + h.c \tag{2.14}$$

where $m_D^l = c_l v/\sqrt{2}$, and the coupling constant c_l is experimentally obtained.

However, it is also an experimental fact that neutrinos have mass, reason why the right-handed chiral neutrino component is introduced, obtaining a lagrangian similar to the ones for the charged leptons:

$$\mathcal{L}_D^{\nu_l}(x) \;=\; -\nu_{\alpha_L}(x) m_{\alpha\beta} \nu_{\beta_R} + h.c \tag{2.15}$$

where $m_{\alpha\beta}$ is a complex matrix, than can be represented in diagonal form with the help of two unitary matrices:

[4]The weak force range is about $10^{-18}m$, in comparison to the infinite range of electromagnetic forces with the photon as its gauge boson, which is massless

$$m_{\alpha\beta} \;=\; U^{L^*}_{\alpha i}\, m_i U^R_{\beta i} \tag{2.16}$$

here, m_i are three real and positive masses. U^L, U^R are the unitary matrices.

Considering the Standard Dirac lagrangian density [29]:

$$\mathcal{L} = i\psi_L^\dagger \tilde{\sigma}^\mu \partial_\mu \psi_L + i\psi_R^\dagger \sigma^\mu \partial_\mu \psi_R - m\left(\psi_L^\dagger \psi_R + \psi_R^\dagger \psi_L\right) \tag{2.17}$$

Where $\sigma^\mu, \tilde{\sigma^\mu}$ are in function of the Pauli matrices defined in (2.6):

$$\sigma^\mu = \left(\sigma^0, \sigma^1, \sigma^2, \sigma^3\right), \tilde{\sigma^\mu} = \left(\sigma^0, -\sigma^1, -\sigma^2, -\sigma^3\right) \tag{2.18}$$

and ψ_L, ψ_R come from the four-component Dirac field

$$\psi \;=\; \begin{pmatrix} \psi_L \\ \psi_R \end{pmatrix} \;=\; \begin{pmatrix} \psi_L \\ 0 \end{pmatrix} + \begin{pmatrix} 0 \\ \psi_R \end{pmatrix} \tag{2.19}$$

Then, we can define:

$$\nu_{i_L}(x) = U^{L^*}_{i\alpha}\, \nu_{\alpha_L}(x) \tag{2.20}$$

$$\nu_{i_L}(x) = U^{R^*}_{i\alpha}\, \nu_{\alpha_R}(x) \tag{2.21}$$

and replace in 2.15, getting:

$$\mathcal{L}^{\nu_l}_D(x) \;=\; -m_i\left(\nu^\dagger_{i_L}\nu_{i_R} + \nu^\dagger_{i_R}\nu_{i_L}\right) \tag{2.22}$$

Which resembles the mass term in the standard lagrangian density in terms of ψ_L and ψ_R in (2.17).

However, due to the fact that neutrinos are neutral particle, it would be possible to define them in a different way, considering the neutrino is its own anti-particle. In a Majorana field we have [42]:

$$\nu \;=\; \nu_L + \nu^C_L \tag{2.23}$$

which satisfies the Majorana condition:

$$\nu^C \;=\; \nu \tag{2.24}$$

The mass term in the Majorana Lagrangian density is given by [29]:

$$\mathcal{L}_{\mathcal{M}}(x) \;=\; -\frac{1}{2}\nu_{\alpha}^{T}\left(-i\sigma^{2}\right)\nu_{\beta}m_{\alpha\beta} + h.c \tag{2.25}$$

where α, β take values of the three neutrino flavors e, μ, τ, and $\nu_{\alpha}, \nu_{\beta}$ are chiral left-handed neutrinos (L subscript are omitted for better clarity) and $m_{\alpha\beta}$ is an arbitrary complex matrix. If we consider $m_{\alpha\beta} = m_{\beta\alpha}$, we can then write:

$$m_{\alpha\beta} \;=\; U_{\alpha i}m_{i}U_{\beta i} \tag{2.26}$$

where m_i are three positive masses, and we can define:

$$\nu_{i}(x) \;=\; U_{\alpha i}\nu_{\alpha}(x) \tag{2.27}$$

where the equation 2.25 becomes:

$$\mathcal{L}_{\mathcal{M}}(x) \;=\; -\frac{1}{2}m_{i}\nu_{i}^{T}\left(-i\sigma^{2}\right)\nu_{i} + h.c \tag{2.28}$$

where:

$$\nu_{\alpha}(x) \;=\; U_{\alpha i}^{*}\nu_{i}(x) \tag{2.29}$$

2.4 Neutrino Oscillations

Neutrino oscillations are related to the fact that the mass of neutrinos is not zero, which is why it requires extending the Standard Model.

In the neutrino oscillation model, the neutrinos that are produced by weak interactions (weak eigenstates) are not states of a definite mass but a linear superposition of mass eigenstates instead. This can be expressed in the form of a mixing matrix, if we assume only two neutrino species, then such matrix would be:

$$\begin{pmatrix} \nu_{\alpha} \\ \nu_{\beta} \end{pmatrix} \;=\; \begin{pmatrix} \cos\theta & \sin\theta \\ -\sin\theta & \cos\theta \end{pmatrix}\begin{pmatrix} \nu_{1} \\ \nu_{2} \end{pmatrix} \tag{2.30}$$

where $(\nu_{\alpha}, \nu_{\beta})$ are the weak eigenstates and (ν_1, ν_2) the mass eigenstates and θ is the neutrino mixing angle. Also, α, β are the neutrino flavors and you could associate two masses m_1, m_2 to the mass eigenstates.

Hence, using equation 2.30, a neutrino weak eigenstate at a time $t = 0$ would then be:

$$|\nu_\alpha(t=0)\rangle = \sin\theta|\nu_1\rangle + \cos\theta|\nu_2\rangle \tag{2.31}$$

However, for a time $t \neq 0$, the mass eigenstate propagates with a different phase factor, as following:

$$|\nu_\alpha(t)\rangle = \sin\theta e^{-iE_1 t - px}|\nu_1> + \cos\theta e^{-iE_2 t - px}|\nu_2> \tag{2.32}$$

where E_1, E_2 are the mass eigenstates energies with a momentum p. If we consider the extreme relativistic approximation for very small neutrino masses $m << p$, then:

$$E_{1,2} \approx p + \frac{m_{1,2}^2}{2p} \tag{2.33}$$

So, using 2.33 in 2.32:

$$|\nu_\alpha(t)\rangle = |\nu_1\rangle \cos\theta e^{-\frac{-im_1^2 L}{2E}} + |\nu_2\rangle \sin\theta e^{-\frac{im_2^2 L}{2E}} \tag{2.34}$$

where $E = p$ and L is defined as the distance from the neutrino production to the neutrino detection. So, after that distance propagation L, the probability to find a different neutrino flavor is defined as:

$$P(\nu_\alpha \to \nu_\beta, t) = |<\nu_\beta|\nu_\alpha(t)>|^2 = \sin^2(2\theta)\sin^2\left(\Delta m^2 L/4E\right) \tag{2.35}$$

where $\Delta m^2 = m_2^2 - m_1^2$ is the mass square difference.

2.5 Neutrino Interactions

The interest in neutrino interactions has recently increased in the physics community due to the need of it for neutrino oscillation data interpretation. Neutrino scattering results on both charged current (CC) and neutral current (NC) interaction channels.

Neutrinos cross sections can be expressed as:

$$\sigma = \sigma^{CC} + \sigma^{NC} \tag{2.36}$$

and each one of these inclusive cross sections can be broken up in three basic processes which are described in Sections 2.5.1, 2.5.2 and 2.5.4: Quasi-Elastic σ^{QE}, Resonance σ^{RES} and Deep Inelastic σ^{DIS} each of which has its own model and associated uncertainties (see Equation 2.37).

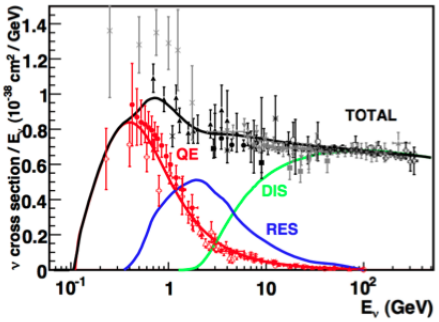

Figure 2.3: Existing muon neutrino charged-current cross section measurements and predictions as a function of neutrino energy. The contributing processes in this energy region include Quasi-Elastic (QE) scattering, Resonance Production (RES), and Deep Inelastic Scattering (DIS)[43]

$$\sigma^{CC,NC} = \sigma^{QE} + \sigma^{RES} + \sigma^{DIS} \tag{2.37}$$

For the sake of simplicity, small contributions to the total cross section in the few GeV energy range, such as coherent and elastic νe^- scattering, were omitted from the expression above (See Figure 2.3).

2.5.1 Deep Inelastic Scattering

This is the dominant channel at high neutrino energies (see Figure 2.3). The term "deep" is due to the fact that the interaction is produced at the quark level. It is characterized by a high momentum transfer q. The associated wavelength of the propagator $\frac{1}{|q|}$ is at the size scale of the nucleon constituents.

Neutrinos have the unique ability to taste particular flavors of quarks, hence playing an important role in the extraction of *Parton Distribution Functions* (PDFs)[5], which represent probability densities to find a parton carrying a momentum fraction x at a squared energy scale Q^2 [44]. In charged current DIS, the ν interact with $d, s, \bar{u}$ and $\bar{c}$ while the $\bar{\nu}$ interact with $u, c, \bar{d}$ and $\bar{s}$. This is due to charge conservation i.e: $\nu(0) + d(-\frac{1}{3}) \rightarrow \mu^-(-1) + u(\frac{2}{3})$.

The main interactions for charged and neutral current can be expressed in equations 2.38 and 2.39:

[5]The Parton name was proposed by Richard Feynman in 1969 as a generic description for any particle constituent within the proton, neutron and other hadrons. These particles are referred today as quarks and gluons.

$$\text{Charged Current :} \tag{2.38}$$
$$\nu_l + N \rightarrow l^- + X$$
$$\bar{\nu}_l + N \rightarrow l^+ + X$$
$$\text{Neutral Current :} \tag{2.39}$$
$$\nu_l + N \rightarrow \nu_l + X$$
$$\bar{\nu}_l + N \rightarrow \bar{\nu}_l + X$$

where, $N = p, n$ and X denotes any final hadron state.

2.5.2 Resonance Production

In this interaction process, a resonant state is produced due to the excitation of the nucleon during the interaction process. These excited states decay to their fundamental states producing a combinations of nucleons and mesons.

Resonant reactions can be expressed as:

$$\nu + N \rightarrow \nu + R \tag{2.40}$$
$$\nu + N \rightarrow l^- + R \tag{2.41}$$

The resonant production in neutrino interactions represents a significant fraction of the total cross section for the few GeV range as seen in Figure 2.3.

This channel is also the main background source for experimental quasi-elastic analyses, which is the main channel in this thesis. In particular, resonant processes where single pions are produced.

2.5.2.1 Resonance Single Pion Production

As mentioned in section 2.5.2, resonance reactions involve a nucleon that is excited into a resonance state. At low neutrino energies, these resonance states are composed of isospin $1/2(N^*)$ and $3/2\Delta$ states, which generally decay into a nucleon and a single pion final state (See figure 2.4).

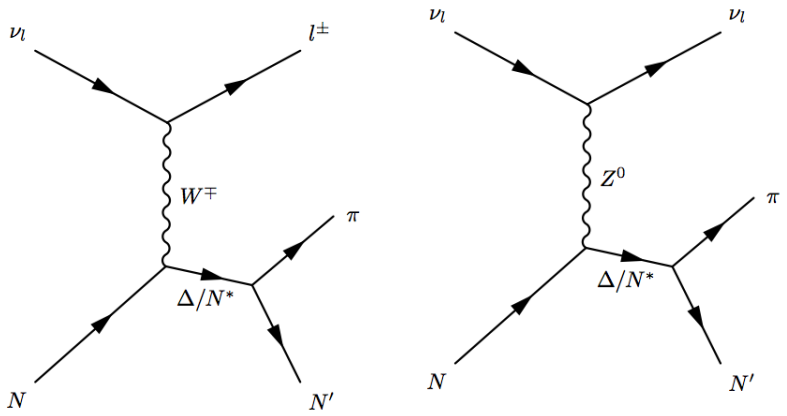

Figure 2.4: (left) Charged and (right) Neutral Current resonance pion production

Resonance reactions in which intermediate resonance states like $\Delta(1232)$ are produced are given in equations 2.42 (charged current reactions) and 2.43 (neutral current reactions) :

Charged Current: (2.42)

$$\begin{aligned}
\nu_\mu + p \rightarrow \mu^- + p + \pi^+ \quad &, \quad \bar{\nu}_\mu + p \rightarrow \mu^+ + p + \pi^- \\
\nu_\mu + n \rightarrow \mu^- + n + \pi^+ \quad &, \quad \bar{\nu}_\mu + n \rightarrow \mu^+ + n + \pi^- \\
\nu_\mu + n \rightarrow \mu^- + p + \pi^0 \quad &, \quad \bar{\nu}_\mu + p \rightarrow \mu^+ + n + \pi^0
\end{aligned}$$

Neutral Current: (2.43)

$$\begin{aligned}
\nu_\mu + p \rightarrow \nu_\mu + p + \pi^0 \quad &, \quad \bar{\nu}_\mu + p \rightarrow \bar{\nu}_\mu + p + \pi^0 \\
\nu_\mu + n \rightarrow \nu_\mu + n + \pi^0 \quad &, \quad \bar{\nu}_\mu + n \rightarrow \bar{\nu}_\mu + n + \pi^0 \\
\nu_\mu + p \rightarrow \nu_\mu + n + \pi^+ \quad &, \quad \bar{\nu}_\mu + p \rightarrow \bar{\nu}_\mu + n + \pi^+ \\
\nu_\mu + n \rightarrow \nu_\mu + p + \pi^- \quad &, \quad \bar{\nu}_\mu + n \rightarrow \bar{\nu}_\mu + p + \pi^-
\end{aligned}$$

The single pion production from baryonic resonances is predicted using the Rein and Sehgal model [45], which works well for high energy neutrino interactions, but are poorly constrained by neutrino data at lower energies (below 2 GeV) [46].

2.5.3 Coherent Pion Production

In coherent pion production, very little energy is exchanged between the neutrino and the target. The nucleus remains intact in its fundamental state but a single pion exists in the final state from the coherent sum of scattering from all the nucleons, with the same charge as the boson involved in the interaction [47]. Coherent charged and neutral current processes are

expressed in equations 2.44.

$$\text{Neutral Current} \tag{2.44}$$
$$\nu_\mu + A \to \nu_\mu + A + \pi^0 \quad , \quad \bar{\nu}_\mu + A \to \bar{\nu}_\mu + A + \pi^0$$
$$\text{Charged Current} \tag{2.45}$$
$$\nu_\mu + A \to \mu^- + A + \pi^+ \quad , \quad \bar{\nu}_\mu + A \to \mu^+ + A + \pi^-$$

Just as in the resonance pion production case, the Rein and Sehgal model [45] is also used for predicting these reactions but more data is necessary to constrain the model. There are many pion analyses currently on-going on the Minerνa experiment from both neutrino and anti-neutrino resonant and coherent channels.

2.5.4 Quasi-Elastic Scattering

This is the dominant channel below 2 GeV as Figure 2.3 shows. The neutrino scatters off a nucleon inside the nucleus of an atom by the exchange of the W boson (for charged current interactions) or the Z boson (for neutral current interactions) and one nucleon (or multiple nucleons) come out from the target. The term "quasi" for charged current interactions is due to the fact the the neutrino can change its identity to a charged lepton and the neutron can suffer a quark flip becoming a proton. For neutral current interactions, this process is referred simply as *elastic scattering*.

2.5.4.1 Charged Current Quasi-Elastic Scattering

The charged current quasi-elastic reactions for neutrinos and anti-neutrinos are[6]:

$$\nu_l + n \to p + l^- \tag{2.46}$$
$$\bar{\nu}_l + p \to n + l^+ \tag{2.47}$$

where $l = e, \mu, \tau$.

The differential cross section can be expressed in the Llewellyn-Smith formalism [48]. This formalism allows to describe the cross section in terms of functions that only depend on the four-momentum transfer Q^2. The neutrino cross section is then written as follows:

[6]The equation 2.47 with $l = e$ is also called *inverse beta decay* and has been used in historical experiments such as in the Cowan and Reines experiment (Section 2.1), where neutrinos where observed for the first time.

$$\frac{d\sigma_{CC}^{\nu_l n,\bar{\nu}_l p}}{dQ^2} = \frac{G_F^2 |V_{ud}|^2 m_N^4}{8\pi \left(p_\nu \cdot p_{N_i}\right)^2} \left[A\left(Q^2\right) \pm B\left(Q^2\right) \frac{s-u}{m_N^2} + C\left(Q^2\right) \frac{(s-u)^2}{m_N^4} \right] \tag{2.48}$$

where $s - u = 4ME_\nu - Q^2 - m_l^2$, and A, B, C are in function of Q^2:

$$\begin{aligned} A = & \frac{m_l^2 + Q^2}{m_N^2} \left\{ (1+\tau) F_A^2 - (1-\tau)(F_1^V)^2 + \tau(1-\tau)(F_2^V)^2 + 4\tau F_1^V F_2^V \right. \\ & \left. - \frac{m_l^2}{4m_N^2} \left[\left(F_1^V + F_2^V\right)^2 + (F_A + 2F_P)^2 - \left(\frac{Q^2}{m_N^2} + 4 \right) F_P^2 \right] \right\} \\ B = & \frac{Q^2}{m_N^2} F_A \left(F_1^V + F_2^V\right) \\ C = & \frac{1}{4} \left(F_A^2 + (F_1^V)^2 + \tau (F_2^V)^2\right) \end{aligned} \tag{2.49}$$

where $\tau = \frac{Q^2}{4m_N^2}$. Notice that neutrinos and anti-neutrinos just differ in the cross section formula by the sign in the B term.

In other words, the cross section can be expressed in terms of four form factors: F_1^V, F_2^V, F_A and F_P. The vector form factors $F_{1,2}^V$ can be expressed considering the conserved vector current hypothesis (CVC) [49] in terms of the Dirac and Pauli electromagnetic form factors $F_1^{p,n}, F_2^{p,n}$:

$$F_{1,2}^V = F_{1,2}^p - F_1^n \tag{2.50}$$

These electromagnetic form factors have been measured in electron scattering experiments, and can be written in the Galster et all formalism [50]:

$$F_1^{p,n} = \frac{G_E^{p,n} + \tau G_M^{p,n}}{1+\tau} \tag{2.51}$$

$$F_2^{p,n} = \frac{G_M^{p,n} + \tau G_E^{p,n}}{1+\tau} \tag{2.52}$$

where $\tau = -q^2/m_N^2$. The G_E and G_M are called the Sachs form factors and are parameterized in terms of the dipole form factor in the following way:

$$G_E^p(Q^2) = G_D(Q^2) \tag{2.53}$$

$$G_E^n(Q^2) = 0 \tag{2.54}$$

$$G_M^p(Q^2) = \mu_p G_D(Q^2) \tag{2.55}$$

$$G_M^n(Q^2) = \mu_n G_D(Q^2) \tag{2.56}$$

where:

$$G_D(Q^2) = \frac{1}{1 + Q^2/M_V^2} \tag{2.57}$$

where the vector mass $M_V = 0.843$ GeV.

The pseudo-scalar form factor F_P and the axial form factor F_A can be related by requiring partially conserved vector current (PCAC) [51]:

$$F_P(Q^2) = \frac{2m_N^2}{Q^2 + m_\pi^2} F_A(Q^2) \tag{2.58}$$

The axial form factor commonly adopt the following dipolar form:

$$F_A(Q^2) = \frac{g_A}{1 + \frac{Q^2}{M_A^2}} \tag{2.59}$$

where the average axial mass constant $M_A = 1.026$ GeV and the best axial vector constant coming from beta decay experiments [52] $g_A = -1.267$.
For a detailed discussion of the axial structure of the nucleon, see Reference [53].

It is important to notice that the neutrino energy E_ν and the four-momentum transfer Q^2 can be expressed in terms of the muon kinematics as following:

$$E_\nu^{QE} = \frac{(2M_n - E_B)E_\mu - \left[(M_n - E_B)^2 + m_\mu^2 - m_p^2\right]}{2\left[(M_n - E_B) - E_\mu + \sqrt{E_\mu^2 - m_\mu^2}\cos\theta_\mu\right]} \tag{2.60}$$

$$Q_{QE}^2 = -m_\mu^2 + 2E_\nu^{QE}(E_\mu - \sqrt{E_\mu^2 - m_\mu^2}\cos\theta_\mu) \tag{2.61}$$

where E_B is called *binding energy* and is equivalent to 34 MeV in this model.

2.6 Short Range Correlations

Quasi-elastic scattering is traditionally viewed as scattering off single nucleons, as described previously. However, when nucleons are too close from each other (< 15 fm), strong short-range forces increase their relative momentum and push the nucleons far off-shell.

This is known as short range correlations (SRCs) [54] and are predicted to involve the nucleon 20% of the time and most of them are neutron-proton correlations [55, 56].

These effects are not included in the simulation but have a significant impact in the measurement. Details on this can be found in Reference [57].

2.7 Meson Exchange Currents

This is another mechanism that is not included in the standard quasi-elastic formalism.Meson exchange currents are two-body currents carried by a virtual meson which is exchanged between two nucleons in the nucleus. This leads to the emission of two nucleons in the hadronic final state. See Reference [58] for more details.

2.8 Analysis Motivation

Quasi-elastic interactions were extensively studied in between the 1970s and 1990s using deuterium-filled bubble chambers. This could be called the first generation of neutrino quasi-elastic experiments, where the main interest was to measure the axial-vector form factor of the nucleon (see reference [59]). The Llewellyn-Smith formalism was used to describe the quasi-elastic scattering (See Section 2.5.4.1).

The modern neutrino quasi-elastic experiments no longer use deuterium as a target, but heavier nuclei with $A > 2$ instead. By doing so, nuclear effects become important and produce considerable modifications to the standard quasi-elastic differential cross section described in Equation 2.48.

Figure 2.5 shows the comparison of the ν_μ CCQE cross-section as a function of neutrino energy for different experiments and models. Here, MiniBooNE [60] and NOMAD[61] are both modern neutrino experiments with high-statistics and carbon-based targets, but some disparity can be appreciated between both measurements.

NOMAD experimental data is consistent with a neutrino quasi-elastic scattering on a free nucleon target, as described in Llewellyn-Smith formalism with the standard axial mass constant $M_A \approx 1.03$. MiniBooNE data on the other hand, prefers an axial mass of $M_A = 1.35$.

Notice that the neutrino energy range is different in both experiments. MiniBooNE has neutrino energies less than 2 GeV while NOMAD cross sections have neutrino energies greater than 3 GeV.

It is currently believed that nuclear effects are responsible for these discrepancies. In particular, nucleon-nucleon correlations and two-body exchange currents can improve the accuracy of describing neutrino quasi-elastic scattering. These effects yield significantly enhanced cross

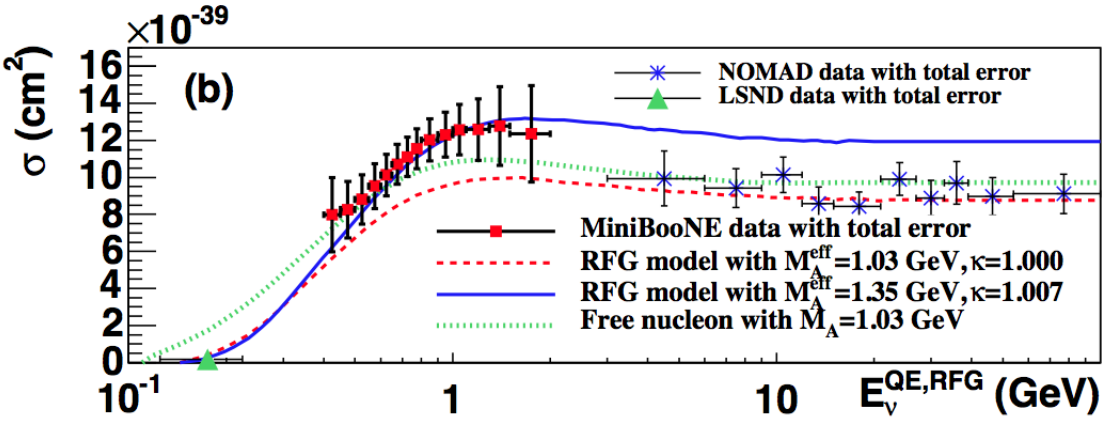

Figure 2.5: Flux unfolded $\sigma(E_\nu)$ Data for MiniBoone and NOMAD.

sections (larger than the free scattering case) which, in some cases, appear to better match the experimental data [62].

These nuclear effects also produce final states that include multiple nucleons, implying a "quasi-elastic" definition should not be restricted to a single nucleon.

Nowadays, the fact that nuclear effects may play an important role in neutrino quasi-elastic scattering has made both theorists and experimentalists to put a lot of effort in these studies (See Sections 2.6 and 2.7).

Since the total cross sections $\sigma(E_\nu)$ and the axial mass are model dependent quantities, especially when scattering off nucleon targets, there is a strong preference to report differential cross section results in term of observables instead. MiniBooNE measured single differential cross section as a functions of Q^2 and a double differential cross section in terms of the muon kinetic energy and the scattering angle [63] for $E_\nu < 2$ GeV.

Figure 2.6 shows a single differential quasi-elastic cross section as a function of Q^2 compared to different models in the MINERνA experiment. The purity of the sample is about 49% and the background is removed with a MC-driven background subtraction technique that constrains the background models with MINERνA own data [64] in order to lessen the model dependency.

The analysis in this thesis aims to improve the purity of the MINERνA quasi-elastic sample by extending the reconstruction to identify the protons and rejecting pion backgrounds that decay into michel electrons (see Section 5). The analysis will measure *Quasi-Elastic Like* events, which are events that a detector can see (see definition in Section 6.2), with a neutrino energy 1.5

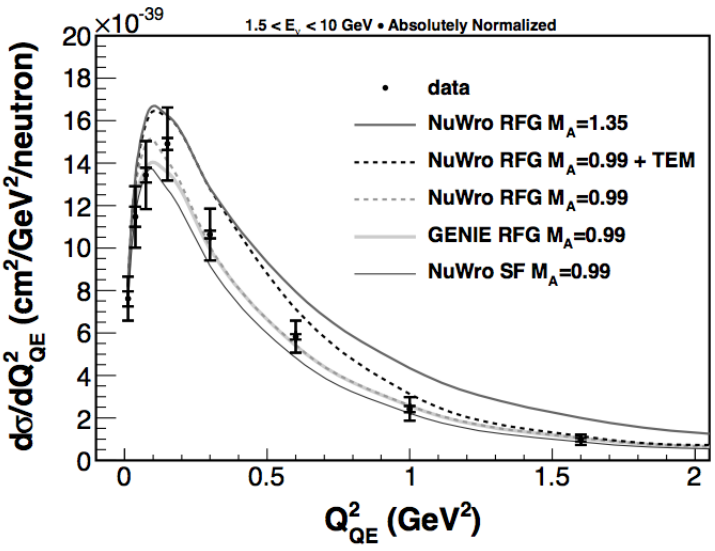

Figure 2.6: Minerva single differential cross section $d\sigma/dQ^2$

GeV $< E_\nu <$ 10.0 GeV. In order to lessen the model dependency, it also aims to measure a double differential cross section as a function of two observables: the longitudinal (P_Z) and transverse (P_T) momentum of the muon. This phase space was chosen instead of the $T_\mu \cos\theta_\mu$ phase space used by MiniBoonE because the muon scattering angles are more forward in MINERνA due to the higher neutrino energies from the NuMI beam, and because this acceptance is limited more by the requirement of these muons to match into the MINOS Near Detector (see Section 5.3). Figure 2.7 shows how different constant values of the neutrino energy and the four-momentum transfer $E_\nu^{QE}, {Q^2}_{QE}$ calculated under the quasi-elastic assumption from the muon kinematics (See equations 2.60, 2.61) look like in this phase space.

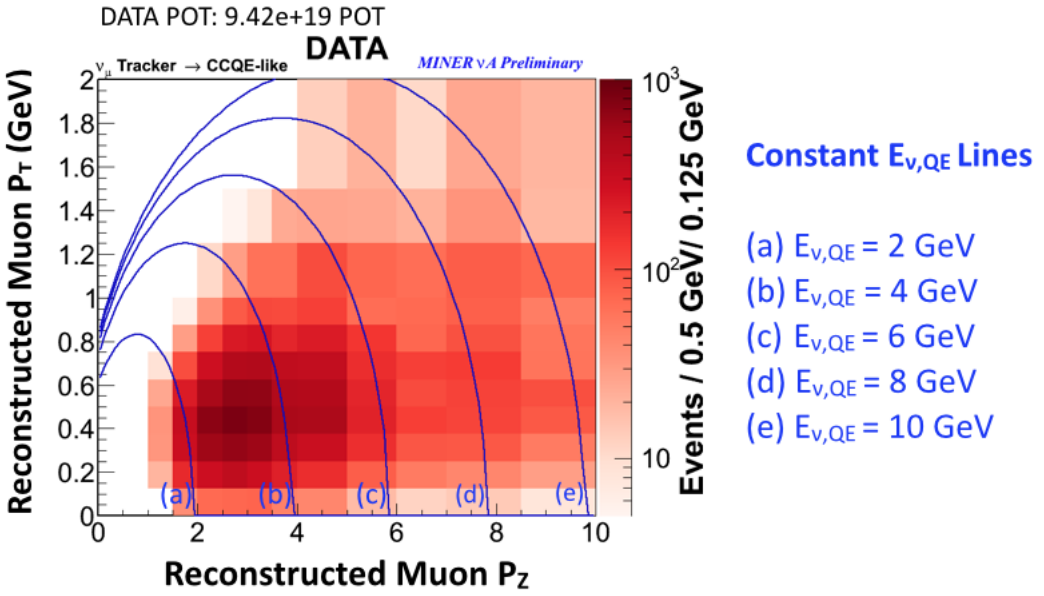

(a) Constant lines of different E_ν^{QE} values in the muon $P_Z - P_T$ phase space.

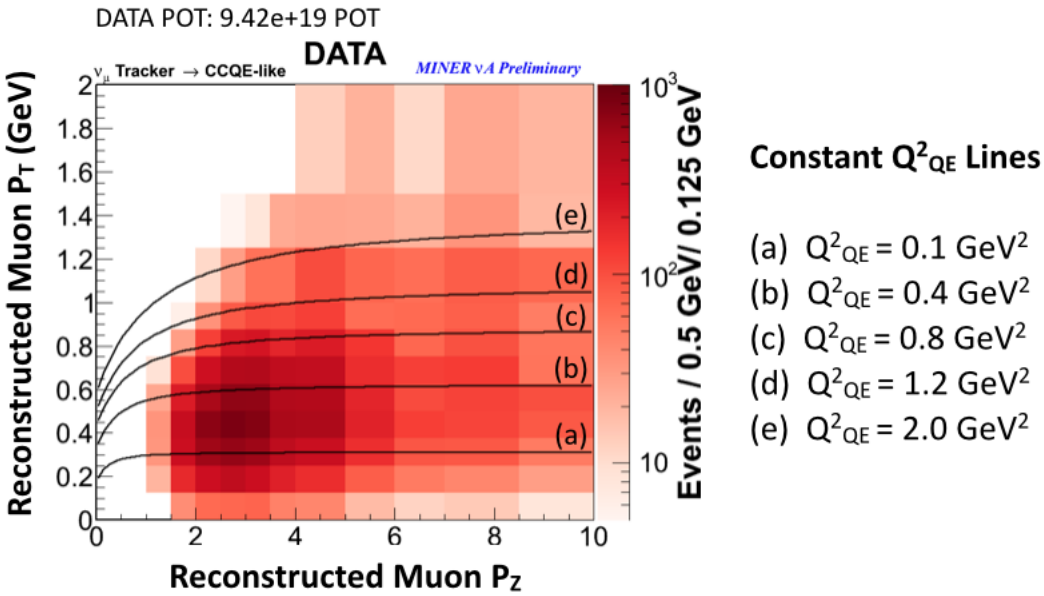

(b) Constant lines of different ${Q^2}_{QE}$ values in the muon $P_Z - P_T$ phase space.

Figure 2.7: Constant lines of $E_\nu^{QE}, {Q^2}_{QE}$ values in the muon $P_Z - P_T$ phase space. Events shown here are data events taken from March to July 2010 after passing the selection criteria described in Section 6.

CHAPTER 3

The MINERvA Experiment

3.1 General Description of the Experiment

MINERνA (Main INjector Experiment ν-A) is a few GeV neutrino-nucleus scattering experiment designed to study low energy neutrino interactions both in support of neutrino oscillation experiments and as a pure weak probe of the nuclear medium. The experiment uses a fine-grained, high resolution detector. The active region is composed of plastic scintillator with additional targets of helium, carbon, iron, lead and water placed upstream of the active region.

3.2 The NuMI Neutrino Beam

The NuMI [65] (Neutrinos at the Main Injector) is an intense $\nu_\mu, \bar{\nu}_\mu$ beam located at FERMILAB, with the purpose of serving different neutrino experiments, short and long-baseline, such as MINERνA (See figure 3.1, MINOS, ArgoNeut and NOνA [66].

The MINERνA experiment is located in the NuMI hall (next to the MINOS Near Detector [67]), about 1 km downstream of the *NuMI target* and 100 meters underground in order to get the flux for the neutrino cross section measurements.

NuMI is a tertiary beam which results from the decay of secondary kaons and pions produced in the *NuMI target*. A 120 GeV/c proton beam that is extracted from the Main Injector storage ring bombards a graphite NuMI target producing mostly kaons and pions.

These charged mesons are focused by a system composed of two toroidal magnets called *horns* into a 675 meters decay pipe and then decay primarily into μ and ν_μ. Then they travel through a region of 240 m of unexcavated rock that stop the remnant hadrons and leptons, leaving only the neutrinos (See Figure 3.2).

Figure 3.1: MINERvA installation at the NuMI Hall.

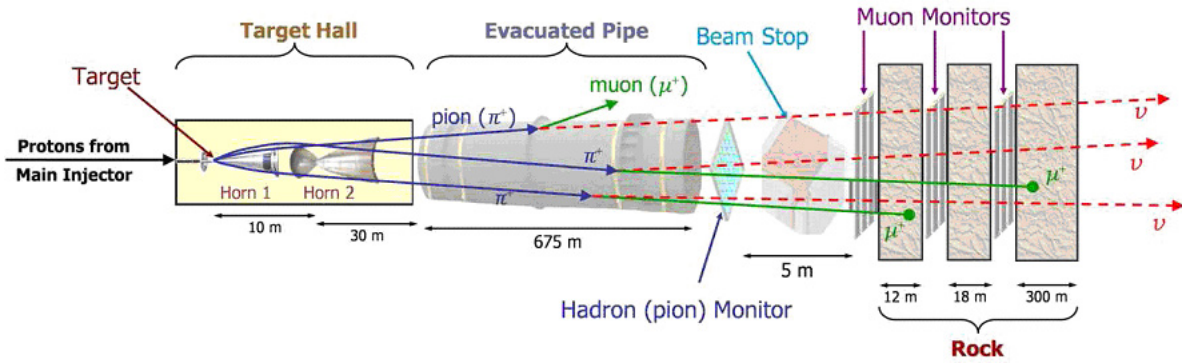

Figure 3.2: The NuMI main components.

3.3 The MINERvA Detector

The MINERνA detector consits of an inner tracker volume made of active plastic scintillator surrounded by electromagnetic and hadronic calorimeters and a set of different passive nuclear targets: helium, carbon, iron, lead and water. (See Figure 3.3).

The detector has 120 modules of hexagonal shape with an inner portion surrounded by an outer steel support frame. This frame is 56 cm wide and partially instrumented with scintillator and serves as a hadronic calorimeter. The content of the inner portion depends on the part of the detector the module is located: the tracker, calorimeters or nuclear targets.

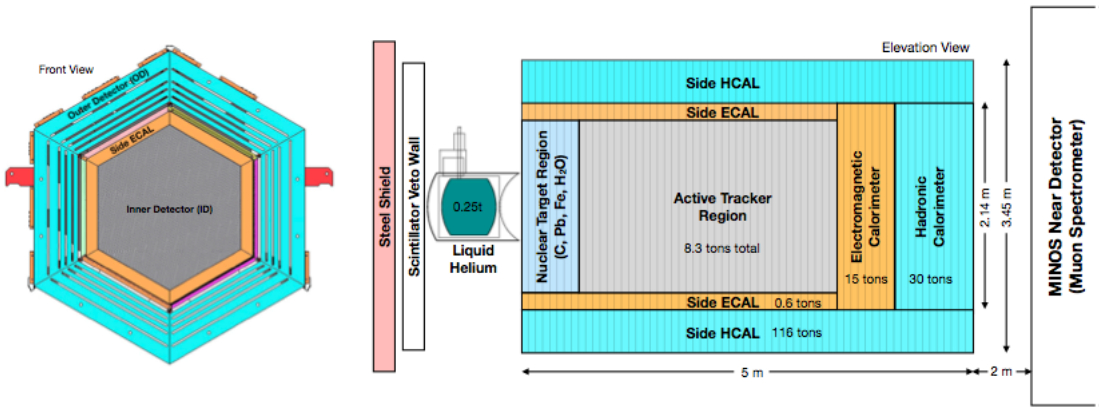

Figure 3.3: Minerva Detector Schematic

3.4 The Inner Detector

The Inner Detector (ID) has a hexagonal shape of apothem[1] 1.07 m and is composed of 120 modules divided in four regions: the nuclear target region, the tracker, the downstream electromagnetic calorimeter (ECAL) and the downstream hadronic calorimeter (HCAL). It also includes the side electromagnetic calorimeter (See Figure 3.3).

3.4.1 The Nuclear Targets

This region involves 22 tracking modules and five solid passive targets that are built in different combinations and thicknesses of iron, lead, graphite and water interspersed with active scintillator. A cryogenic helium target and a water target are also installed in this region.

Figure 3.4 describes the composition of each target and the position in the detector for all targets except the helium cryogenic target, which is located upstream of the region shown.

[1]apothem is the distance from the center a regular polygon to the midpoint of any side.

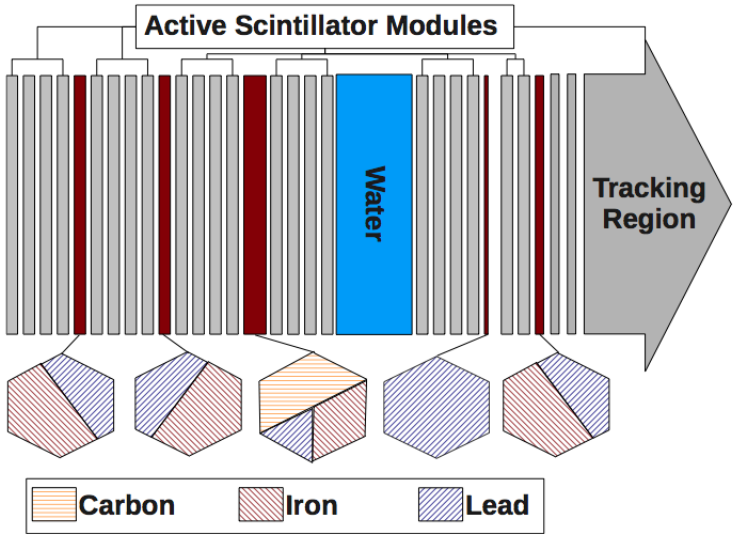

Figure 3.4: Nuclear Targets position and composition.

Targets 1 and 2 have the Pb and Fe rotated with respect to each other to allow checks for differences in detection. Target 3 contains all three nuclei with essentially the same detection capability to allow detailed studies a the dependence of interactions.

Target 4 is pure lead to insure that any produced photons, either from the upstream or downstream targets, begin to shower. The Pb sheet is about 1.5 radiation lengths thick, which is enough to begin the shower but not enough to contain it. Target 5, directly upstream of the fully active central detector, allows to study multiplicities and distributions of lower energy particles with good tracking and energy resolution.

The mass of each target and the expected rated in the MINERνA detector are shown in Table 3.1.

Target	Fiducial Mass	ν_μ CC Events in 1E20 POT
Polystyrene Scintillator	6.43 tons	340k
Helium	0.25 tons	14k
Carbon	0.17 tons	9.0k
Water	0.39 tons	20k
Iron	0.97 tons	54k
Lead	0.98 tons	57k

Table 3.1: Nuclear target masses and expected event rates in the MINERvA detector.

3.4.2 The Tracker Region

Modules in the tracker region contain three layers of finely segmented scintillator planes as shown in Figure 3.5 to allow three dimensional track reconstruction.

Each plane is composed of 127 strips of extruded polystyrene scintillator that are triangular in cross section (17.0 mm height x 33.4 mm base).

The triangular shape (See Figure 3.6) ensures energy deposition in two strips per plane for most particle paths, improving the position resolution of the reconstruction. A 1.2 mm diameter green wavelength shifting fiber down the middle of each strip guides the generated light to a single pixel of a 64 anode PMT.[68]

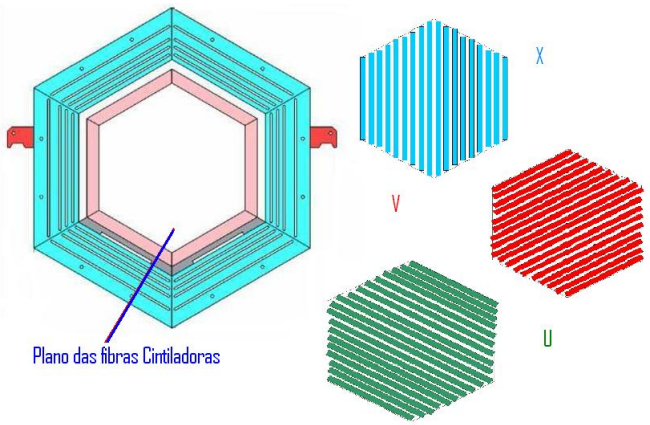

Figure 3.5: One active (tracker) module and its three planes: X,U and V. V and U are rotated ±60 degrees with respect to the X.

3.4.3 Electromagnetic Calorimeters

High energy photons are detected through the pair-production/bremsstrahlung process that lead to a shower of e^+, e^- and γ. The photons energy regime in the detector is of the order of a few GeV, so 99% of the energy is expected to be contained within 4 cm of Pb (about 7 radiation lengths).

The downstream electromagnetic calorimeter consists of 20 layers of Pb, each 2 mm thick, interleaved with one layer of scintillator, consisting of the standard 1.7 cm thick layer of triangular strips, which gives an energy resolution of approximately $6\%/\sqrt{E}$, with E in GeV. Figure 3.7 shows a cut-away view from one ECAL module.

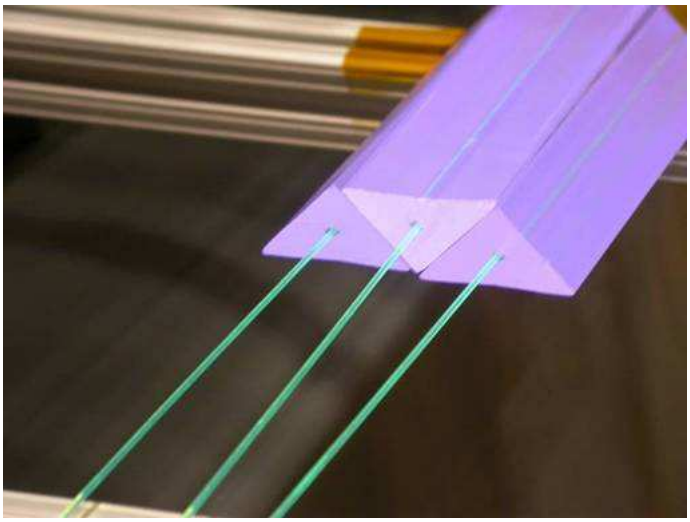

Figure 3.6: Triangular scintillator strips from the inner detector.

The side calorimetry is quite similar. Trapezoidal sheets of Pb, also 2 mm thick, will be inter- leaved with each layer of scintillator. The sheets will extend 15 cm into the active area.

Photons entering the side calorimeter are fully contained for angles less than about 25° with respect to the neutrino beam axis. At larger angles the shower is not fully contained, but penetrates into the outer hadron calorimetry, where the remainder of the shower will be fully contained, but less well sampled, leading to a decline in resolution.

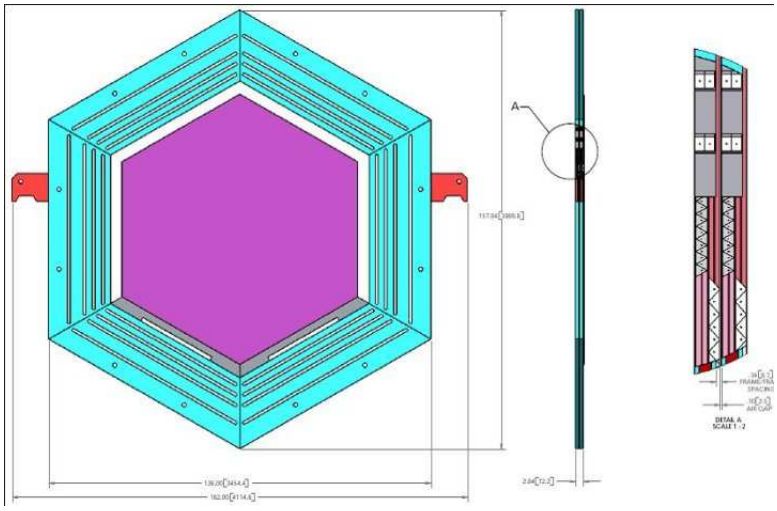

Figure 3.7: View of an ECAL detector module. The figure at right shows a cut-away view from the side.

3.4.4 Downstream Hadronic Calorimeter

The downstream hadron calorimetry consists of 20 layers of iron, each 2.54 cm thick, interleaved with one layer of scintillator between plates, downstream of the electromagnetic calorimeter. The combined thickness of the 4 cm of Pb and 50 cm of Fe stop muons up to about 600 MeV and protons up to about 800 MeV. One nuclear interaction length is 16 cm for Fe, so higher energy protons (or pions) will also generally be stopped. Figure 3.8 shows a cut-away view from one HCAL module.

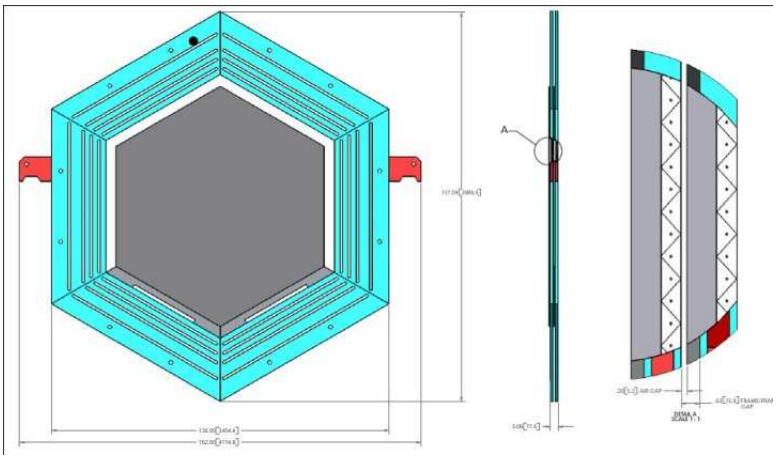

Figure 3.8: View of an HCAL detector module. The figure at right shows a cut-away view from the side.

Based on studies by the MINOS collaboration the resolution of the hadron calorimeter is about $50\%/\sqrt{E}$ for hadron energies above 1 GeV. For lower energy particles, the resolution is 50% or less, depending on the energy. The primary reason for the poor resolution is the likely interaction of the particle with a nucleus before stopping, which frequently produces one or more energetic neutrons whose energy is unobserved, making it difficult to get good energy resolution.

3.5 The Outer Detector

The outer detector is the side hadron calorimeter that consists of plates of iron 55.9 cm thick, with fives slots, each 2.5 cm wide, filled with scintillator. The total iron thickness is 43.4 cm, or 340 g/cm^2 , which can stop, from ionization losses alone, up to 750 MeV protons at 90° and nearly 1 GeV protons entering at an angle of 30°. It also used as the detector support structure and as a constraint for the plane alignment.

3.6 Electronics and DAQ (Data Acquisition)

The light acquired from abouth 30.000 scintillators in the MINERνA experiment has to be converted to electric pulses with an amplitude proportional to the deposited energy and the time.

In order to accomplish this objetive, the MINERνA experiment uses multi-anode photomultiplier tubes (PMTs) R7600U-00-M64, each with 64 pixels or channels, provided by Hamamatsu Photonics [69]. Each XU/XV module employs 19 PMT that are the MINERνA fundamental detection instrument. There are 500 PMTs totalling about 32.000 channels.

Each PMT is covered by a cilindrical box of steel called "PMT Box", in order to isolate the PMTs from backgrounds of light or electromagnetic fields.

The input signal for each PMT is acquired from the scintillator strips through wavelength shifting fibers (WLS) that are installed at the center of each triangular scintillator strip (see Figure 3.6). The WLS fibers collect the blue scintillation light from the scintillating fibers and shift it to green, that is reflected internally in the fiber reducing the loss of signal significantly. This signal input is amplified and read out using MINERνA 's front end boards or FEBs (see Section 3.6.1) to be later translated to physical quantities.

The MINERνA electronic requirements are motivated by the following objetives:

- Fine-grained spatial resolution, exploiting light-sharing between neighboring scintillator strips.
- Identification of $\pi^{\pm}, K^{\pm}$ and p, using dE/dx information.
- Efficient pattern-recognition, using timing to identify track direction and separate interactions occurring during a single spill.
- Ability to identify strange particles, and muon decay, using delayed coincidence.
- Negligible deadtime within a spill.

3.6.1 Detector Readout

Front End Boards

The Front End Boards (FEBs) are in charge of:

- providing high voltage to the photomultiplier tubes (PMTs) via the Cockroft-Walton generator [70].
- reading out the PMT anode charge.

The board is based on the Trip-T ASIC (Application-specific integrated circuit) [71] designed for the D0 experiment by Abder Makkaoui from the *Fermilab ASIC Group* (see Figure 3.9) and are controlled through a FPGA board. Each of these chips have 32 channels for the read out process, and each two of these have a discriminator associated that triggers when the integrated charge is above a certain threshold.

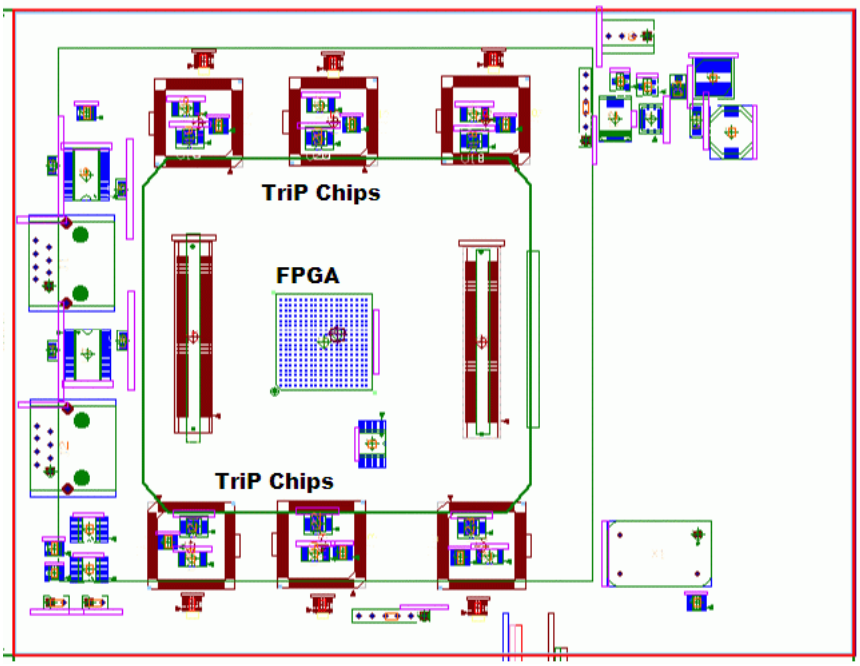

Figure 3.9: Front End Board schematic design

3.6.2 The Data Acquisition System

The standard operating mode of the readout system is to open a collection readout window (gate) on the FEB's synchronously with the delivery of neutrino beam spills of 16 μs each. This gate is opened 0.5 μs before and ends 5.5 μs after the beam spill.

Each readout system channel has a discriminator threshold, so when the charge crosses this threshold, the TriP-T's integrates the charge and stores it along with the hit time information (this happens 150 ns after the discriminator is fired). After this, there is a 20 ns time lapse in which the channels cannot be readout. This allows up to 5 readouts per gate.

All FEBs are daisy-chained together in groups of nine or ten and connected to a custom VME module called Chain Readout Controller (CROC) that serves up to four of these chains. CROCs receive timing information from another VME custom module called CROC Interface Module (CRIM), that collects timing information from the NuMI and from MINOS. The second information is used for matching events between MINERνA and MINOS detectors, since MINERνA uses the MINOS Near Detector as a muon spectrometer. MINERνA has two VME crates each housing a CAEN V2718 Crate Controller, two CRIMs and eight CROCs. These crates are accessed through a CAEN A2818 PCI Card that interact with the V2718 Crate Controller.

For a fully detailed description of the Data Acquisition System and components, please see Reference [72].

CHAPTER 4

Simulation

4.1 The NuMI Flux

Understanding the neutrino beam flux is mandatory for MINERνA to measure absolute cross sections. MINERνA uses G4numi, a geant4 (more specifically, geant4 9.2.p03) based MC for the NuMI flux simulation with FTFP_BERT [73] (FRITIOF Precompound and BERTINI cascade) to model the hadron production in the following way:

- The Bertini-style cascade is used for the inelastic scattering of hadrons by nuclei below 5 GeV. Final state hadrons are produced by a classical cascade consisting of individual hadron-nucleon scatterings which use free-space partial cross sections, corrected for various nuclear medium effects [74, 75].
- The FRITIOF model implements inelastic scattering of hadrons by nuclei above 5 GeV. It forms QCD strings by pairing a parton from the projectile hadron with a parton from a target nucleon. The strings are then excited by momentum exchange which can result in diffraction of the target or projectile or both. String masses are sampled and then the strings are decayed using the LUND fragmentation model. After the initial collision, the highly excited remnant nucleus is de-excited using the G4Precompound model [73, 76].

Due to the importance of the flux determination, MINERνA makes use of several tools to constrain its flux:

- **External hadron production data:** the hadronic models are reweighted using proton-carbon hadron production experimental data (see Section 4.1.1).
- **Beam fits to MINERνA detector data:** by producing neutrinos of the same energy using several different beam configurations, it is possible to deconvolve focusing effects, hadron production off of the target, and neutrino cross sections. These flexible beam configurations (a.k.a Special Runs), can be used to tune the hadron production yields to match data from the MINERvA detector.
- **Beam fits to Muon Monitor Data:** the NuMI beamline preceding the MINERνA detector contains four excavated rock alcoves, three of which are instrumented with arrays of ionization chambers and the fourth alcove is currently being instrumented. These alcoves are separated by significant amounts of rock, so each monitor is sensitive to a different muon energy threshold (hence, a different neutrino energy threshold too). The Monte Carlo hadron production model can be tuned to match muon monitor data in the same way we tune it to match MINERvA detector data [77].
- **Standard Candle Method:** MINERνA wants to perform fits on "standard candle" data samples in which the cross section is approximately constant with neutrino energy.

  Neutrino-electron scattering data: $\nu - e$ scattering is a well known interaction that can used to constrain the neutrino flux with this technique [78].

  Low ν Method: this is a sample composed of events with a low energy transfer to the nucleon [79].

Currently only the external hadron production data is used to constrain the flux. Efforts for developing and implementing the other methods are in progress.

4.1.1 Hadron Production Reweighting

MINERνA has found that external hadron production data has, in general, a better agreement with the FTFP_BERT model, which is the reason it was chosen instead of the default physics list model in G4numi (QGSP). However, even though the agreement is better, the discrepancy between external data and the FTFP_BERT is still considerable.

In order to improve the flux prediction, MINERνA reweights the G4numi events according to measurements from proton-carbon hadron production data based on the cross sections for $pC \to \pi^{\pm}X$, $pC \to K^{\pm}X$ and $pC \to p^{\pm}X$ from the following experiments:

- **NA49** experiment at CERN: Data collected at 158 GeV/c beam momentum [80].

- **Barton et al.**: Data collected at 100 GeV/c beam momentum using the Fermilab Single Arm Spectrometer in the M6E beamline [81].

The kinematic region is represented by the following variables:

- x_F: The Feynman scaling variable
- p_T: The transverse momentum

Where, $x_F = \frac{2p_L}{\sqrt{s}}$, and p_L is the outgoing's particle longitudinal momentum and $\sqrt{s}$ is the total center of mass energy.

The corrections applied as a function of x_F are described in Table 4.1. Figure 4.1 shows a comparison of the NA49 data with the FTFP_BERT prediction for $pC \to \pi^{\pm}X$ cross sections, where the focussing peak is in $x_F = [0.05, 0.15]$ and $p_T = [0.1, 0.6]$ as shown in Figure 4.2.

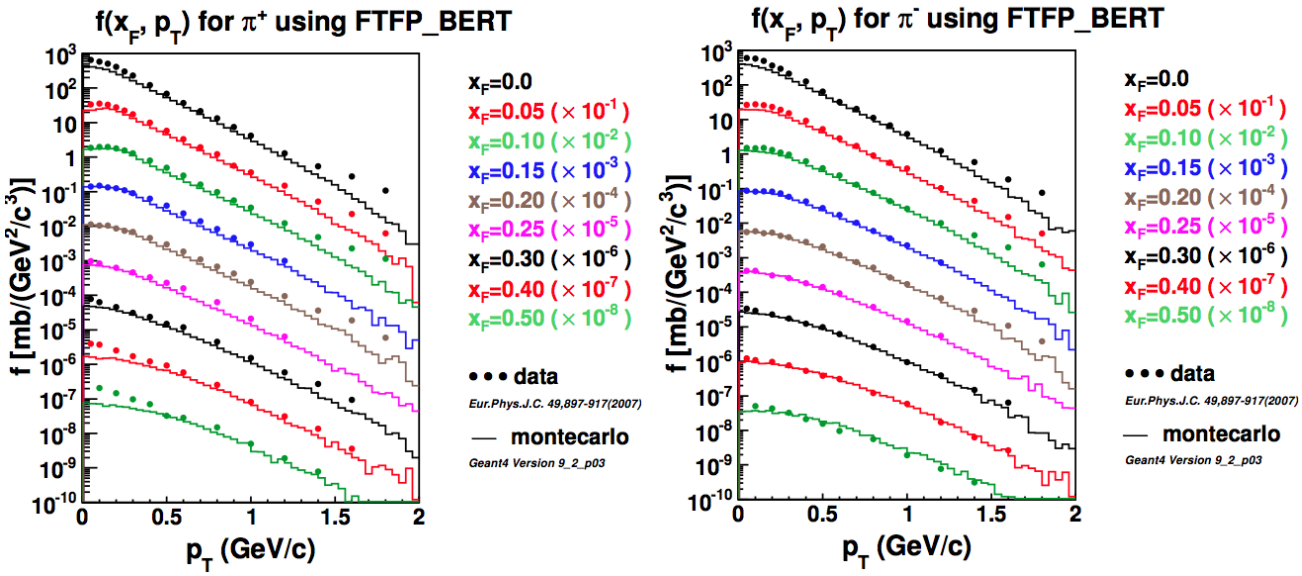

(a) $pC \to \pi^+X$ (b) $pC \to \pi^-X$

Figure 4.1: FTFP_BERT and NA49 data for (left) $pC \to \pi^+X$ and (right) $pC \to \pi^-X$ cross sections.

The reweighting factor for the Barton et.al external data in function of x_F, p_T can be expressed as:

$$w_{\text{Barton et al.}} = \frac{\sigma_{\text{Barton et al.}}(x_F, p_T, E = 100\text{GeV})}{\sigma_{Model}(x_F, p_T, E)} \tag{4.1}$$

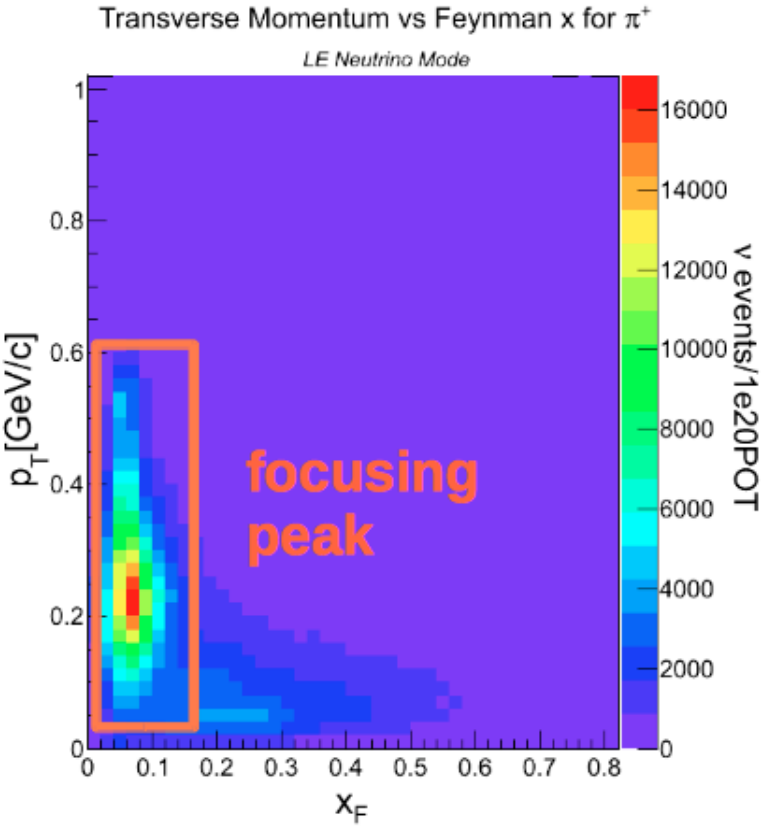

Figure 4.2: Transverse Momentum vs Feynman x for pi^{+}, which makes a ν_{μ} in MINERνA.

The NA49 reweighting factor is additionally re-scaled using predictions from FLUKA [82] (a different hadron production simulation) at the NuMI energies from the NA49 energies (158 GeV) as follows:

$$w_{\mathrm{NA49}} = \frac{\sigma_{\mathrm{NA49}}(x_F, p_T, E = 158\mathrm{GeV})}{\sigma_{Model}(x_F, p_T, E)} \times \frac{\sigma_{FLUKA}(x_F, p_T, E)}{\sigma_{FLUKA}(x_F, p_T, E = 158\mathrm{GeV})} \tag{4.2}$$

Dor the events outside the kinematic region described en Table 4.1, the reweighting factor is simply one.

Cross Section	Kinematics	Dataset
$pC \to \pi^{\pm}X$	$x_F < 0.5$	NA49
$pC \to \pi^{\pm}X$	$x_F > 0.5$	Barton et al.
$pC \to K^{\pm}X$	$x_F < 0.2$	NA49
$pC \to K^{\pm}X$	$x_F < 0.95$	Barton et al.

Table 4.1: A summary of the dataset used to constrain the NuMI flux measurement

The flux weights as a function of neutrino energy are shown in Figure 4.3. The overlay comparisons of the flux before and after reweight corrections can be seen in Figure 4.4.

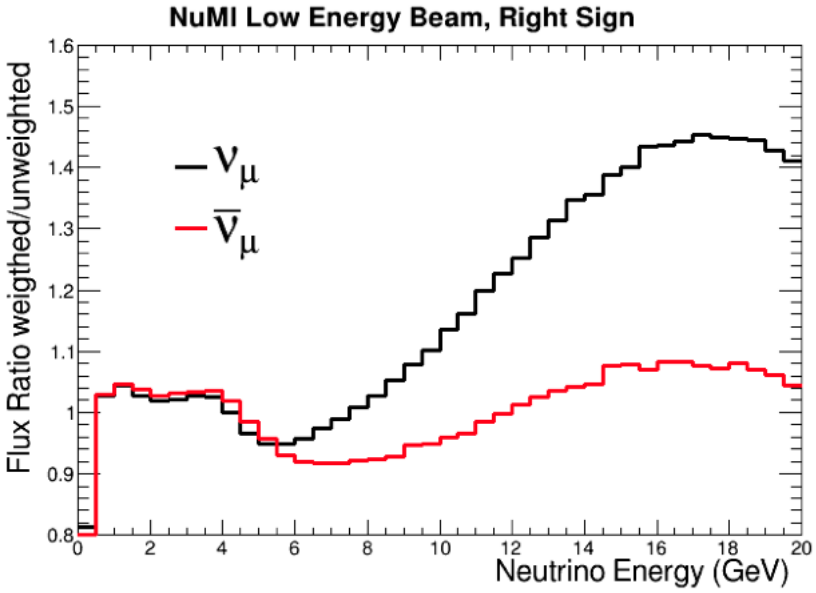

Figure 4.3: Neutrino and anti-neutrino hadron reweight factors

4.2 Neutrino Cross Section Models (GENIE)

The GENIE Neutrino Monte Carlo Event Generator used by MINERνA has different cross section models for each type of interaction process in order to determine which process occurs during the event generation and then the differential distributions for that model is used to determine the event kinematics.

4.2.1 Quasi-Elastic Scattering

The quasi-elastic scattering is modeled according to the Llewellyn-Smith formalism described in Section 2.5.4.1.

The electromagnetic form factors are parametrized using the BBBA2005 model [83]. The pseudo-scalar form factor is assumed to have the form suggested by the partially conserved axial current (PCAC) hypothesis, leaving the axial form factor (see Equation 2.59) as the only remaining unknown factor.

GENIE assumes a dipole form with the axial vector mass M_A remaining as the sole free parameter with a default value of $0.99\text{GeV}/\text{c}^2$.

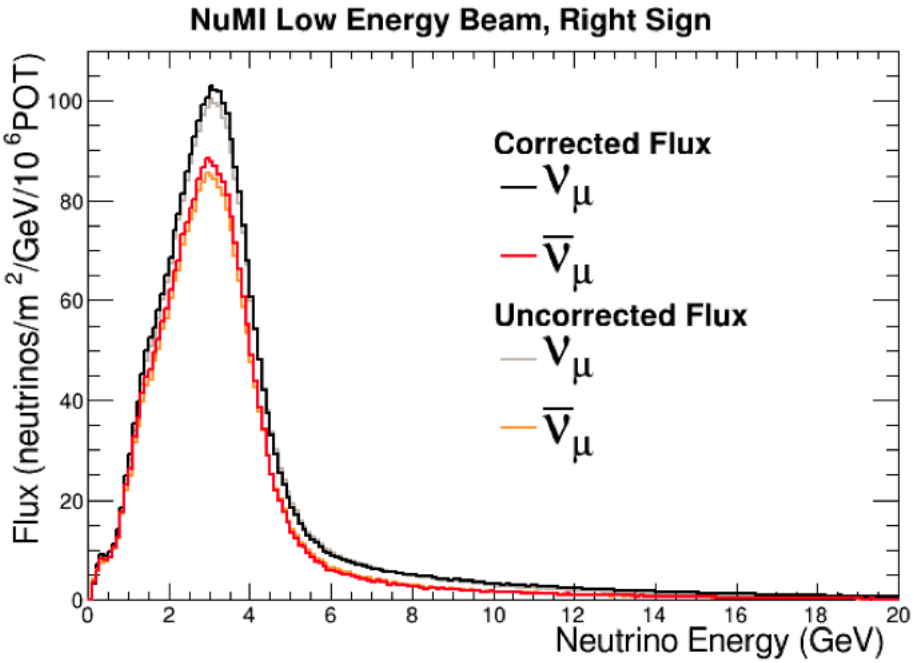

Figure 4.4: Neutrino and anti-neutrino flux: Corrected (after weights applied) vs Uncorrected (before reweights).

4.2.2 Resonance Scattering

The Rein-Sehgal Model is used to simulate this kind of interaction process. The double differential cross section for single meson production in this model is given by [45]:

$$\frac{d^2\sigma}{dQ^2 d\nu} = \frac{1}{32\pi m_N E_\nu^2}\frac{1}{2}\sum_{spins}|T(\nu N \to lN^*)|^2\delta(W^2 - M^2) \tag{4.3}$$

where: $|T(\nu N \to lN^*)|$ is the amplitude of a given resonance production, which is calculated via the Feynman-Kislinger-Ravndal model [84] and W is the hadronic invariant mass.

From the 18 resonances of the Rein-Sehgal model original paper [45], GENIE includes the 16 that are listed as unambiguous at the latest PDG baryon tables and all resonance parameters have been updated. interference between neighboring resonances has been ignored in this implementation of the Rein-Sehgal model. The default value for the resonance axial vector mass M_A is 1.12GeV/c^2 as determined in the global fits carried out in [85] .

4.2.3 Coherent Scattering

The coherent neutrino-nucleus interactions are also modeled according to the Rein-Sehgal model [45].

Since the coherence condition requires a small momentum transfer to the target nucleus, it is a low-Q2 process which is related via PCAC to the pion field. The Rein-Sehgal model begins from the PCAC form at $Q^2 = 0$. Based on the PCAC formalism, the differential cross section for $Q^2 = 0$ is given by:

$$\frac{d^3\sigma(\nu A \to lA\pi)}{dxdydt}|_{Q^2=0} = \frac{G_F^2}{\pi^2} f_\pi^2 m_N E_\nu (1-y) \frac{\sigma(\pi A \to \pi A)}{dt} | E_\nu y = E_\pi \tag{4.4}$$

where G_F is the weak coupling constant, f_π the pion decay constant, m_N is the nucleon mass, ν is the energy transfer, t the square of the four-momentum transferred to the nucleus and the bjorken kinematic variables $x,\ y$ are expressed as:

$$x = \frac{Q^2}{2m_N\nu} \tag{4.5}$$

$$y = \frac{\nu}{E_\nu} \tag{4.6}$$

For values of $Q^2 \neq 0$ the model assumes a dipole dependence with $M_A = 1.00\text{GeV/c}^2$ and calculates the relevant pion-nucleus cross section from measured data on total and inelastic pion scattering from protons and deuterium. The GENIE implementation uses the modified PCAC formula described in a recent revision of the Rein-Sehgal model that includes lepton mass terms [86].

4.2.4 Deep Inelastic Scattering

The deep inelastic scattering (DIS) process is calculated in an effective leading order model using the modifications suggested by Bodek and Yang at low Q^2 [87].

The double differential cross section for this process is calculated as:

$$\frac{d\sigma^2}{dxdy} = \frac{G_F^2 m_N E_\nu}{\pi} \left[\left(1 - y + \frac{1}{2}y^2 + C_1\right) F_2(x) \pm y\left(1 - \frac{1}{2}y + C_2\right) xF_3(x) \right] \tag{4.7}$$

where:

$$C_1 = \frac{m_l^2(y-2)}{4m_N E_\nu x} - \frac{m_N xy}{2E_\nu} - \frac{m_l^2}{4E_\nu^2} \tag{4.8}$$

$$C_2 = -\frac{m_l^2}{4m_N E_\nu x} \tag{4.9}$$

$$\tag{4.10}$$

x, y are the bjorken scaling variables defined in a DIS process as:

$$x = \frac{Q^2}{2m_N(E_\nu - E_l) + m_N^2} \tag{4.11}$$

$$y = \frac{E_\nu - E_l}{E_\nu} \tag{4.12}$$

E_l is the energy of the final state lepton, and $F_2(x), xF_3(x)$ the nucleon structure functions calculated with the GRV98 parton distribution functions [88].

4.2.5 Transition region to DIS

GENIE restricts the resonance production using a hadronic invariant mass cut of $W < 1.7$ and restricts the DIS production using a hadronic invariant mass cut of $W > m_{\Delta^{++}}$ where $m_{\Delta^{++}} = 1.232$GeV [89] so that the RES/DIS mixture in this region agrees with the inclusive cross section data. GENIE also follows NEUGEN procedure [90] for supressing DIS interactions with resonance-like final states $(1\pi, 2\pi)$ in order to avoid double counting.

4.2.6 Hadron Production

The hadronization model determines the final state particles and 4-momenta given the nature of a neutrino-nucleon interaction (CC/NC, $\nu, \bar{\nu}$, target neutron/proton) and the event kinematics (Q^2, W, x, y).

GENIE uses the AGKY model. This model is now the default hadronization model in neutrino Monte Carlo generators. GENIE includes a phenomenological description of the low invariant mass region based on the Koba-Nielsen-Olesen (KNO) scaling [90] and the PYTHIA/JETSET model for higher masses.

The transition from the KNO-based model to the PYTHIA/JETSET model takes place gradually, at an intermediate invariant mass region, ensuring the continuity of all simulated

observables as a function of the invariant mass. The reference [86] (p24-29) gives a detailed description of these models.

4.3 Nuclear Effects

Section 2.5 describes the Neutrino-nucleon scattering processes considering free nucleons. Since nucleons are, in reality, bound to the nuclei GENIE uses the relativistic Fermi Gas Model to account for the corresponding nuclear effects.

4.3.1 Relativistic Fermi Gas Model

In this model, the protons and neutrons are considered as moving freely within the nuclear volume. The system obeys the Fermi-Dirac statistics leading to the Pauli exclusion principle. Neutrons and protons are distinguishable fermions and are therefore situated in two separate potential wells (see Figure 4.5).

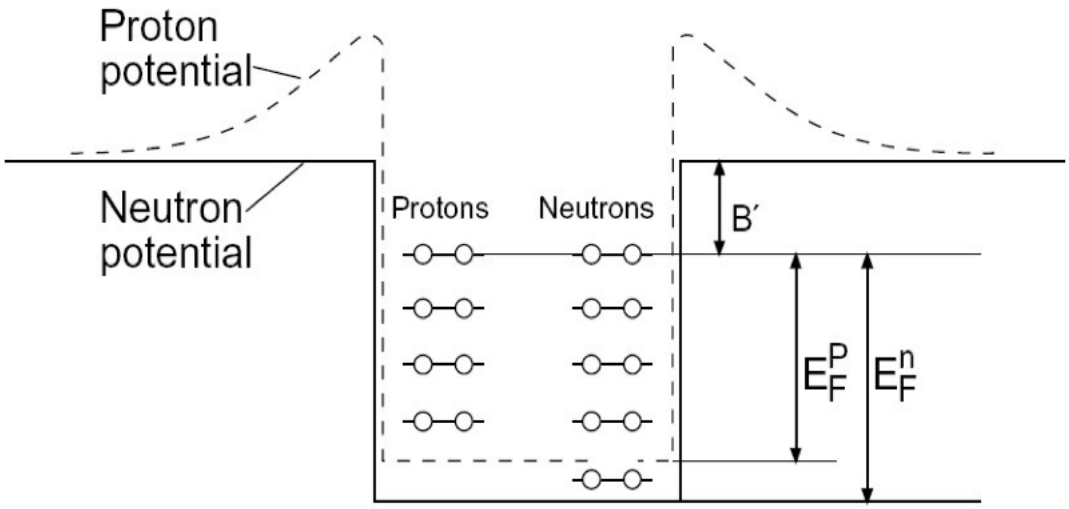

Figure 4.5: Proton and neutron potential wells and states in the Fermi gas model. E_F^p, E_F^n are the Fermi energy of the proton and neutron respectively. B' is the Binding Energy.

The number of states that nucleons in a volume V and a momentum interval dp can have is given by:

$$dn = \frac{4\pi p^2 dp}{(2p\hbar)^3} V \tag{4.13}$$

For the nucleus in its ground state, all states from the minimum momentum up to the maximum momentum will be filled. The maximum level is called the Fermi momentum (p_F). The total number of states is obtained integrating from 0 to p_F:

$$n = \frac{V p_F^3}{6\pi^2\hbar^3} \tag{4.14}$$

As the nucleons have spin-1/2, there are two nucleons for each energy level and hence for each of the nucleon types we have

$$N = \frac{V(P_F^n)^3}{3\pi^2\hbar^3} \quad , \quad Z = \frac{V(P_F^p)^3}{3\pi^2\hbar^3} \tag{4.15}$$

where P_F^n, P_F^p are the fermi momentum for neutrons and protons respectively. If we consider a spherical volume of radius $R = 1.21\ fm$, replace it in Equation 4.15, consider $Z = N = A/2$ and consider that the potential wells for protons and neutrons have the same radius, we get:

$$V = \frac{4}{3}\pi R^3|_{R=1.21fm} \rightarrow P_F = P_F^n = P_F^p = \frac{\hbar}{R}\left(\frac{9\pi}{8}\right)^{1/3}|_{R=1.21fm} \approx 250 \text{ MeV/c} \tag{4.16}$$

and the Fermi energy $E_F = \frac{P_F^2}{2m_N} \approx 33$ MeV. The difference between the edge of the potential and the fermi energy is called binding energy and is constant for most nuclei and equal to the average binding energy per nucleon, which is given by $B/A = 7$ to 8MeV (see Figure 4.5).

In the Fermi gas model a neutrino-nucleon interaction occurs only when the nucleon receives a momentum above the Fermi momentum (because all the states are already occupied). This suppresion is called Pauli blocking.

Although this model provides a good description of the nuclear response it does not account for the effects of dynamical nucleon-nucleon correlations in the initial and final states, which play an important role in specific kinematical regions.

4.3.2 Final State Interactions

GENIE uses Intranuke to simulate final states interactions. When the neutrino interacts with a bound nucleon, the product of these interactions can also interact intra-nuclearly with other nucleons. This is called FSI (final state interactions).

The intra-nuclear interactions of nucleons and mesons produced in neutrino interactions are important nuclear effects to take into account. In particular, pion absorption interactions are

events in which pion is not observed in the final states. A rescattering of protons can also modify the momentum of the particle.

Since all this happens inside the nucleus, it can't be seen by the detector and it can potentially affect the classification of the event type in the analysis (pions absorbed, for example, are an irreducible background in quasi-elastic scattering). For this reason this analysis focuses on a "QE-like" definition, that considers any number of nucleons in the final state but no pions.

CHAPTER 5

Event Reconstruction

5.1 Introduction

This chapter describes the algorithms and techniques based on the location and timing of energy deposition in the detector in order to determine the vertices, trajectories and energies that compose the detector activity originated by the neutrino interactions we aim to study.

This is fundamental in order to understand the nature of neutrinos since these particles, being neutral, can't be directly reconstructed. The neutrino incoming energy is unknown and can only be inferred from the final state particles produced.

5.2 Classification of hits

The reconstruction of events in the detector starts with grouping the collected hits within a gate into different time windows defined as *time slices*. Each time slice generally corresponds to a single physics event like, for instance, the activity due to a neutrino interaction or a rock muon.

Hits within a time slice are spatially grouped within planes into **clusters**. Clusters are classified according to their geometrical position in the detector as:

- Inner Detector Clusters

- Outer Detector Clusters

If groups of clusters are found in the inner detector, and they all together resemble the path of a charged particle, these are then associated into a *track*, which is a three-dimensional object.

After tracks are created, *vertex* objects are associated to the start and end point of each track. If two or more tracks seem to come from the same origin, a single vertex object links these tracks. This is done using a Kalman filter fit [91] to reconstruct the best position for the vertex. The vertex that is identified to the neutrino interaction vertex is called the *primary vertex*.

Different pattern recognition algorithms are applied to these track objects in order to find muon and hadron tracks.

5.2.1 Clustering by Time

A single NuMI beam spill can have multiple event interactions. Hence, dividing the time spill into different slices is important.

In order to do this, a time window of 30 ns is initially taken. If the integrated number of photoelectrons in that window is greater than 10 a candidate time slice is created. The subsequent hits continue to be added to the time slice until the total integrated number of photoelectrons is less than 10. Figure 5.1 shows the time distribution of the hits within a single NuMI beam spill.

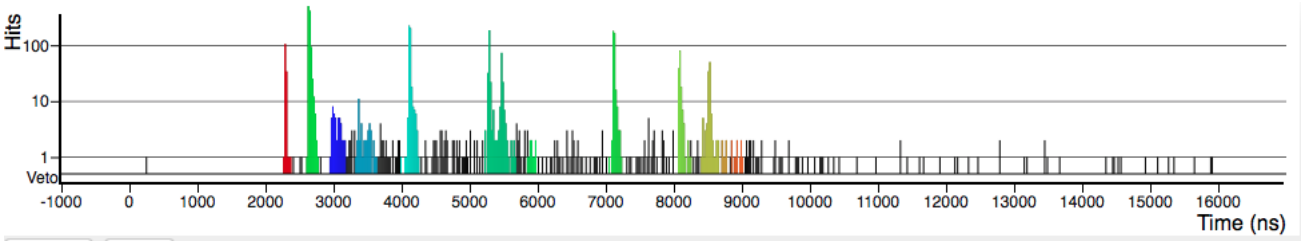

Figure 5.1: Time distribution of hits in a NuMI beam spill. Colored peaks represent the time slices created.

5.2.2 Clustering by Position

Hits are spatially classified by first grouping all hits that are contiguous in position within a plane. If there is a hit isolated from others, that hit composes its own cluster. The time and

energy are defined as follow:

- **Time:** the cluster time is equal to the most energetic hit time in that cluster.
- **Energy:** the energy of the cluster is calculated as the total sum of all energy hits in that cluster.

Additionally, it is known that the topology of each cluster will be different depending on the particles that compose such a cluster. These topologies are classified in the following way:

- **Low Activity:** any cluster with an energy less than 1 MeV.
- **Cross Talk:** each hit in the detector is detected by a specific pixel on a specific PMT. Each hit is mapped to its corresponding PMT pixel and then compared to the neighbor pixels in that PMT. If the photoelectrons measured are consistent with cross talk [92], the cluster is tagged as such.
- **Heavy Ionizing:** clusters with an energy greater than 12 MeV and less than 5 hits. Additionally, at least one hit (but less than four) energy needs to be greater than 0.5 MeV and they all have to be contiguous.
- **Trackable:** clusters whose energy is between 1 and 12 MeV and have less than 5 hits. In addition, at least one hit (but less than three) must have energy between 0.5 MeV and 12 MeV and hits have to be contiguous.
- **Superclusters:** clusters that do not pass the previous categories criteria. These clusters are consistent with electromagnetic or hadronic showers.

5.2.3 Tracking

Clusters that have been created in the *trackable* and *heavy ionizing* category, undergo a series of different algorithms in order to reconstruct a track from it. In this analysis we aim to reconstruct muons and hadrons trajectories.

Muons are minimum ionizing particles that travel without changing its trajectories due to interactions with the detector. Hence, a single track is enough for reconstruction. Hadrons on the other hand, tend to interact more and we must to be able to reconstruct multiple tracks.

5.2.3.1 The Tracking Procedure

The MINERνA framework components designed to reconstruct these trajectories are composed of the *LongTracker* and two *ShortTrackers* algorithms. The first is used to reconstruct the muon and a combination of the three (LongTracker+ShortTrackers) is used to reconstruct hadron trajectories. The sequence in the reconstructor code for this analysis is the following:

- **The Anchor Track:** first the longest track, which most of the time is the muon, is selected as the anchored track using the LongTracker algorithm. This track must have traveled at least 25 planes through the detector or else the event is discarded. The **event vertex** is defined as the origin of the selected anchored track. The clusters not related to this track are then freed so more algorithms can be used on them.

- **The Anchored Tracks:** after the anchor track is created, the LongTracker and ShortTracker algorithms are run on the clusters that were freed and are kept if they are compatible with the event vertex. Compatible here means that:

  (a) the anchored track projection has to be no more than 100 mm away from the event vertex

  (b) its origin has to be less than 250 mm away from the event vertex.

  This is repeated multiple times until there are no more free clusters meeting these requirements.

- **The Secondary Tracks:** after the anchor track and all the anchored tracks are created, the search of tracks continue by looking at the end position of the anchored tracks. The procedure is similar to the anchored tracks with the difference that the anchor point is the end of a track instead of the event vertex. This sequence continues in a loop until no more secondary tracks can be found.

5.2.3.2 The LongTracker

This algorithm looks for tracks in all *seeds* within a single time slice. A *seed* is a group of 3 *trackable* or *heavy ionizing* clusters that meet the following criteria:

- Two clusters in the same plane are not allowed
- Each cluster plane has to be in the same orientation (X, U or V)
- Clusters must be in consecutive planes
- These cluster need to be fitted in a two-dimensional line.

Additionally, only a single cluster is allowed to belong to multiple seeds. These requirements limit seeds to reconstruct tracks with less than 70 degrees with respect to the longitudinal axis.

The seeds with the same plane orientation are then merged to form *track candidates* if they meet the following criteria:

- The slope of the seeds' linear fits are consistent
- The seeds share at least one cluster
- The seeds do not contain different clusters in the same scintillator plane

Each seed can only be used by a single track candidate. After all track candidates are formed they can also be merged. Track candidates are not required to share clusters. The existence of gaps allows the track camdidatres to accurately follow particle trajectories that intersect dead regions in the detector.

Two routines are used in the attempt to form three-dimensional track objects from the track candidates [93].

- The first routine looks for all possible combinations of three candidates in which no two candidates share the same plane orientation. These combinations form a 3D-track if they overlap longitudinally and are mutually consistent with the same three-dimensional line. This routine also searches for particular topologies in which a particle trajectory bends in only two views. In that case, the longer candidate is broken into two shorter candidates and kinked tracks are found.
- The second routine examines all remaining candidates to form all possible combinations of two candidates which do not share the same plane orientation. These are then used to construct a three-dimensional line if they have a similar longitudinal overlap. After this, a search for unused clusters with a position consistent with the candidate pair is performed in the remaining view in order to form a three-dimensional track. This technique is specially powerful for tracking particle trajectories that are obscured by detector activity in one of the three orientations.

The three-dimensional tracks are then fit by a Kalman filter. Figure 5.2 shows the tracking position resolution after the Kalman filter fit.

The track found is then submitted to a procedure called **track cleaning** that:

- removes the energy that is likely to be unrelated to the track.

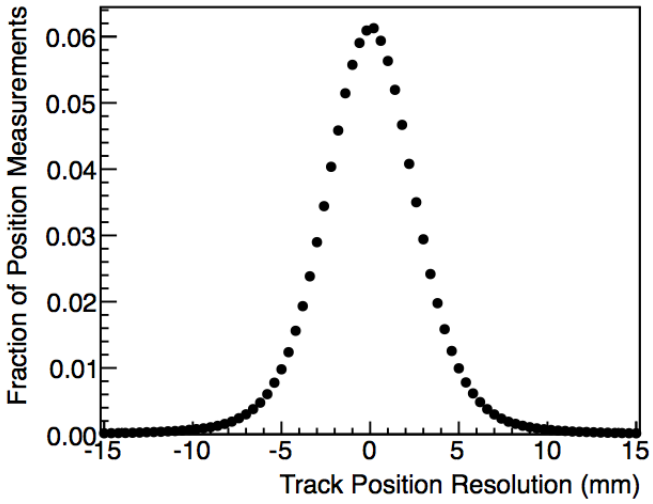

Figure 5.2: Resolution of the fitted positions along a track relative to the measured cluster positions for a sample of data rock muons [93].

- improves the vertex energy measurement.

See reference [93] for a more detailed explanation.

5.2.3.3 The Short Trackers

The short tracker algorithms are effective especially in hadron-like track particles because the energy deposition is greater than the muon and they tend to interact more with the detector and, consequently, are more likely to travel shorter distances. This analysis uses two short tracker algorithms that can reconstruct short trajectories starting with 5 planes or more: the *Vertex Anchored Short Tracker* and the *Vertex Energy Study Tool*.

The Vertex Anchored Short Tracker

MINERνA needs at least four clusters to form a three-dimensional track. This algorithm uses three-dimensional seeds constructed from four clusters in consecutive planes as long as they follow one of the following patterns: XUXV, XVXU, UXVX, VXUX.

Once the seeds are constructed, the short tracker tries to merge the seeds into longer tracks. The following conditions are necessary:

- Seeds need to share one or more clusters
- Polar angles have to be of similar order

- Resemble a straight line
- Pass a Kalman filter fit with a $\chi^2 < 10$

This procedure is repeated until no more seeds can be merged.

The Vertex Energy Study Tool

This short tracker uses a Hough transform to reconstruct three-dimensional tracks [94]. It works as an angle scanner between the anchor track and the ID Clusters. This algorithm increases the reconstruction efficiency especially near the vertex, since the track needs to pass through the anchor vertex and have a cluster near the reconstructed vertex.

5.3 Muon Reconstruction

Since MINERνA is not magnetized we must rely on the MINOS near detector to determine the charge and momentum of muons exiting the MINERνA detector and entering MINOS.

In order for tracks in MINERνA and MINOS to be matched and merged into a muon candidate, the following conditions are required:

- The difference in time between both tracks has to be less than 200 ns.
- The MINERνA track must have activity in at least one of the five last modules of the detector.
- The MINOS track must start within one of the four first planes of MINOS.

Due to these requirements this technique accepts muons within 20 degrees scattering angle with respect to the Z-axis.

There are two methods used to match tracks [93]:

- **Track projection method:** the MINOS track is extrapolated to the plane that contains the last activity on a MINERνA track and the MINERνA track is extrapolated to the plane that contains the start of the MINOS track. The distance between the most downstream activity from the MINERνA track and the start of the MINOS track must be smaller than 40 cm to be considered as a matched.

- **Closest Approach Method:** if the previous method does not find matched tracks, the MINOS track is projected towards MINERνA and the MINERνA track towards MINOS and the point of the closest approach of the two tracks is found. This is especially useful if the muon undergoes a hard scatter in the passive material between the two detectors (i.e the MINERνA detector support structure).

The charge is inferred by the deflection of the muon due to the MINOS magnetic field. The momentum in MINOS is determined by two different methods:

- **Range Method:** this is based on the total energy loss through interactions in the MINOS detector and is applied to muons contained inside the calorimeter region. The momentum is calculated by integration of this energy loss.

- **Curvature Method:** this methods reconstructs the momentum by relating the curvature of the track (K), the magnetic field (B) and the momentum component perpendicular to the field (P) as follows:

$$K = \frac{1}{R} = \frac{0.3B}{P_\mu} \tag{5.1}$$

where R is the radius of curvature.

5.4 Proton Reconstruction

The fine granularity and light yield of the MINERνA detector makes it possible to use dE/dX profiles near the ends of the reconstructed tracks to identify particles that stop in he detector (see section 10.2 of [93]).

In cases where the hadron loses energy via electromagnetic processes, decays in flight, elastic scattering or minimum inelastic hadron scattering, the dE/dX can differentiate between minimum and heavily ionizing particles. However, hadrons can interact or be absorbed in the detector too, which affects the performance of this technique for such cases.

For each track found using the algorithms described in in Sections 5.2.3.2 and 5.2.3.3, a χ^2 is determined by comparing the energy deposited per scintillator plane to templates derived from the dE/dX profile expected in the detector for different momenta and for two different types: protons and pions. Figure 5.3 shows the dE/dx profile for a proton compared to the pion and proton templates. The profile is gotten from a reconstructed track in data, where the measured proton momentum is 1 GeV/c and the $\chi^2/ndf = 29/33$.

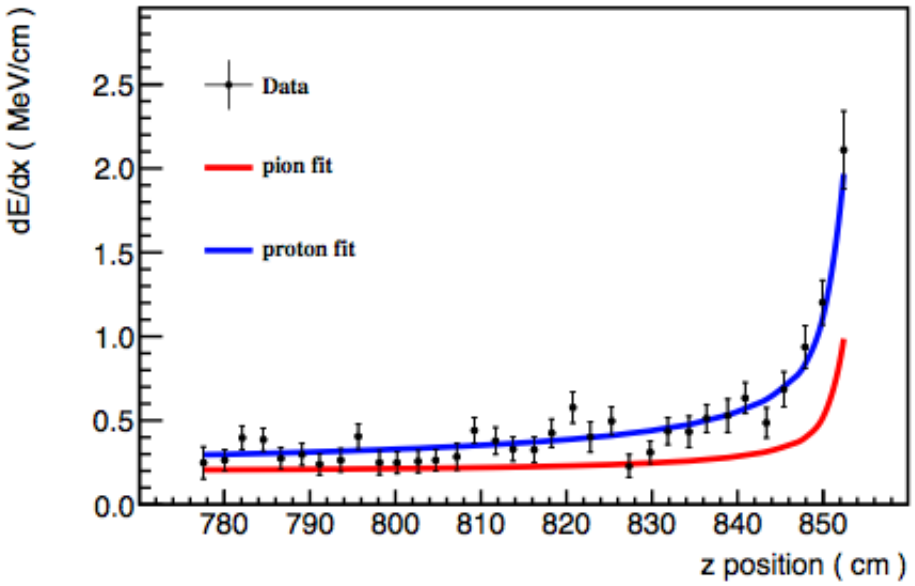

Figure 5.3: dE/dx profiles for an identified proton in data.

A particle score is then computed based on the χ^2/ndf between data and these profiles as follows:

$$\texttt{particle score}_{p(\pi)} = \frac{(\chi^2/ndf)^2_{p(\pi)}}{\sqrt{(\chi^2/ndf)^2_p + (\chi^2/ndf)^2_\pi}} \tag{5.2}$$

The dE/dx is also used to measure the energy of stopping particles more precisely than a simple calorimetric energy sum. Figure 5.4 shows the momentum resolution for protons and pions from simulated reconstructed tracks stopping in the detector.

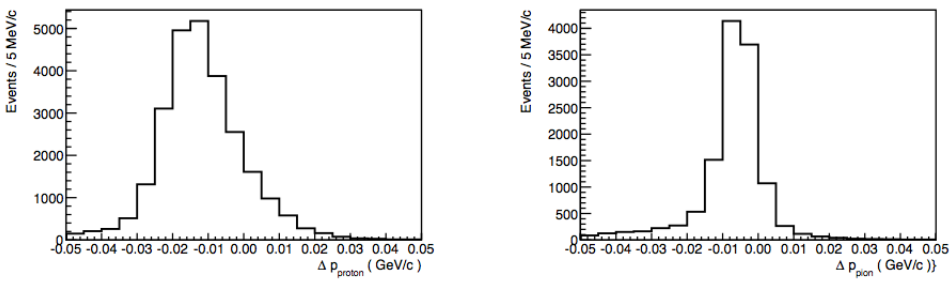

Figure 5.4: Momentum resolution (reconstructed momentum - true momentum) for protons (left) and pions (right) from simulated reconstructed tracks stopping in the detector.

5.5 Michel Electrons Reconstruction

A Michel electron is an electron produced by the decay of a muon . Muons are unstable elementary particles that decay via the weak interaction. The dominant muon decay is shown in equation 5.3, this decay is also known as the "Michel decay", named after Louis Michel (See reference [95]).

$$\mu^+ \rightarrow e^+ \nu_e \bar{\nu_\mu} \ , \ \mu^- \rightarrow e^- \bar{\nu}_e \nu_\mu \tag{5.3}$$

Michel electrons are reconstructed in order to veto events with soft pions in the final state that decay into michel electrons (via: $\pi^+ \rightarrow \mu^+ \nu_\mu$ and then: $\mu^+ \rightarrow e^+ \nu_e \bar{\nu_\mu}$).

A Michel electron is identified by searching for a delayed signal near the endpoint of a stopped muon track. However, isolated energy depositions in time slices with no other detector activity are found predominantly due to delayed Michel electrons. Because of this, the full sample of such energy depositions can be used without requiring a precursor muon. Figure 5.5 shows the energy spectrum of michel electrons in data and Montecarlo. The mean value of both distributions show an agreement within 3% (see reference [93]).

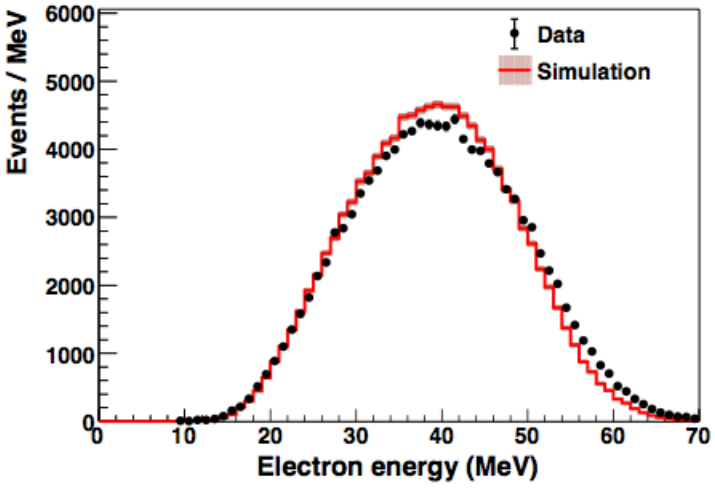

Figure 5.5: Michel electron energy distribution for data and Montecarlo.

5.6 Recoil Energy Reconstruction

The recoil energy is calculated using a simple calorimetric sum of the clusters not associated with the muon. In this analysis, the selected clusters are also outside a region near the vertex

(see Section 6.3.11). This is done because the MonteCarlo does not fully simulate some of the potential hadronic final states in the event. By isolating this region the analysis remains insensitive to those effects.

The calorimetric constants are determined by the dE/dx of a minimum ionizing particle at normal incidence. For a given sub-detector, the calorimetric constants are given by:

$$C^{sd} = \frac{E_{abs} + E_{sc}}{f \times E_{sc}} \tag{5.4}$$

where E_{abs} is the energy loss on one absorber plane, E_{sc} the energy loss in one scintillator plane and f is the active fraction of the scintillator plane in that sub-detector. The sub-detectors are: Central Tracking Region, ECAL and HCAL. For the Tracking region, $E_{abs} = 0, E_{sc} = 1, f = 0.8185$, so $C^{sd} = 1/f = 1.222$. For the ECAL and HCAL, the constants are 2.013 and 10.314 respectively.

The calorimetric energy is then reconstructed as:

$$E^{cal}_{recoil} = \beta \left(\alpha \times \sum_i C^{sd}_i E_i \right) \tag{5.5}$$

where α is an overall scale calculated by minimizing the difference between the sum term and the true value of E_{recoil}. β is an energy-dependent scale that increases agreement with the true simulated recoil energy. For simulated charged current events with MINOS-matched muons and event vertices inside the fiducial tracker region $\alpha = 1.568$ and the energy resolution is $\sigma/E = 0.134 \oplus 0.290/\sqrt{E}$ (see Figure 5.6).

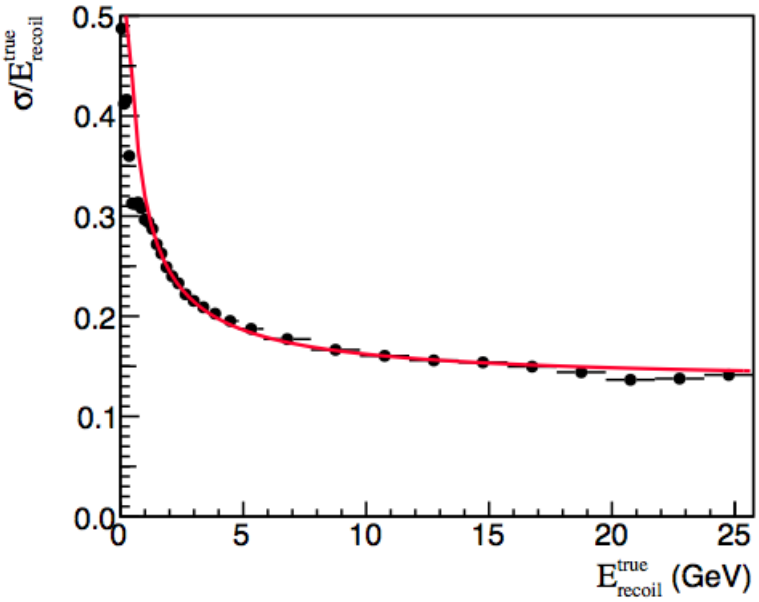

Figure 5.6: Calorimetric energy resolution for simulated charged-current inclusive neutrino events. The dots show the width of a Gaussian fit to the difference between the measured and true recoil energy divided by the true recoil energy, binned by true recoil energy. The line represents a functional fit, $\sigma/E = 0.134 \oplus 0.290/\sqrt{E}$.

CHAPTER 6

Event Sample and Selection

6.1 Event Sample

6.1.1 Monte Carlo

The MINERνA experiment Monte Carlo is implemented via GENIE[96] and GEANT4 [97].

The GENIE Neutrino Monte Carlo Event Generator is used to implement several neutrino cross section models. Section 4.2 describes the different physics channels implemented in GENIE and how it handles the nuclear effects due to the fact that nucleons are bound to the nuclei.

The Geant4 version 9.2 p03 is used to simulate the NuMI Beamline via the G4Numi package. Section 4.1 has a description of the physics model used for the hadron production as well as a descrition of different techniques used to constrain the simulated flux with external hadron data. Geant4 is also used to simulate the passage of final state particles generated by GENIE through the MINERνA detector and to simulate the optical system and electronics used for readout of the scintillator strips. See reference [98] for a detailed description.

The generated event sample used in this analysis corresponds to 1.84×10^{21} protons on target (POT), which is a equivalent to about 6.2 times the data amount.

When Monte Carlo and Data are presented together, Monte Carlo is either POT Normalized (Equation 6.1) or Area Normalized (Equation 6.2).

$$MC_{ABS}^{Norm} = \frac{POT_{DATA}}{POT_{MC}} \tag{6.1}$$

$$MC_{AREA}^{Norm} = \frac{\#Events_{DATA}}{\#Events_{MC}} \tag{6.2}$$

6.1.2 Data Set

MINERνA started collecting data in November 2009. The Low Energy Run (LE) data set refers to the data taken between the fall of 2009 and April of 2012 (see Figure 6.1). The accelerator complex was then shut down and underwent an upgrade necessary for the Medium Energy Run. data taking restarted in September 2013 and will continue for about five more years.

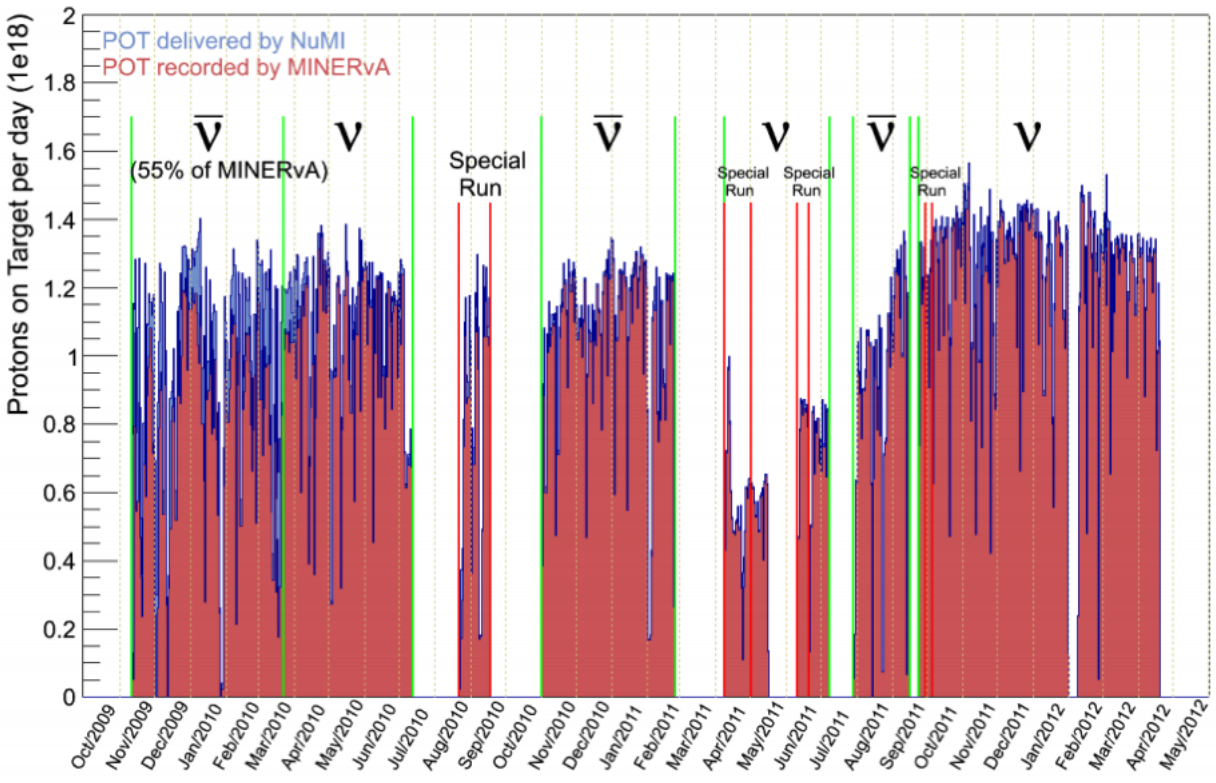

Figure 6.1: Neutrino beam data recoded by MINERνA .

In November 2009 MINERνA started taking anti-neutrino data with about $\tilde{5}5\%$ of the full detector installed. The detector was gradually completed untill reaching 100 % in March 2010. This data set is known as the *frozen detector data*.

With the full detector in place MINERνA took data from March 2010 to July 2010 and

then switched between neutrino and anti-neutrino for different periods. Data with different beam configurations were also taken in order to constrain the hadron production model. These are called *Special Runs* (see Section 4.1).

The first publication [64] uses the neutrino data from March to July 2010. This analysis uses the whole neutrino low energy data taken from March 2010 to April 2012, which is equivalent to 2.95×10^{20} protons on target.

6.2 The Quasi-Elastic Like Signal

A neutrino charged current quasi-elastic event occurs when a neutrino scatters off a free or bound nucleon via the exchange of a charge vector boson $W^{\pm}$. However, this boson can be absorbed by a nucleon-nucleon correlated pair or coupled with a virtual meson, as discussed in Sections 2.6, 2.7 and 4.3.2.

This analysis aims to measure *Quasi-Elastic Like* events, which are the kind of events the detector is able to see. A neutrino charged current *Quasi-Elasic Like* event is an event with:

- one negative charged muon
- no mesons in the final state
- any number of nucleons (protons, neutrons)

6.3 Event Selection

Charged current events originating from neutrino interactions inside MINERνA are the starting point of the event selection procedure needed for this analysis. The ultimate goal is to obtain charged current events that bear a topology similar to those from quasi-elastic interactions. A number of selection criteria are imposed for obtaining events that meet this requirement. They are enumerated and explained below in chronological order as present in the analysis.

6.3.1 Fiducial Volume

The fiducial volume is several modules long, along the length of the detector. It extends from module 27 to module 80. Based on a coordinate system that has its origin at the most upstream module of the MINERνA detector this extends for almost 2.5 m from 5990.0 mm to 8410.0 mm.

The maximum extent in the X-Y plane, perpendicular to the length of the detector (Z axis), is required to be no more than 850.0 mm. This is referred to as the apothem. This

fiducial volume requirement leads to most of the event information being present inside a well understood and calibrated region of the detector and avoids edge effects or escape of considerable information near the edges of the detector.

All the neutrino interactions that will be considered are required to originate inside this volume.

6.3.2 MINOS Matching

Each event should come from a charged current interaction. This means that the neutrino picks up charge and converts into a lepton as it interacts with the detector material.

Since the neutrinos from the NuMI beam line are mostly muon neutrinos in nature, they will produce muons. Each muon originating inside MINERνA from a neutrino interaction vertex is considered as the primary muon and must be matched to a corresponding muon track in the MINOS detector. Since the MINOS detector is magnetized the muon momentum and charge can be obtained from the track curvature inside MINOS.

A metric based on the derived charge (q) and momentum (p) information is used for selecting muons (as compared to anti-muons). Figure 6.2 shows a schematic of a quasi-elastic event, with a muon going into the MINOS near detector. See section 5.3 for details about the muon reconstruction.

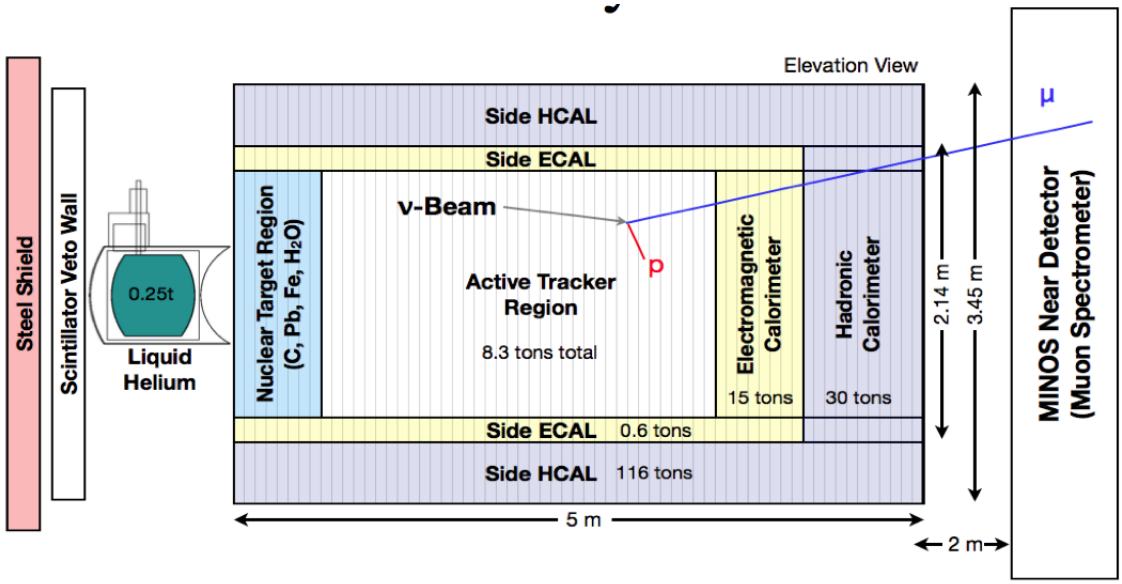

Figure 6.2: Schematic of a quasi-elastic event in the MINERνA detector. The event interaction vertex is inside the fiducial volume, the muon is going into the MINOS Near Detector and the proton is contained in the MINERνA detector.

6.3.3 Insensitive Electronic Regions in Detector

The MINERνA readout electronics has a charge integration time of 150 ns followed by 200 ns of reset time [72]. Blocks of channels linked to the same front-end electronics have little to no readout sensitivity during this reset time. If a second event occurs anytime during the 200 ns of reset time, very close in electronics space to the first event, little to no information from the second event will be read out during the reset mode. This incomplete readout of event information can lead to the presence of a background. For e.g. a rock muon[1] entering through the front of MINERνA can appear like a muon originating from a neutrino interaction inside the detector from this incomplete information readout.

In order to minimize these backgrounds, a minimum number of insensitive channels are required in the event selection. The projection of a reconstructed muon track to the most upstream face of the detector should bear no more than one insensitive channel in its path for this analysis.

6.3.4 Neutrino Helicity

Since this analysis aims to measure a cross-section for neutrino interactions, a requirement on the neutrino helicity is imposed for selecting neutrino events. The neutrino helicity is determined from a metric derived from the charge and momentum measurements of the muon track that enters MINOS.

6.3.5 Event Multiplicity

This analysis considers charged current, quasi-elastic topology-like events. This means that the proton produced as a result of the neutrino interaction can be above or below the tracking threshold of the MINERνA detector.

If the proton is below tracking threshold, it will not be tracked. The event bears a single reconstructed track due to the muon, has multiplicity equal to 1 and pass the multiplicity cut. If the proton is above tracking threshold, it can be tracked and identified as a proton. The event then has two tracks (one from the muon and one from the proton). Its multiplicity is 2 and the event pass the multiplicity cut. Events with multiple reconstructed tracks identified as protons possess multiplicity > 2 and are also selected.

Figure 6.3 shows the the multiplicity of the event sample. Although most events have 1 or 2 outgoing tracks the log-scale version of the plot shows there could be events with up to 6 tracks.

[1] A rock muon is a muon that reaches MINERνA coming from the rock that surrounds the detector.

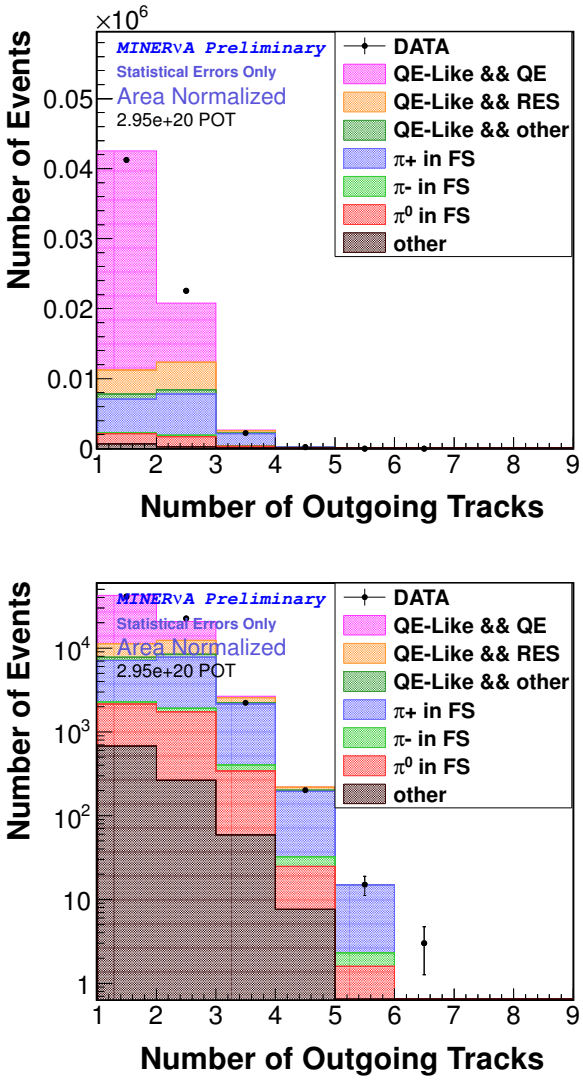

Figure 6.3: Multiplicity or number of outgoing tracks (top) and its logY scale version (bottom).

6.3.6 Primary Proton Identification

All reconstructed non-primary-muon tracks are required to pass the proton identification selection criteria. This identification is based on a metric derived from the energy loss profile (dE/dx) tool (see Section 5.4). Based on how closely the energy loss profile of a non-primary-muon track resembles that of a decelerating pion or proton, the dE/dx tool returns its best guess of the type of particle associated with the track. This metric is referred to as the proton "dE/dx score" (see Equation 5.2) and it ranges in values from 0.0 to 1.0. High proton scores, e.g. 0.8 or higher, signify a well identified proton track. Low proton scores, e.g. 0.2 or lower, point to particle tracks that are probably not protons but, maybe pions or electrons.

The most energetic proton in the event is designated as the primary proton. The identification on the basis of proton scores is a sliding cut and depends on the four-momentum transfer

(Q^2) of the event as shown in Table 6.1 (appendix A shows the proton range score for each Q^2 range in the table). This sliding cut is introduced in an effort to include protons from high Q^2 events which might endure multiple scattering or interactions and then be identified with low scores. As larger the four-momentum transfer of the event, lower is the score for protons reconstructed in that event. Including these protons bolsters the efficiency of the event selection by about 30%, but has a small effect on the decrease of purity, that is about 5%.

Q^2(GeV)	Proton Range Score
0.0-0.3	0.35
0.03-0.05	0.35
0.05-0.1	0.35
0.1-0.2	0.35
0.2-0.4	0.30
0.4-0.8	0.25
0.8-1.2	0.0
1.2-2.0	0.0

Table 6.1: Proton Range Score vs Q^2 cut.

6.3.7 Secondary Proton Identification

As mentioned in section 6.3.6, if an event possesses more than one reconstructed non-primary-muon track, all the tracks are subject to identification for protons. The dEdx scores criteria for identifying the secondary protons is exactly the same used for the primary protons. The secondary protons have less kinetic energy than the primary proton in the event.

6.3.8 Isolated Blobs

Since the events considered for this analysis should have topologies similar to those from quasi-elastic interactions, there is a minimum number of shower-like activity regions that can be present in the event. "Blob" are how MINERνA calls a group of clusters that arise from shower-like activity in the detector medium. These clusters are topologically connected (close to each other) and each group is distinct and away from the other groups. Such blobs are referred to as the isolated blobs.

This analysis considers isolated blobs located far away from the neutrino interaction vertex while using them as a topological cut for selecting quasi-elastic-like events (see Figure 6.4). Only one such isolated blob per event is permitted.

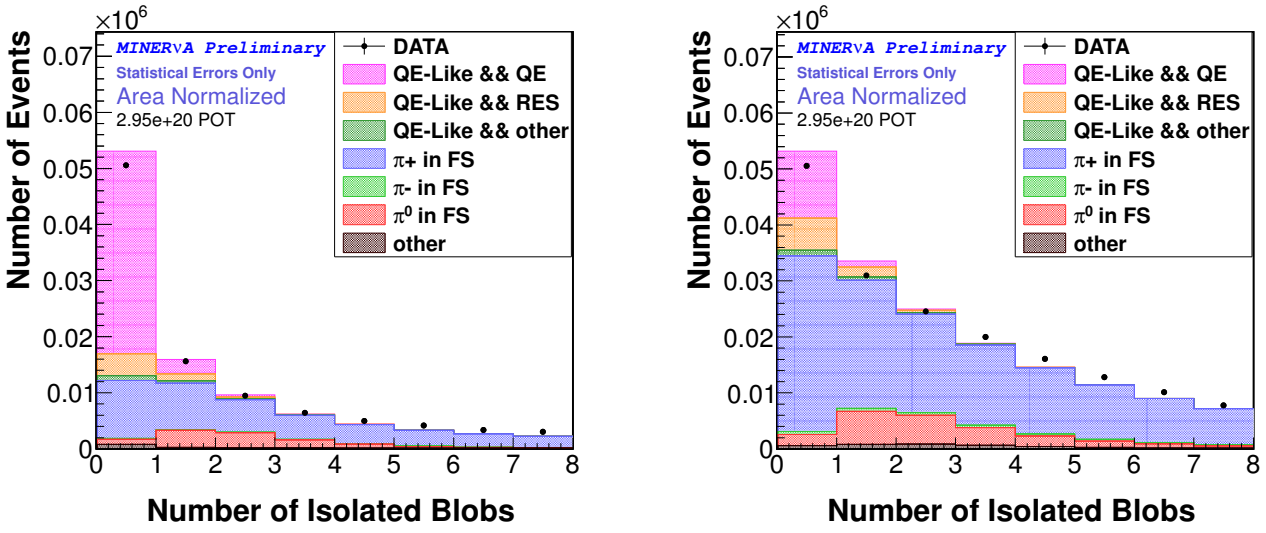

Figure 6.4: Number of isolated blobs. (a) Events with where only the muon was reconstructed. (b) Events with a muon and at least one proton candidate reconstructed.

6.3.9 Michel Electrons

Muons decay to Michel electrons. Leptonic decays of pions produce muons which in turn produce Michel electrons. Protons do not produce Michel electrons. Thus the presence of Michel electrons are a distinguishing indicator of the presence of pions and (or) muons in an event.

The event selection requires a search for these Michel electrons in the event (see Section 5.5 for details on the reconstruction). The searches are conducted at the neutrino interaction vertex and at the end of each non-primary-muon track. If a Michel electron is found, the event is tagged. Events bearing a Michel tag are indicative of the presence of pions and are not considered for this analysis.

Figure 6.5 shows the events that were vetoed by this criteria as a function of the longitudinal muon momentum.

6.3.10 Neutrino Energy

The reconstructed neutrino energy is required to be between 1.5 GeV and 10.0 GeV. The lower limit of 1.5 GeV ensures that the muon resulting from the neutrino interaction traverses MINERνA and enters MINOS for the charge and momentum measurements. The upper limit of 10.0 GeV gets rid of high energy neutrinos which mostly interact with the partons and not via quasi-elastic interactions.

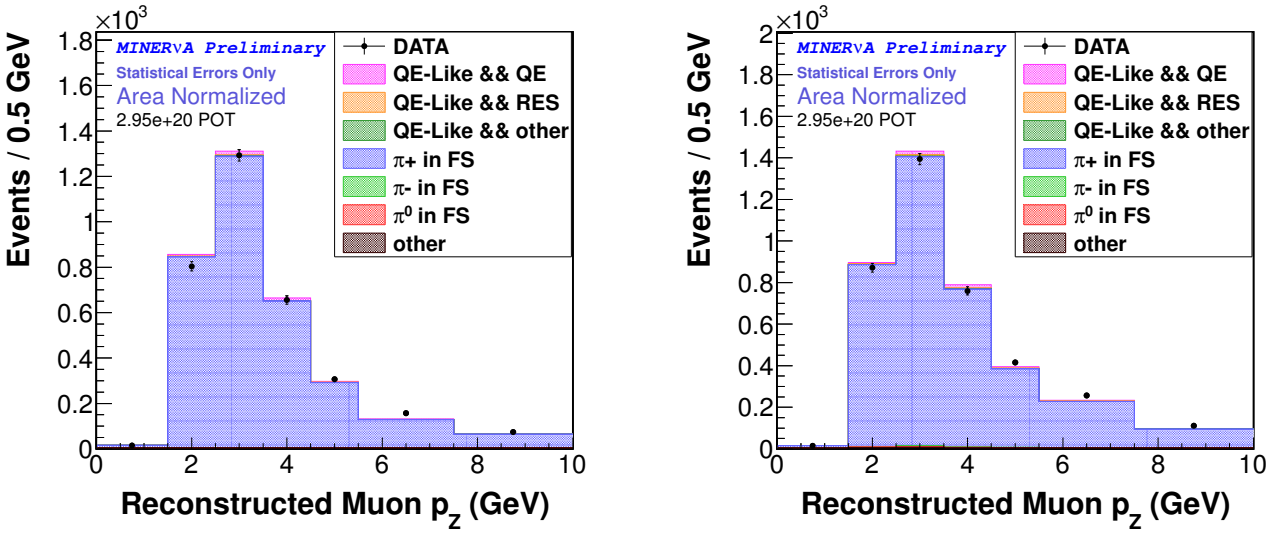

Figure 6.5: Events with at least one michel electron vetoed from the selection.(a) Events with where only the muon was reconstructed. (b) Events with a muon and at least one proton candidate reconstructed.

6.3.11 Recoil Away From The Interaction Vertex

Quasi-elastic interactions are consistent with low recoils. For this analysis the recoil in the reconstructed events is split into two, depending on their location from the interaction vertex. The recoil within a certain designated radius of the interaction vertex is designated as the "vertex recoil". The event selection criteria is insensitive to this vertex recoil, in an effort to avoid biases arising due to differences between the simulation and data. The "non-vertex recoil", is present away from the designated vertex region and is used for deciding which events to keep.

A parametrization of the non-vertex recoil as a function of the reconstructed Q^2 of the event is obtained by studying the non-vertex recoil of events whose topologies are similar to those of quasi-elastic interactions. If the event under consideration possesses a non-vertex recoil that is less than that predicted by the parametrization at its reconstructed Q^2, it passes this selection criteria. If the non-vertex recoil is larger than what the parametrization predicts, the event is discarded. Figure 6.6 shows the parametrization split in two sub-samples: the first sub-sample is for events with only one muon reconstructed and the second sub-sample is for events where there is at least one proton reconstructed. Appendix B shows the plots used to estimate the parametrization.

Figure 6.7 shows a data event candidate after passing all event selection cuts. The long track is the muon going into MINOS and the short track is the proton candidate.

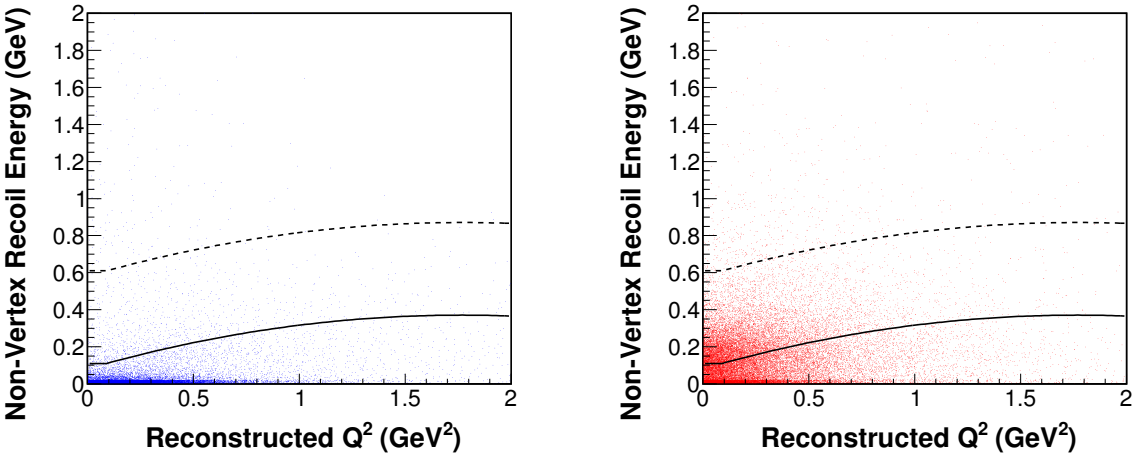

(a) Events with where only the muon was reconstructed.

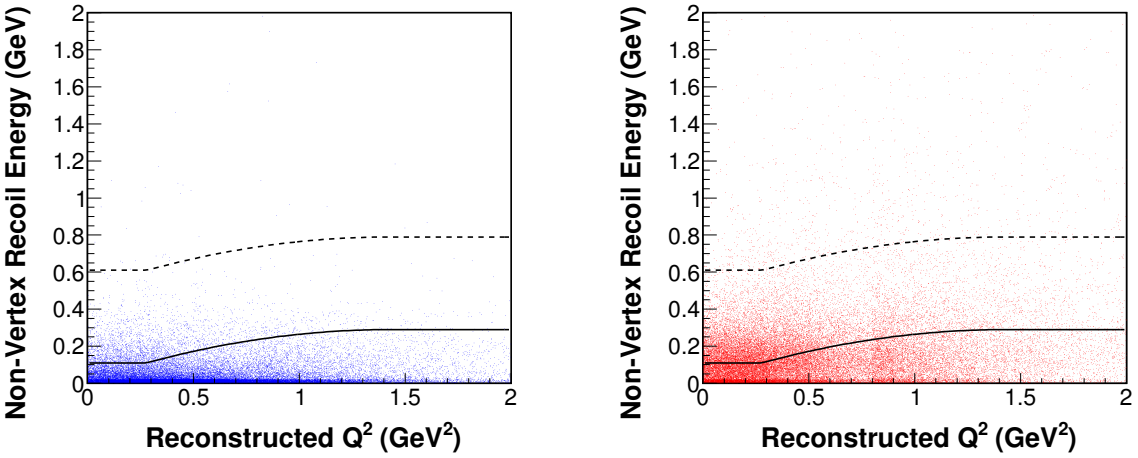

(b) Events with a muon and at least one proton candidate reconstructed.

Figure 6.6: Recoil Energy cut as a function of Q^2. The plots on the left show the quasi-elastic-like events (blue dots) in this phase space and the plots on the right the background (not quasi-elastic-like events). Events below the solid line are accepted. The dotted line is just a reference above 500 MeV.

Figures 6.8 and 6.9 show the Data and Monte Carlo after passing all event selection criteria for the sub-sample where only the muon was reconstructed ($\mu + X$) and the sub-sample where the muon and at least one proton was reconstructed ($\mu + p + X$). The total number of quasi-elastic like event candidates is 20,778 and the estimated purity is 74%.

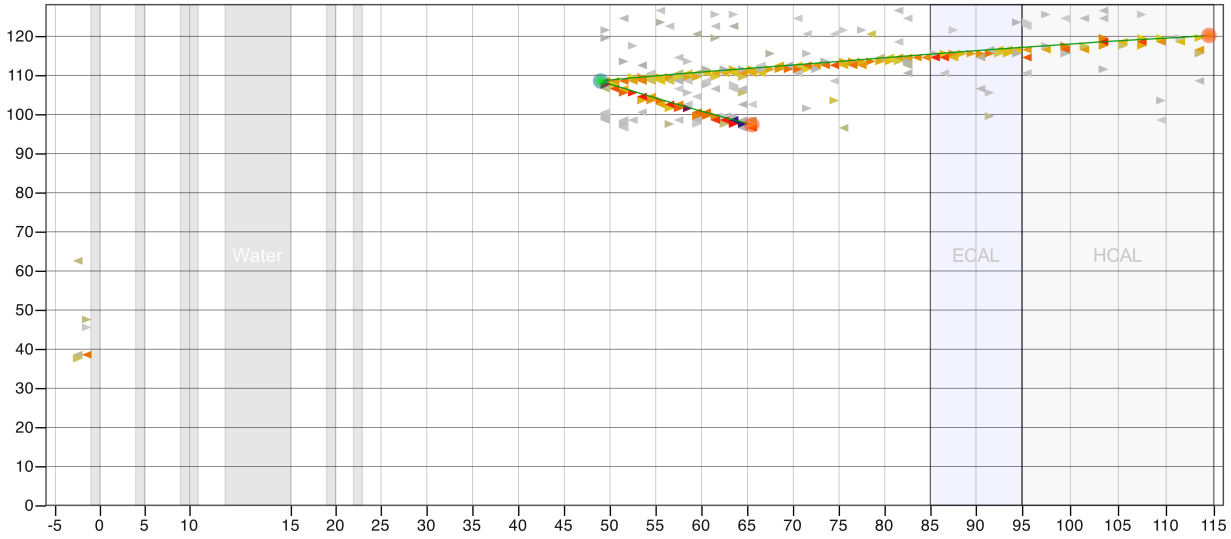

(a) X View

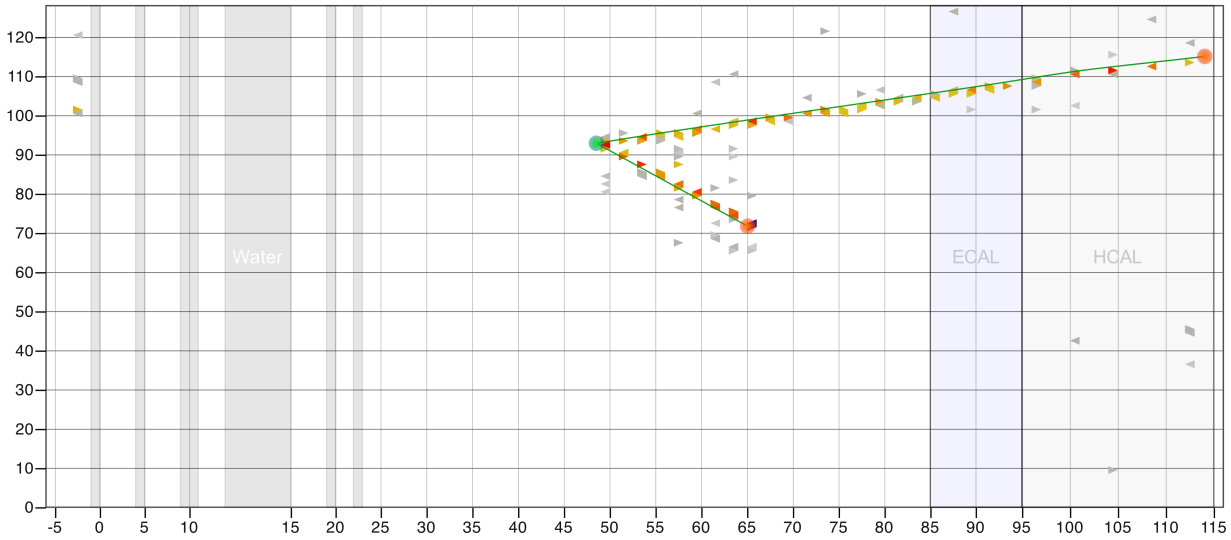

(b) U View

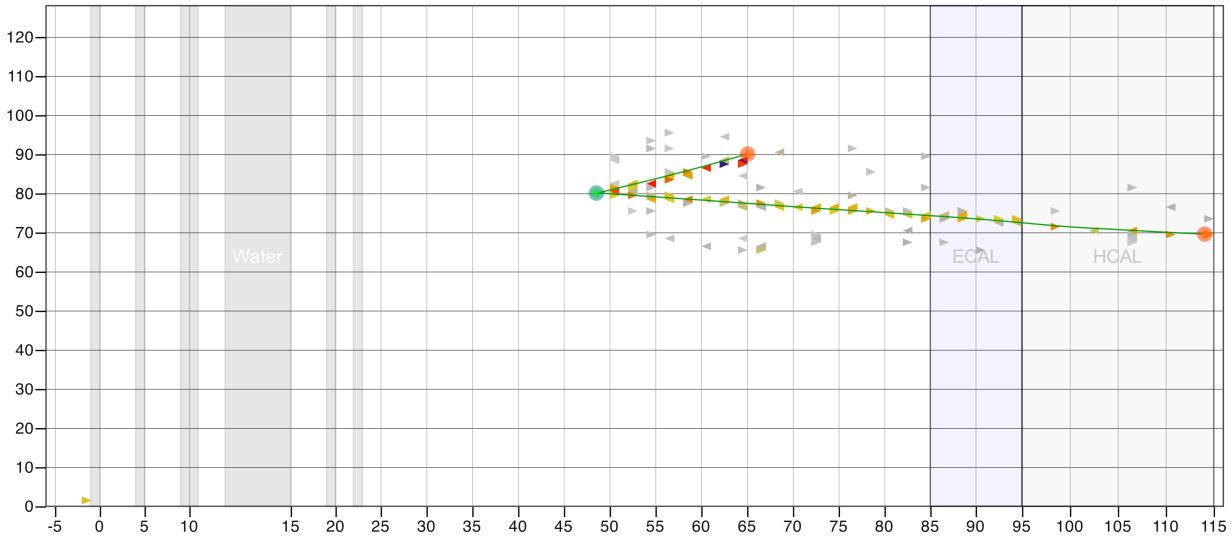

(c) V View

Figure 6.7: Event display candidate after passing all selection criteria.

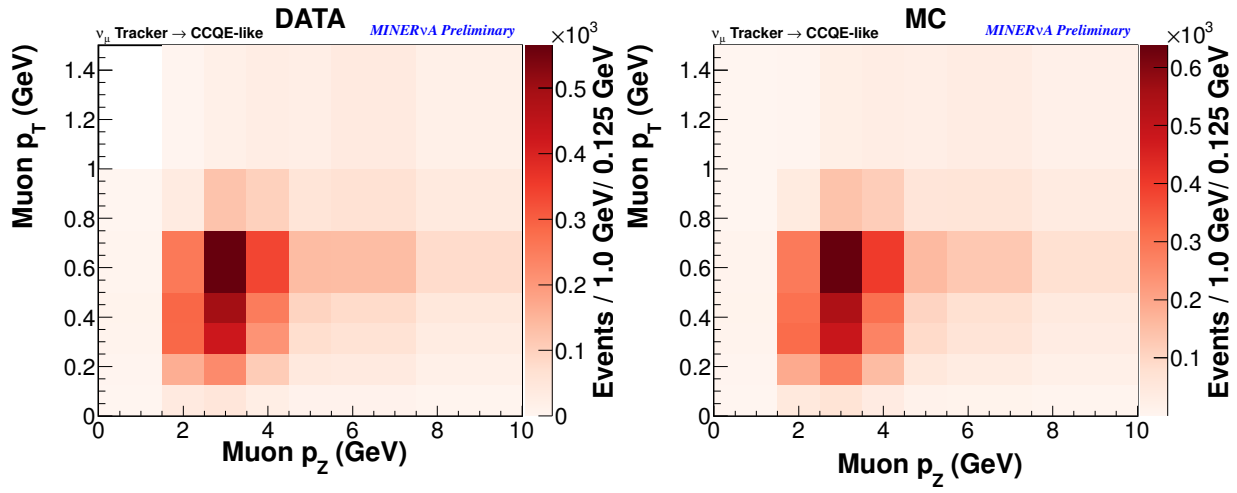

(a) DATA (left) and MC (right) 2-D distributions.

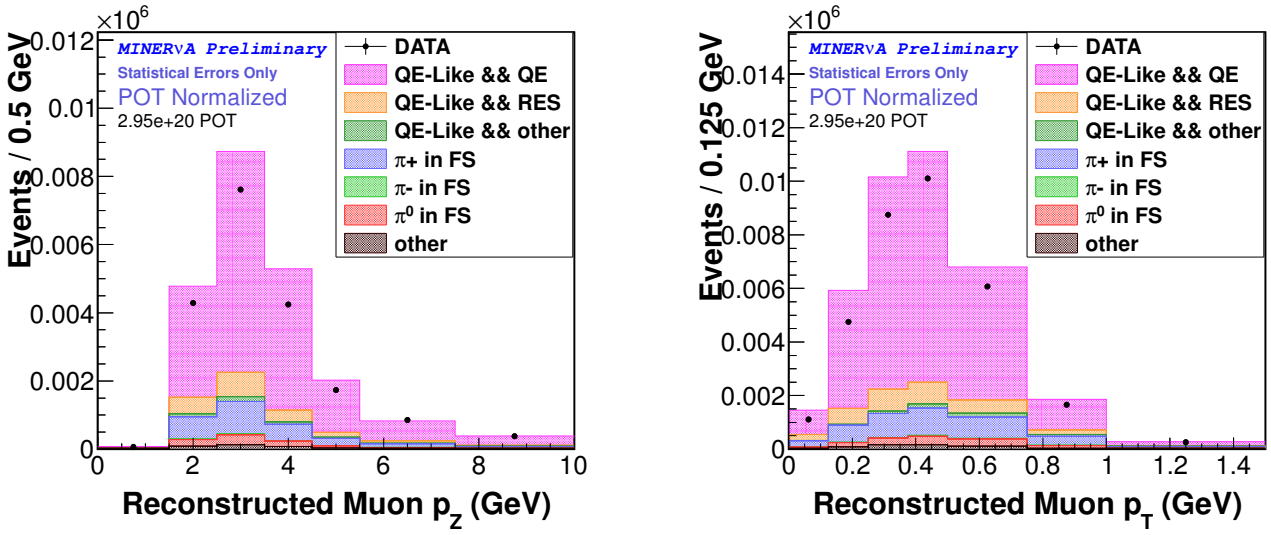

(b) Projections on P_{Z_μ} (left) and P_{T_μ} (right).

Figure 6.8: Muon $P_Z - P_T$ phase space for the $\mu^- + X$ sub-sample after all event selection criteria.

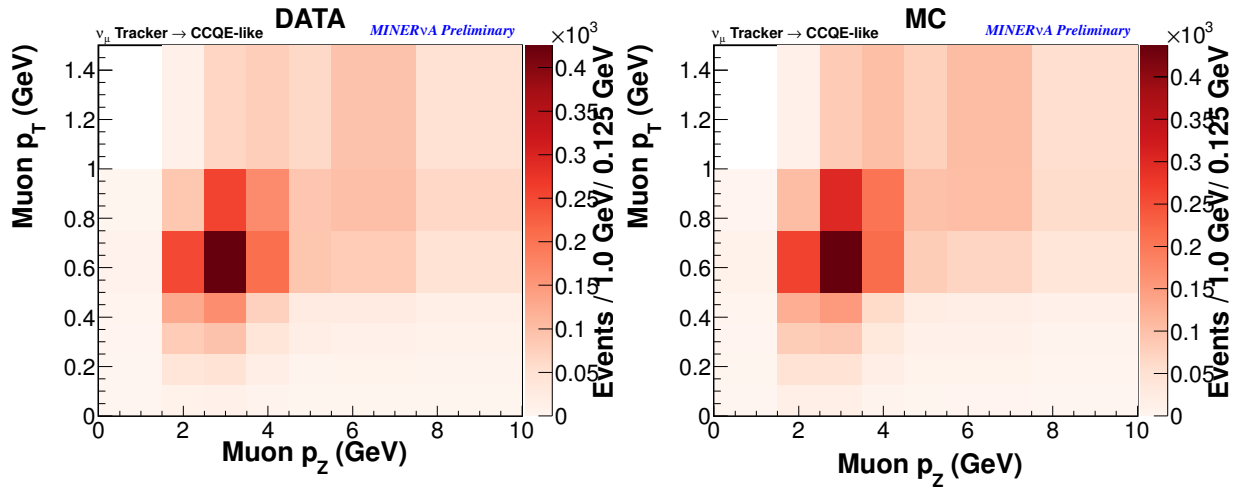

(a) DATA (left) and MC (right) 2-D distributions.

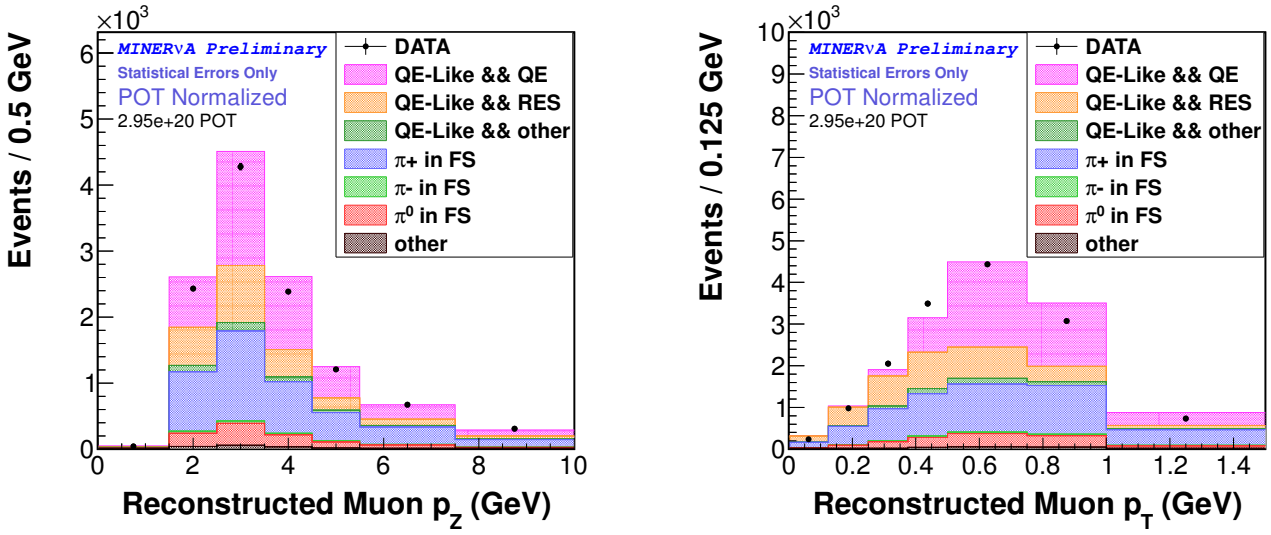

(b) Projections on P_{Z_μ} (left) and P_{T_μ} (right).

Figure 6.9: Muon $P_Z - P_T$ phase space for the $\mu^- + p + X$ sub-sample after all event selection criteria.

CHAPTER 7

The Double Differential Cross Section Measurement

7.1 Introduction

The main result of this analysis is the flux-integrated double differential cross section per nucleon for quasi-elastic like interactions on plastic scintillator in the MINERνA detector as a function of the P_{Z_μ}, P_{T_μ} observables.

The double differential cross section for this measurement in the i^{th} bin is given by:

$$\left(\frac{d^2\sigma}{dP_{Z_\mu}dP_{T_\mu}}\right)_i = \frac{\sum_j U_{ij}\left(N_j - N_j^{bg}\right)}{\epsilon_i\ T\phi\ (\Delta P_{Z_\mu})_i(\Delta P_{T_\mu})_i} \tag{7.1}$$

where:

- $\phi = \int \phi(E_\nu)dE_\nu$ is the flux integrated over acceptance $E_\nu = [1.5, 10]$GeV.
- T is the number of neutron targets in the fiducial volume studied.
- N_j is the Data.
- N_j^{bg} is the estimated background in Data.
- ΔP_{Z_μ} and ΔP_{T_μ} are the respective bin widths.
- ϵ_i is the efficiency correction.

- U_{ij} is the unfolding matrix connecting the reconstructed variable index j to the true index i.

Equation 7.1 shows that in order to measure the double differential cross section from the reconstructed events that pass our selection as described in Section 6.3 one needs a correction of the expected background rated, detector acceptance, efficiency and smearing effects due to the finite resolution of the detector and then, normalized by the corresponding flux, number of neutron targets. All of these procedures are described in the following sections.

7.2 Background Tuning and Subtraction

Figures 6.8 and 6.9 show the simulated signal and backgrounds after all event selection cuts described in Section 6.3.

The largest background is coming from charged positive pions in the final state. In order to get rid of these background events, the GENIE MC prediction is used.

The resonant pions in GENIE are simulated via the Rein-Sehgal Model as described in Sections 2.5.2.1 and 4.2.2, which is known to have big uncertainties [45]. In order to avoid a big dependence on this model, this analysis uses its own data to constrain the background prediction given by GENIE. This procedure is known as *Background Tuning*.

7.2.1 Background Tuning

In order to constrain the background predictions a template fit of background distributions in the simulation to data is performed.

The fit is performed on Recoil Energy distributions, which are divided into 2 templates: signal and background are filled for different regions of P_{T_μ} but averaged over all P_{Z_μ} in order to keep a good statistical sample for each template and data.

Due to the fact that the kinematics of events without a proton reconstructed $\mu^- + X$ (stacked Figure 6.8) and with one or more protons recontructed $\mu^- + p + X$ (stacked Figure 6.9) are different, the fits are done independently for both sub-samples and merged after subtracting the background.

For the first sub-sample ($\mu^- + X$), four bins of P_{T_μ} are used: $P_{T_\mu} < 0.25$ GeV, 0.25 GeV $\leq P_{T_\mu} < 0.50$ GeV, 0.50 GeV $\leq P_{T_\mu} < 0.75$ GeV, 0.75 GeV $\leq P_{T_\mu} < 1.50$ GeV. Figure 7.1 and 7.2 show the different Monte Carlo and DATA distributions before and after the fit for this sub-sample.

For the second sub-sample ($\mu^- + p + X$), two bins of P_{T_μ}: $P_{T_\mu} < 0.75$ GeV and 0.75 GeV $\leq P_{T_\mu} < 1.50$ GeV. Figure 7.3 and 7.4 show the different Monte Carlo and DATA distributions before the and after the fit for this sub-sample.

The fit returns the best relative normalization factors for each signal and background template. A weight for each fit is then computed in the following way:

$$\omega_i = \frac{f_i^{after\ fit}}{f_i^{before\ fit}} \tag{7.2}$$

where i is an index referring to a particular fit, ω is the weight computed, $f^{before\ fit}$ and $f^{after\ fit}$ represent the fraction of simulated background in the selected recoil sample before and after the fit respectively.

Figure 7.5 shows the corresponding weights calculated for both sub-samples.

7.2.2 Background Subtraction

Once all backgrounds are constrained by weights calculated as per Equation 7.2, the estimated background in data is given by:

$$N_{j,data}^{bg} = \omega_{fit} \frac{N_{j,sim}^{bg}}{N_{j,sim}} N_{j,data} \tag{7.3}$$

where N represents the number of events for bin j and ω_{fit} is the corresponding weight, bg stands for background and the subscript sim indicates the uncorrected simulated prediction for N. The background subtracted data for each sub-sample is:

$$N_{j,data} - N_{j,data}^{bg} = \left(1 - \omega_i \frac{N_{i,sim}^{bg}}{N_{i,sim}}\right) N_{j,data} \tag{7.4}$$

Figure 7.6 and 7.7 show the two-dimensional distributions and its corresponding projections with the predicted backgrounds for the $\mu^- + X$ and the $\mu^- + p + X$ sub-samples respectively.

Figure 7.8 and 7.9 show the two-dimensional distributions and its corresponding projections

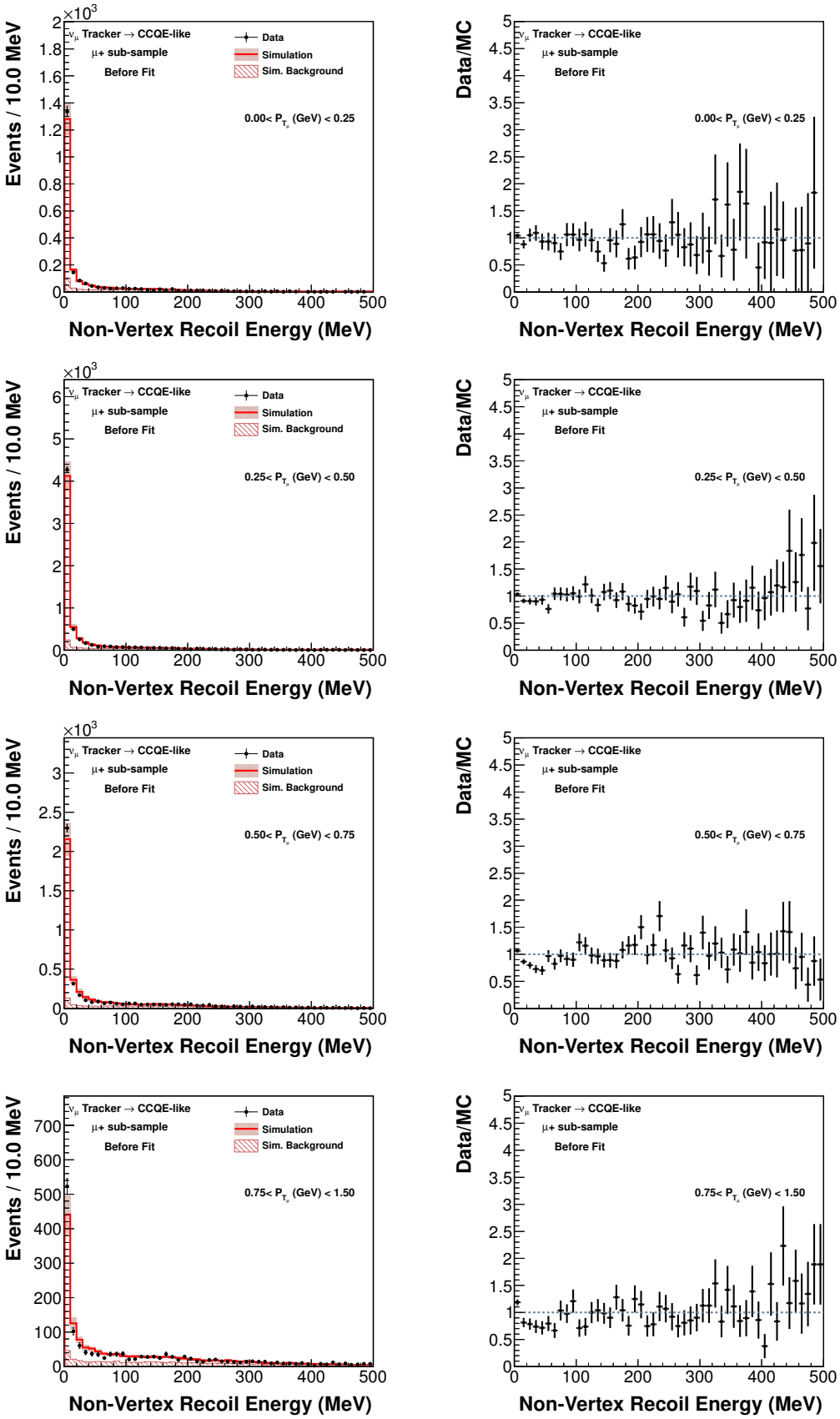

Figure 7.1: Data an Monte Carlo templates (left) and their ratios (right) for the $\mu^- + X$ sub-sample as a function of the recoil energy for different regions of P_{T_μ} before fitting.

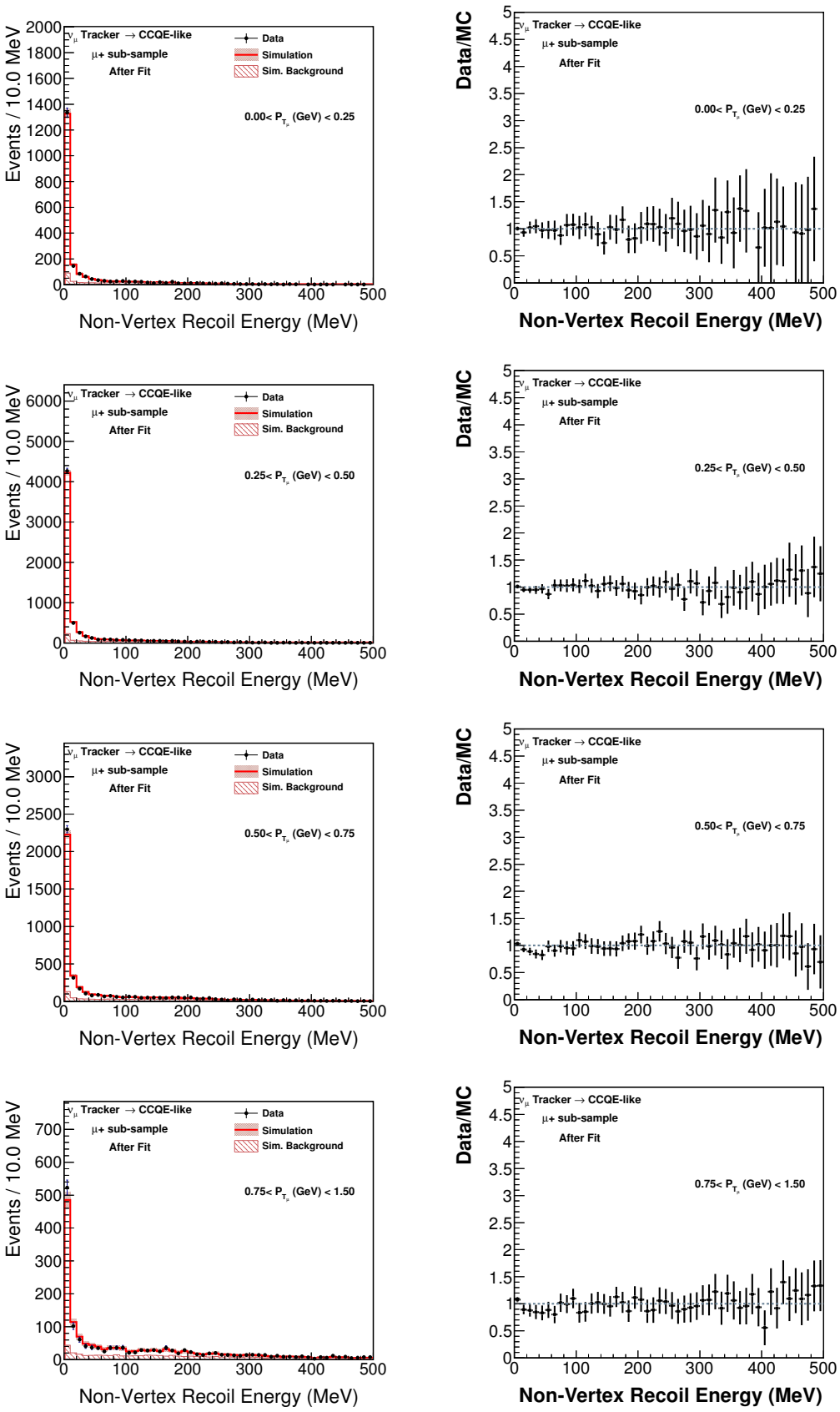

Figure 7.2: Data an Monte Carlo templates (left) and their ratios (right) for the $\mu^- + X$ sub-sample as a function of the recoil energy for different regions of P_{T_μ} after fitting.

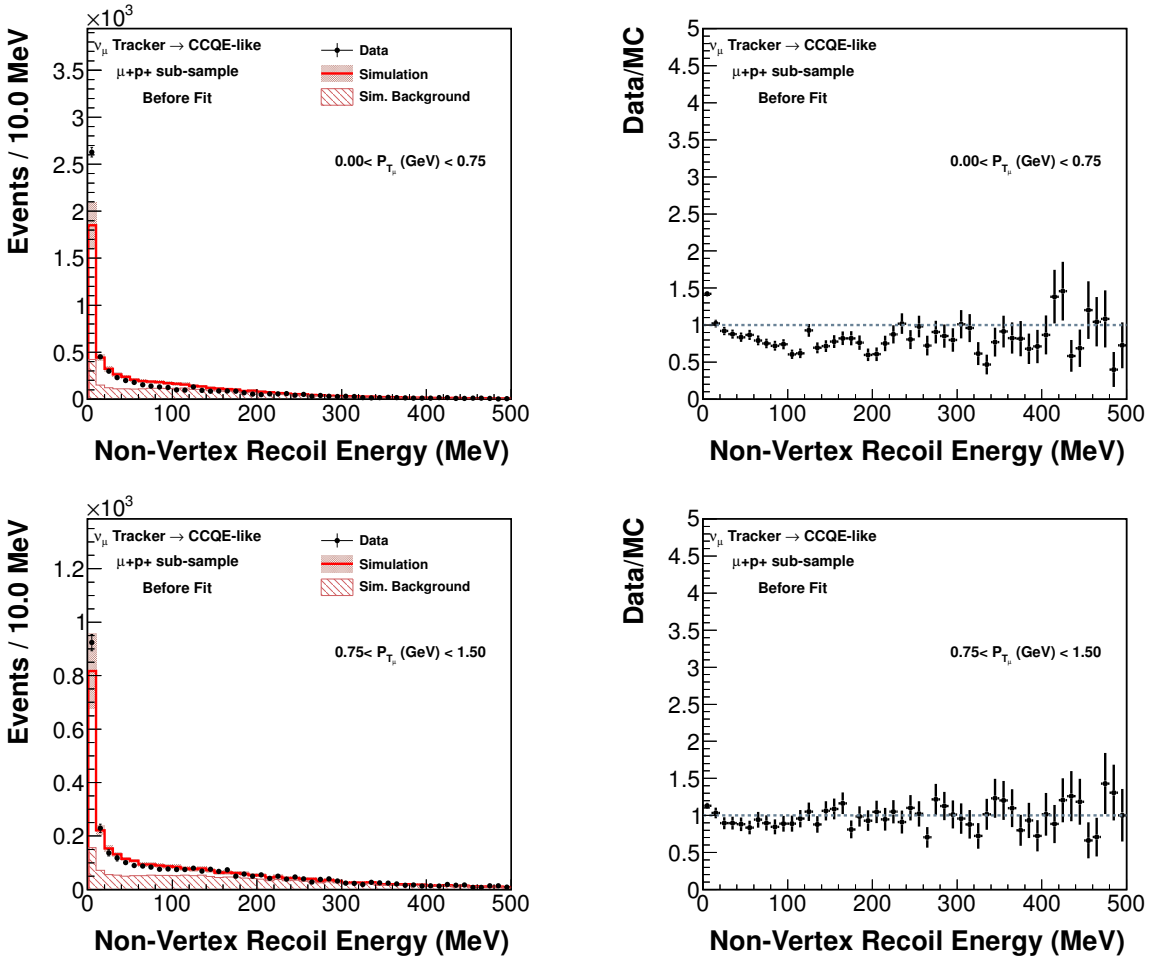

Figure 7.3: Data and Monte Carlo templates (left) and their ratios (right) for the $\mu^- + p + X$ sub-sample as a function of the recoil energy for different regions of P_{T_μ} before fitting.

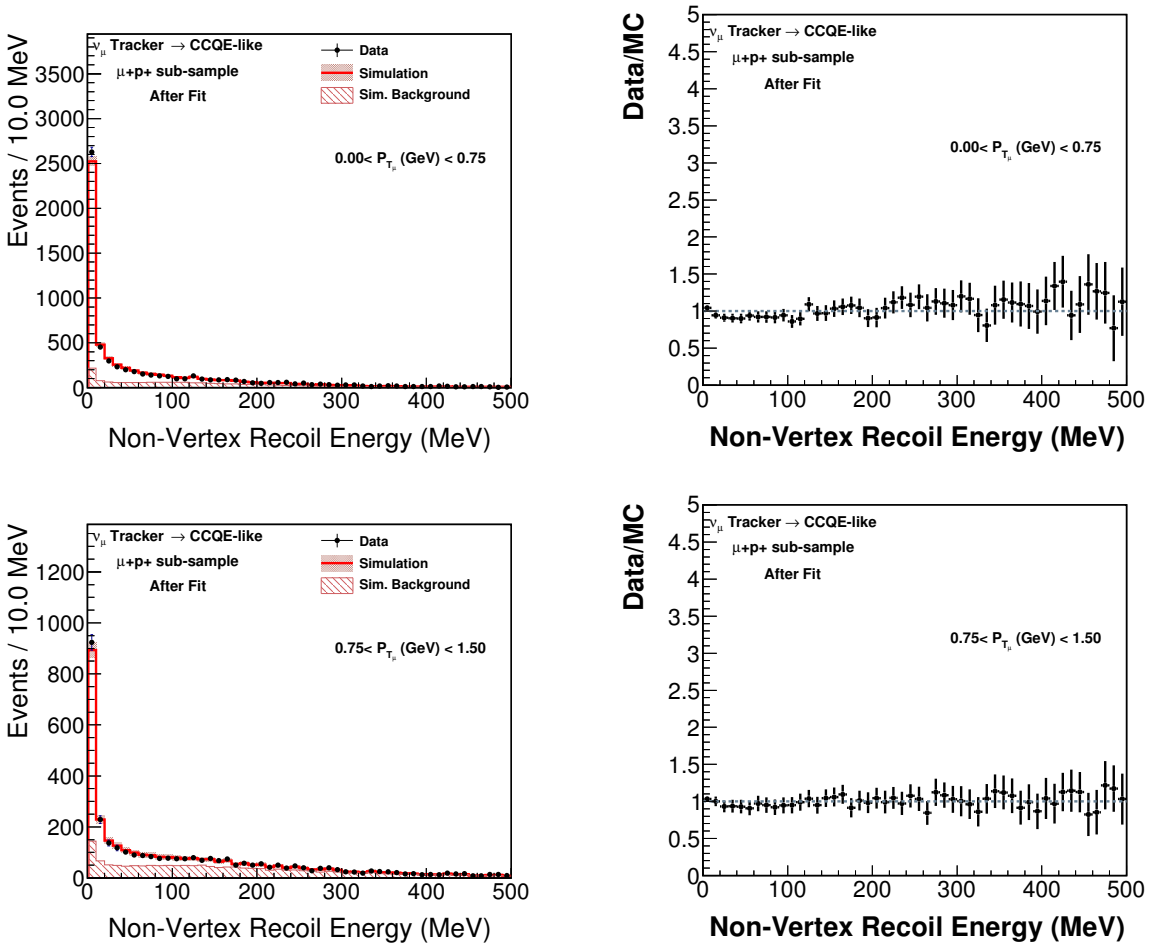

Figure 7.4: Data an Monte Carlo templates (left) and their ratios (right) for the $\mu^- + p + X$ sub-sample as a function of the recoil energy for different regions of P_{T_μ} after fitting.

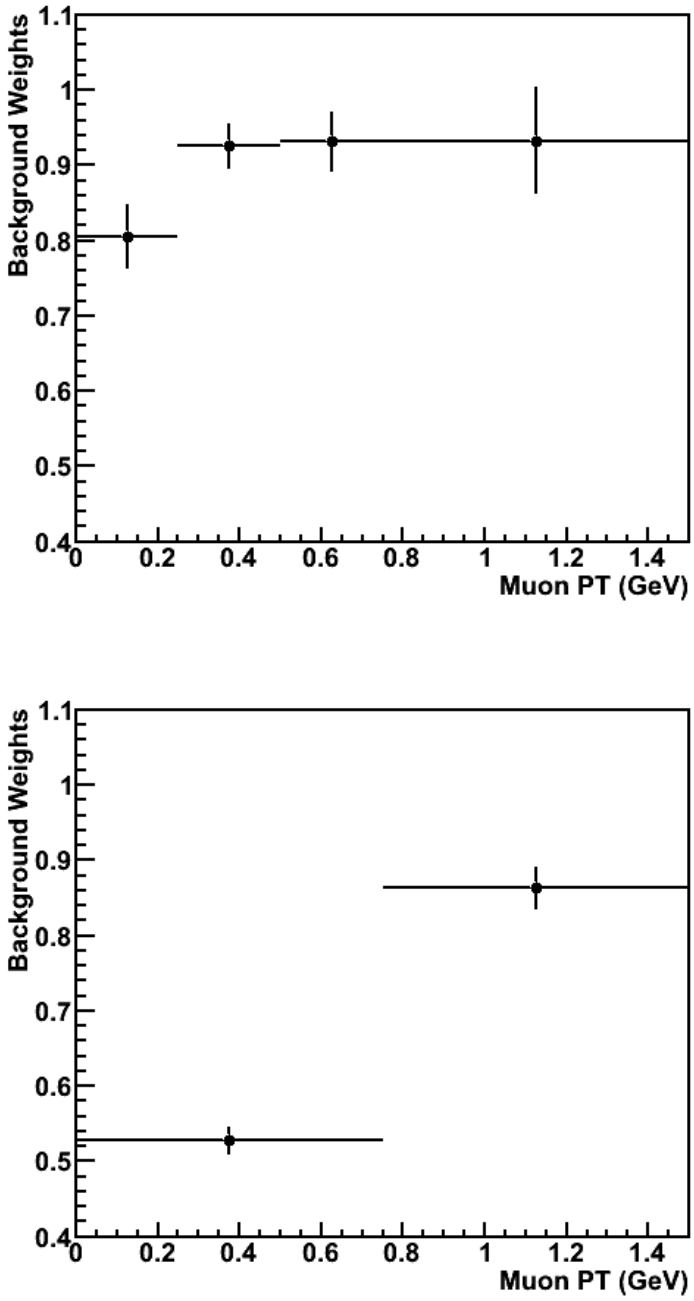

Figure 7.5: Background Weights for both sub-samples as a function of P_{T_μ}.

after background subtraction for the $\mu^- + X$ and the $\mu^- + p + X$ sub-samples respectively.

Figure 7.10 shows the two-dimensional background subtracted distribution and projections after merging $\mu^- + X$ and $\mu^- + p + X$ sub-samples.

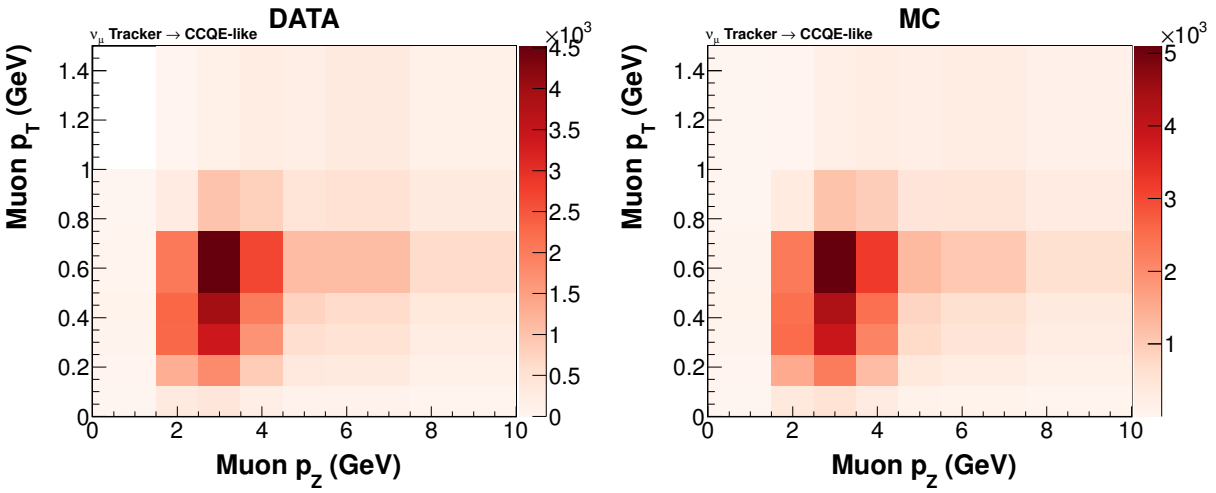

(a) DATA (left) and MC (right) 2-D distributions

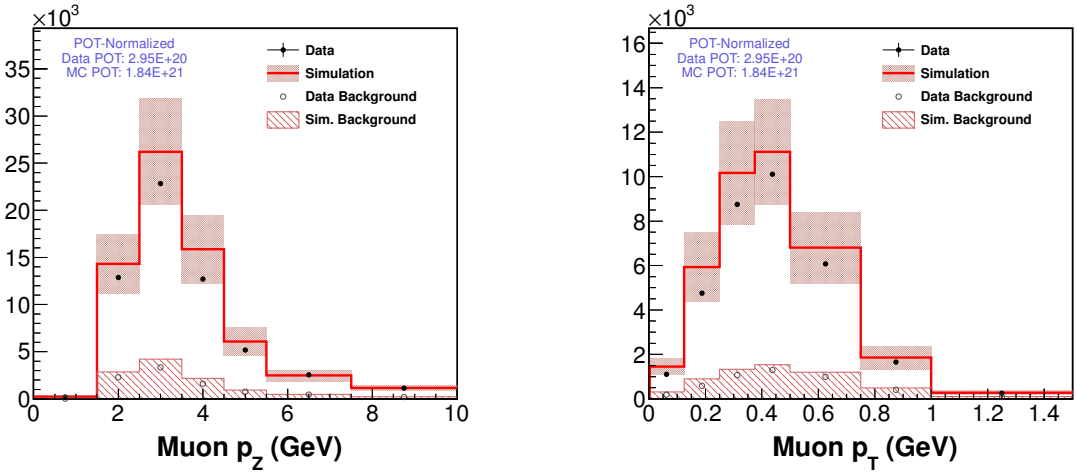

(b) Projections on P_{Z_μ} (left) and P_{T_μ} (right)

Figure 7.6: Muon $P_Z - P_T$ phase space for the $\mu^- + X$ sub-sample with predicted backgrounds.

7.3 Unfolding

In any experiment, measured quantities are smeared out due to limited measurement accuracy(finite resolution) of the detector, implying only a statistical relation between the true kinematic variable and the measured quantity. The procedure to correct for these fluctuations is called *unfolding*.

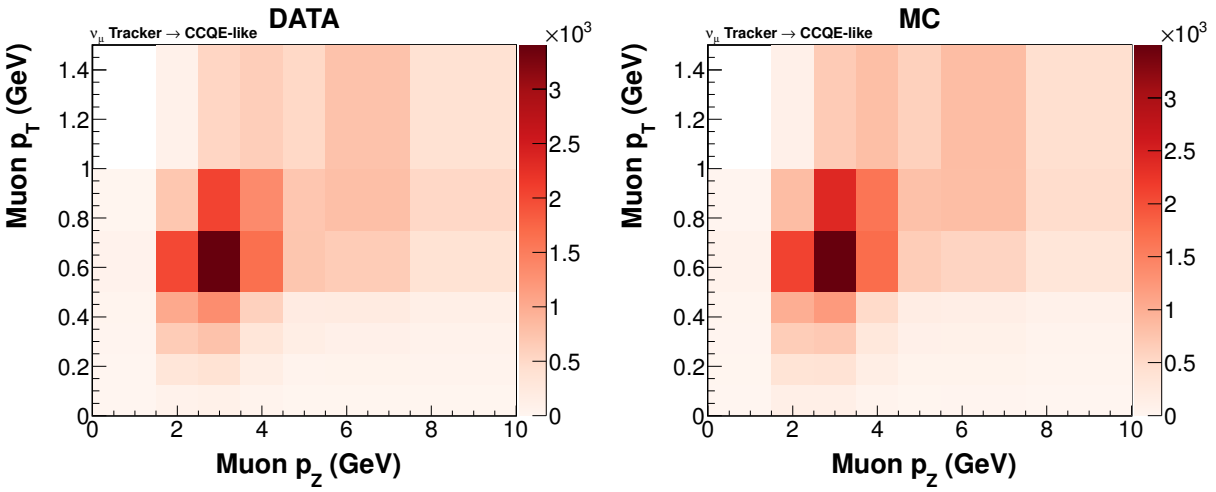

(a) DATA (left) and MC (right) 2-D distributions

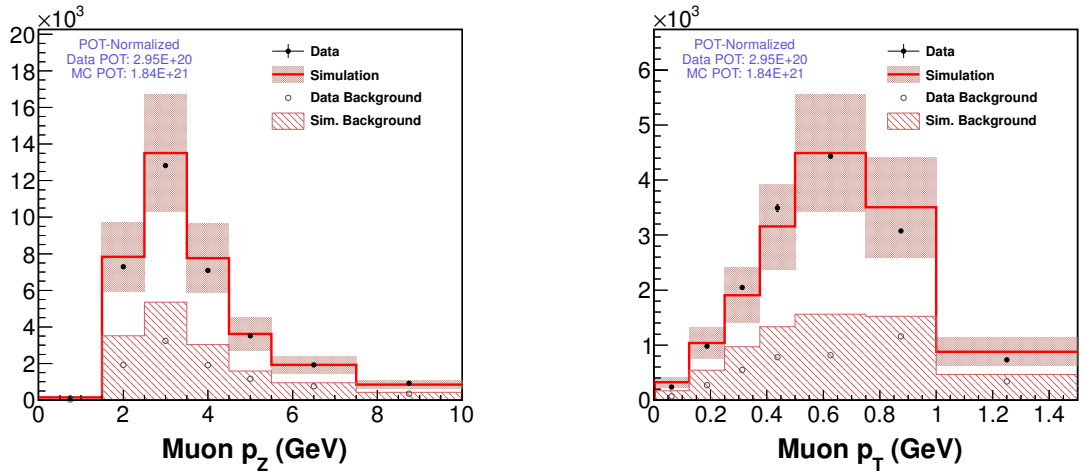

(b) Projections on P_{Z_μ} (left) and P_{T_μ} (right)

Figure 7.7: Muon $P_Z - P_T$ phase space for the $\mu^- + p + X$ sub-sample with predicted backgrounds.

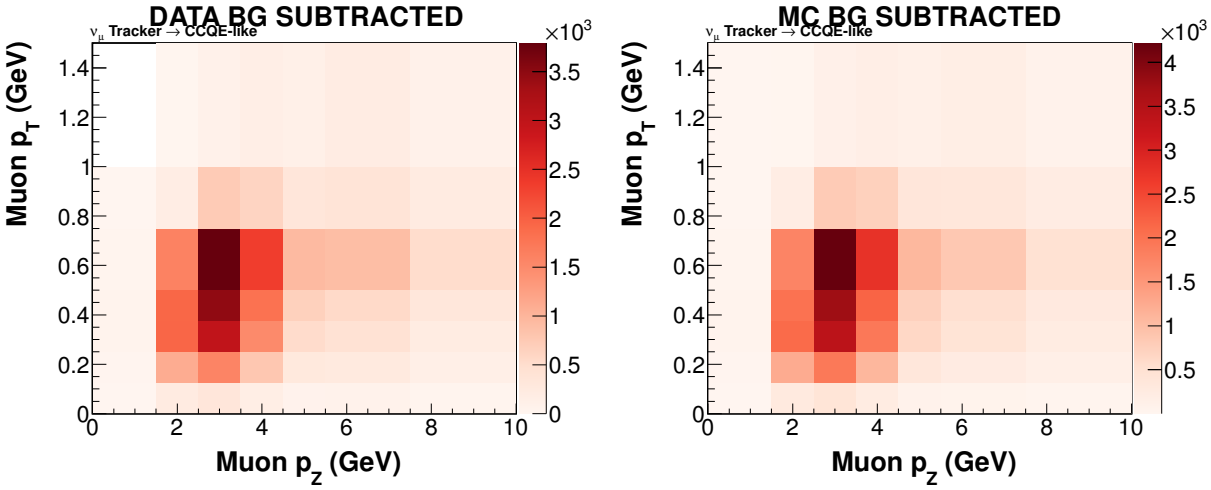

(a) DATA (left) and MC (right) 2-D distributions

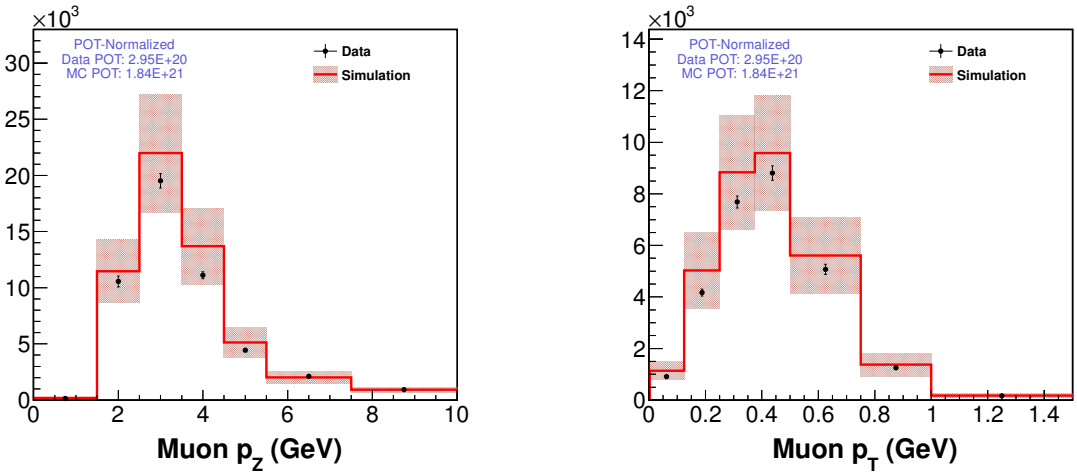

(b) Projections on P_{Z_μ} (left) and P_{T_μ} (right)

Figure 7.8: Muon $P_Z - P_T$ phase space for the $\mu^- + X$ sub-sample after background subtraction.

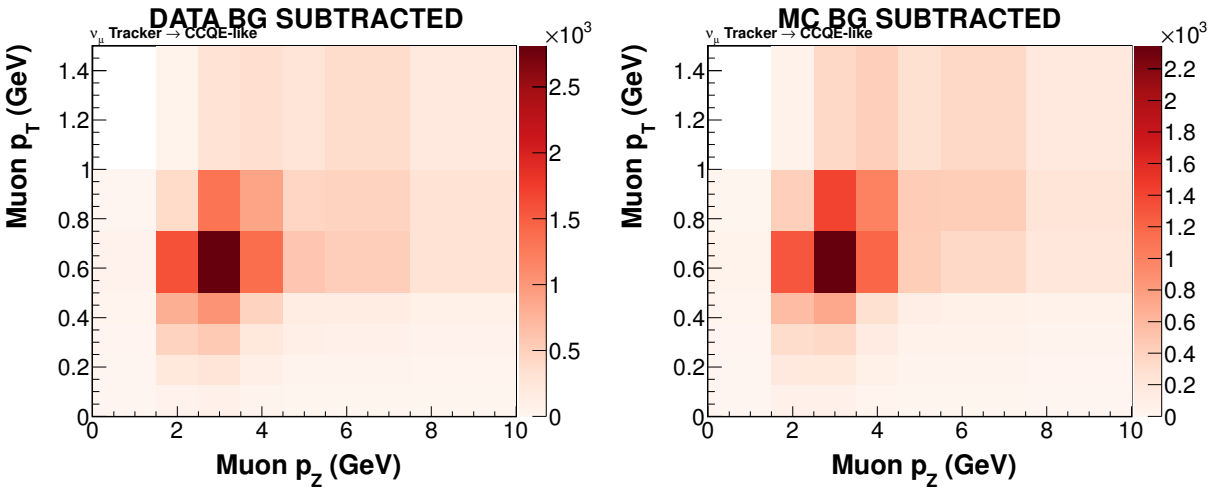

(a) DATA (left) and MC (right) 2-D distributions

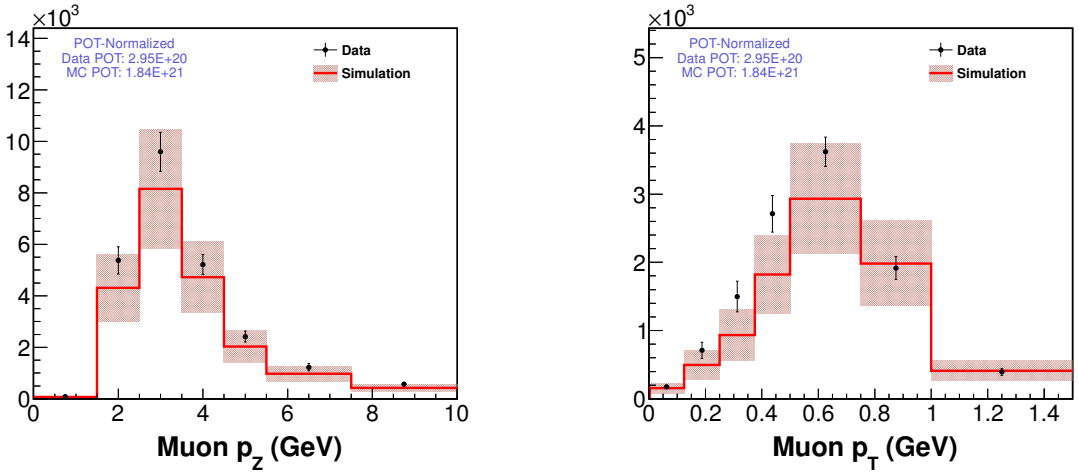

(b) Projections on P_{Z_μ} (left) and P_{T_μ} (right)

Figure 7.9: Muon $P_Z - P_T$ phase space for the $\mu^- + p + X$ sub-sample after background subtraction.

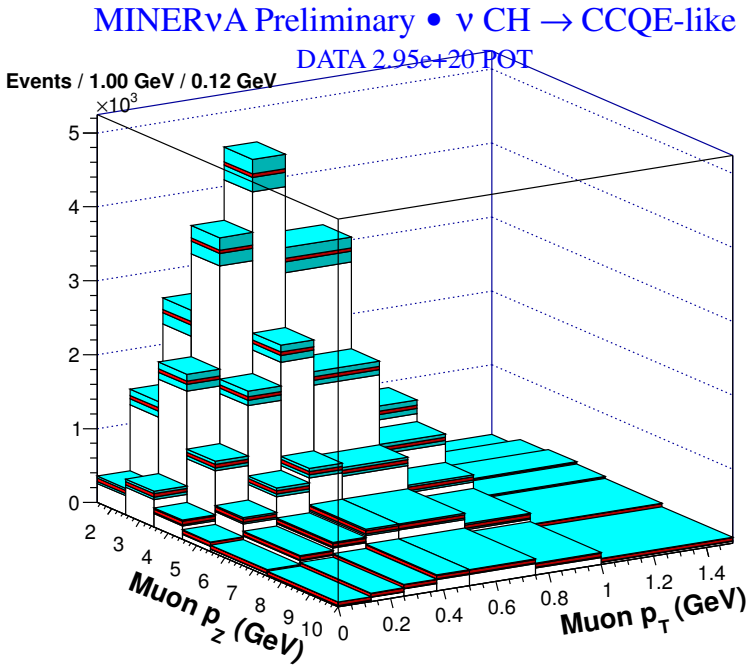

(a) DATA background subtracted distribution

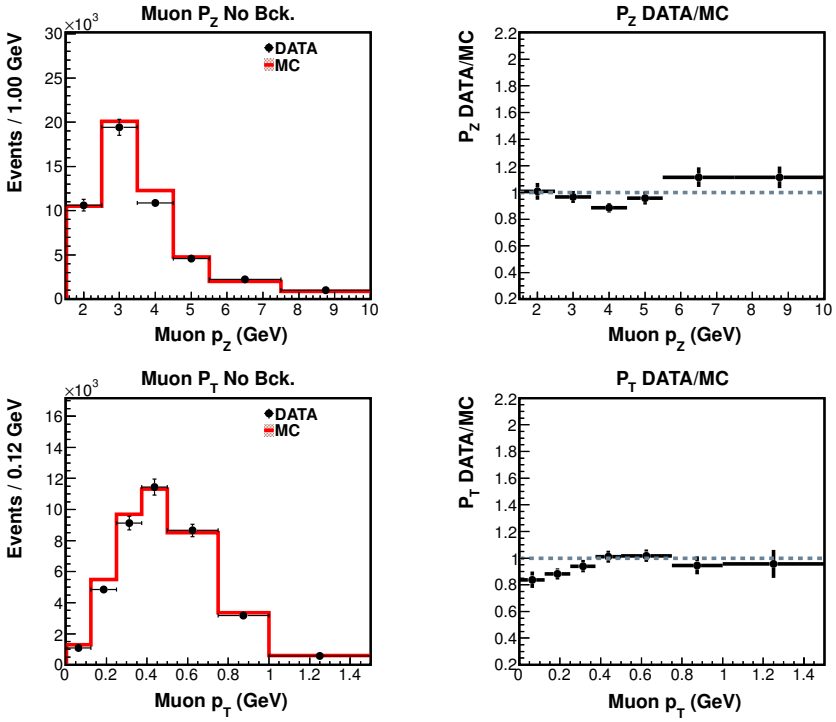

(b) Projections on P_{Z_μ} (left) and P_{T_μ} (right) with DATA/MC overlay

Figure 7.10: Muon $P_Z - P_T$ phase space after background subtraction and merging $\mu^- + X$ and $\mu^- + p + X$ sub-samples.

7.3.1 The Smearing Matrix

The migration or smearing matrix shows the probability of a measured quantity x to happen given its true value y. The measured quantities follow the relation:

$$x_i = \sum_j A_{ij} y_j \tag{7.5}$$

Where A is the smearing matrix, j is the bin in the true kinematics and i s the bin in the reconstructed kinematics.

For the $P_Z - P_T$ phase space, the true values of P_Z in bins of true P_T are presented in the Y axis, while the reconstructed values of P_Z in bins of reconstructed P_T are shown in the X axis.

Figure 7.11 shows the smearing matrix used for the unfolding in this $P_Z - P_T$ phase space (the colors represent the fraction of true events in each reconstructed bin). Each black-dot rectangular region represents the smearing of P_Z for a specific P_T region. This means each true P_Z bin can smear horizontally in the matrix to the different reconstructed P_Z bins in the different reconstructed P_T bins. This can be represented by the following expression:

$$P_{Z_i}^{True}(P_{T_j}^{True}) \rightarrow P_{Z_k}^{Reco}(P_{T_m}^{reco} \epsilon P_{T_j}^{True}) \tag{7.6}$$

where $1 \leq i, k \leq N_{P_Z}$ and $1 \leq j, m \leq N_{P_T}$.

Figure 7.12 shows the smearing of the true P_Z bins that belong to two different reconstructed P_T regions.

7.3.2 Simple Inversion Matrix

If we invert the matrix in equation 7.5, we can get the truth estimates, as shown in equation 7.7. This is the simplest way to unfold or unsmear a measured quantity.

$$y_i = \sum_j A_{ij}^{-1} x_j \tag{7.7}$$

However, if the off-diagonal elements of the smearing matrix are too large (i.e if bins size are too small compared to the measurement's resolution), this method is not so accurate and gives large variances which is why more effective methods, like the bayesian technique are usually used instead.

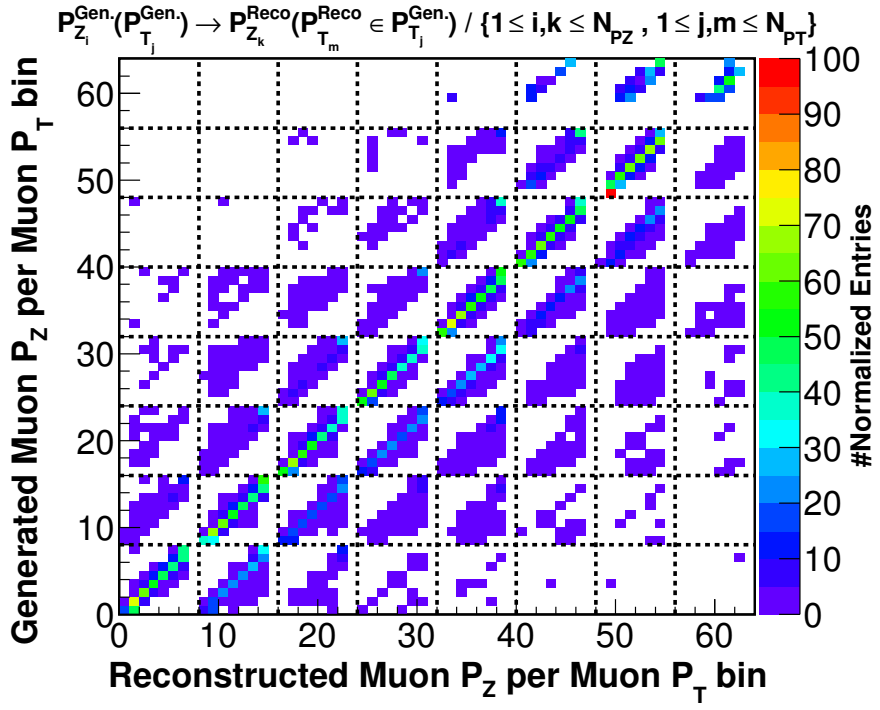

Figure 7.11: Smearing Matrix for the Muon $P_Z - P_T$ phase space for Signal (QE-Like) Events.

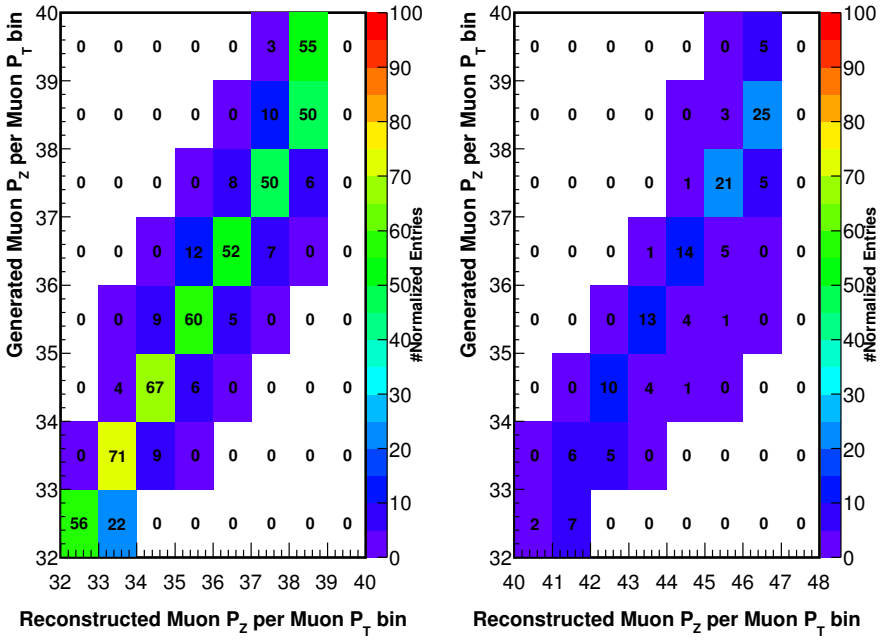

Figure 7.12: Zoom on Smearing Matrix: This is showing smearing of the true P_Z bins into the reconstructed P_Z bins in the reconstructed P_T region from: 0.6GeV $\leq P_T <$ 0.8GeV (left) and 0.8GeV $\leq P_T <$ 1.4GeV (right).

7.3.3 The Bayesian Technique

This analysis uses the method described by D'Agostini in [99]. It uses the bayes' theorem repeatedly to invert the smearing matrix. The regularization parameter in this algorithm is the number of iterations.

The Unfolded distribution $\hat{n}(C_i)$ as the result of applying the unfolding matrix M_{ij} to the measurements $n(E_j)$ is:

$$\hat{n}(C_i) = \Sigma_{j=1}^{n_E} M_{ij} n(E_j)$$

where:

- $\hat{n}(C_i)$: Unfolded Distribution
- M_{ij}: Unfolding Matrix
- $n(E_j)$: Folded Distribution

The Bayesian method is used for calculating the unfolding matrix:

$$M_{ij} = \frac{P(E_j|C_i) n_0(C_i)}{\epsilon_i f_j} \tag{7.8}$$

where:

- $P(E_j|C_i)$ is the Smearing Matrix
- ϵ_i are the efficiencies
- f_j is the folded prior distribution
- $n_0(C_i)$ is arbitrary, then updated from previous $\hat{n}(C_i)$ iteration.

In this procedure, the efficiencies ϵ_i in equation 7.8 are simply 1 for this analysis, because these are corrected independently after the unfolding (see Section 7.4).

Figure 7.13 shows the unfolded Data and MC with its corresponding projections.

7.4 Efficiency and Acceptance Correction

The efficiency and acceptance correction is related to the detector acceptance and the tracking efficiency.

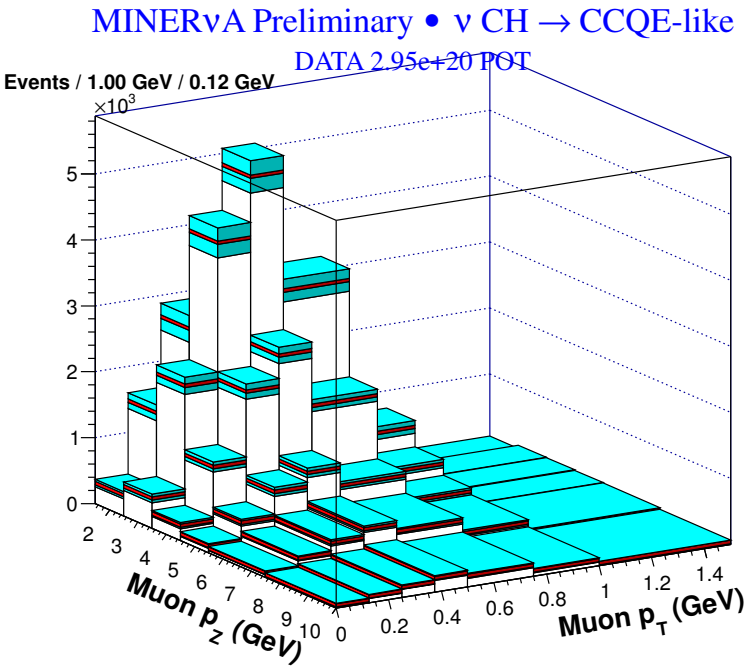

(a) DATA background subtracted and unfolded distribution

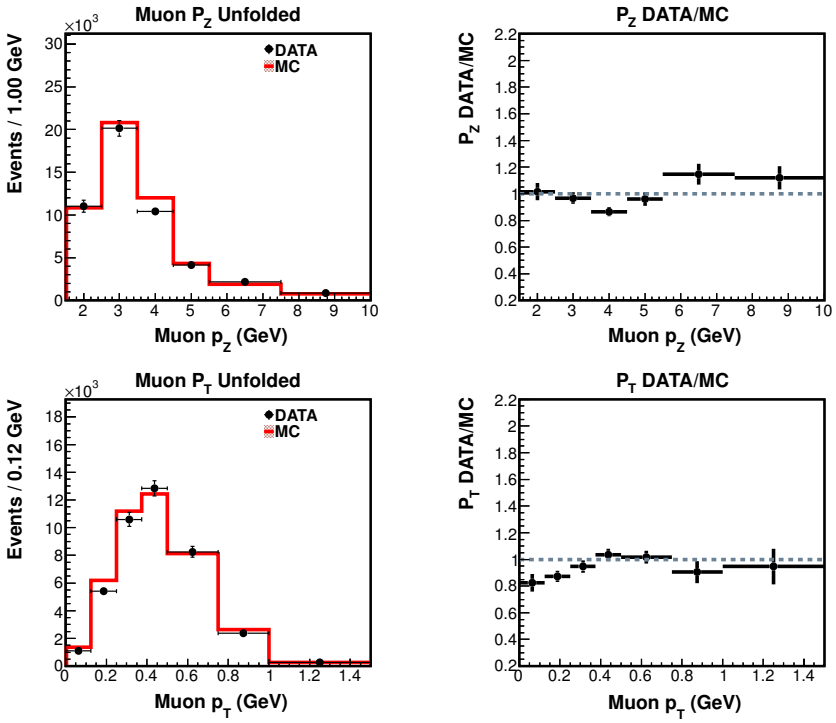

(b) Projections on P_{Z_μ} (left) and P_{T_μ} (right) with DATA/MC overlay

Figure 7.13: Muon $P_Z - P_T$ phase space after unfolding.

As mentioned in Section 5.3, this analysis relies on the MINOS near detector to determine the charge and momentum of muons, which means the acceptance of muons covered by this technique have up to 20 degrees scattering angle with respect to the Z-axis. This and the reconstruction inefficiencies on the muon and the proton PID, are the main reasons why not all of the observed ν_μ CCQE-Like events enter into the final event selection.

The muon tracking efficiency has been measured in MINERνA and MINOS separately [100]. This accounts for the efficiency of muons that propagate from MINERνA to MINOS but do not incorporate geometric acceptance effects. Table 7.1 summarizes these corrections with uncertainties included.

Source of Efficiency Correction	Correction
MINERvA tracking	0.973 ± 0.002
MINOS tracking ($p_\mu^{MINOS} < 3$GeV/c)	0.934 ± 0.002
MINOS tracking ($p_\mu^{MINOS} > 3$GeV/c)	0.982 ± 0.001

Table 7.1: Corrections to the muon reconstruction efficiency in MINERvA and MINOS.

The simulation is used to estimate the geometric acceptance as following:

$$\epsilon_i = \left(\frac{N_{gen}^{passed\ selection}}{N_{gen,fid}^{1.5 \leq E_\nu \leq 10}} \right)_i \tag{7.9}$$

where ϵ_i is the correction factor for a specific bin i, $N_{gen}^{passed\ selection}$ is the number of signal events generated in the fiducial volume for bin i and $N_{gen,fid}^{1.5 \leq E_\nu \leq 10}$ is the number of generated events in the fiducial volume and with a neutrino energy from 1.5 to 10 GeV for bin i.

Figure 7.14 shows the efficiency correction histogram calculated using Equation 7.9, and Figure 7.15 has the efficiency corrected distributions and its corresponding projections with DATA/MC overlay.

7.5 Flux and Target Normalization

The final steps in order to get the cross section, is to normalize by:

- the flux integrated over acceptance $E_\nu = [1.5, 10]$GeV
- the number of neutron targets
- the respective ΔP_{T_μ} and ΔP_{Z_μ} bin widths

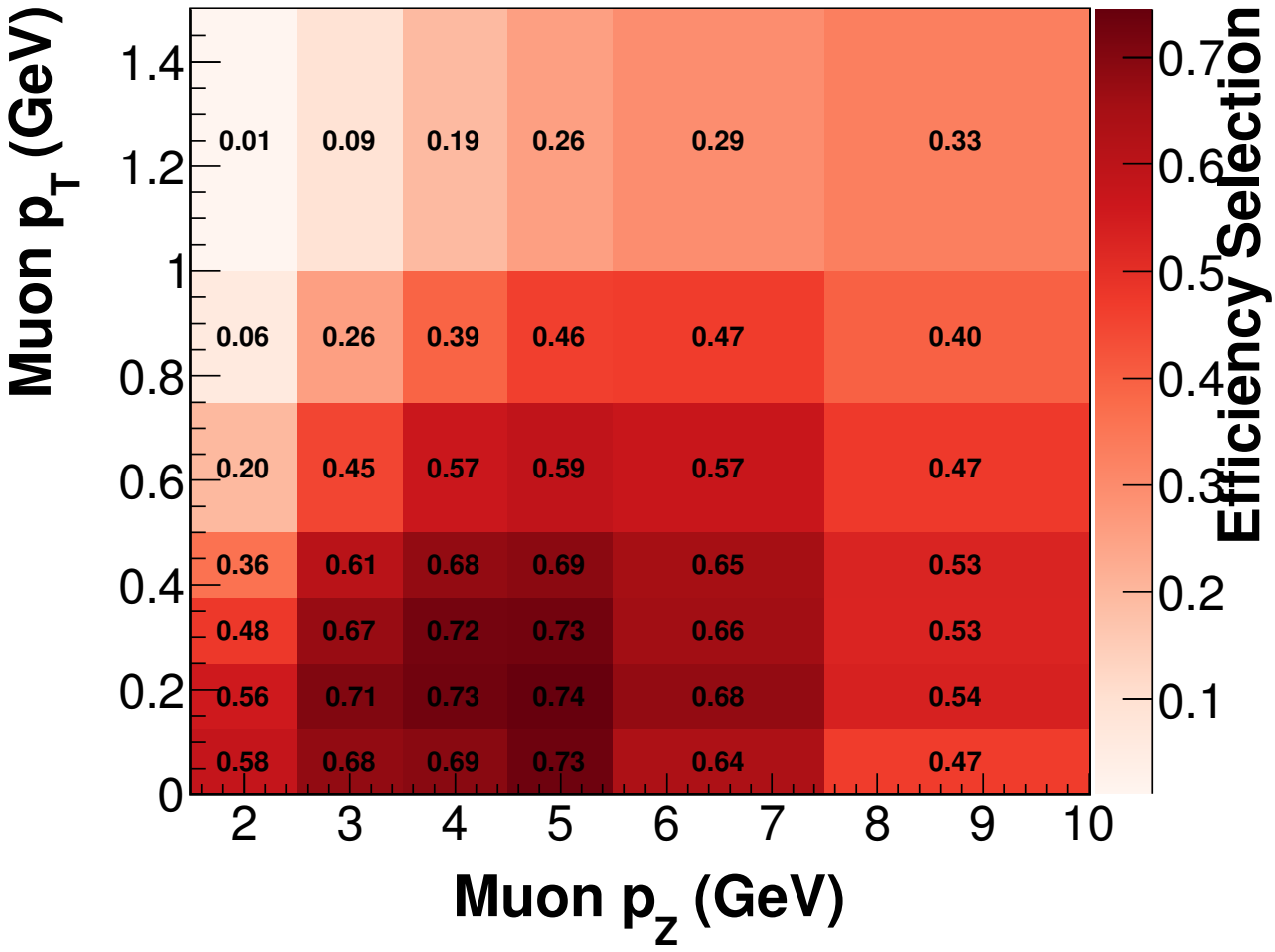

Figure 7.14: Efficiency Correction Histogram for the Muon $P_Z - P_T$ phase space for Signal (QE-Like) Events.

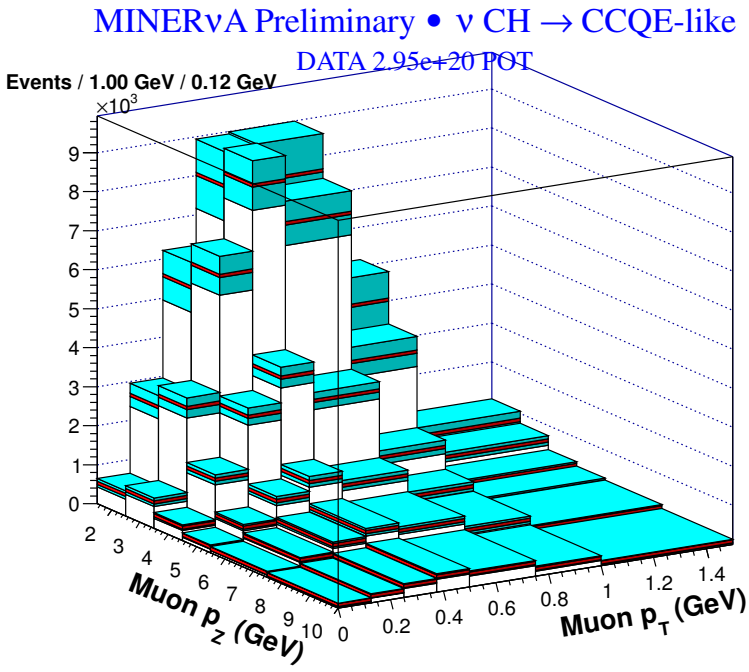

(a) DATA background subtracted, unfolded and efficiency corrected distribution

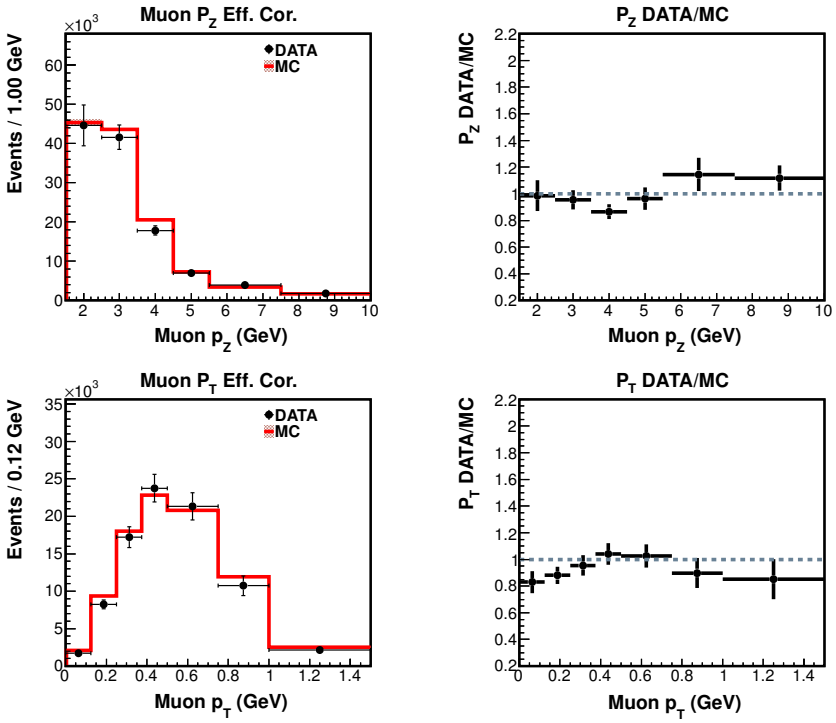

(b) Projections on P_{Z_μ} (left) and P_{T_μ} (right) with DATA/MC overlay

Figure 7.15: Muon $P_Z - P_T$ phase space after efficiency correction.

The flux is calculated as described in Section 4.1 and shown in Figure 7.16, and the integrated flux is $\phi = 2.91 \times 10^{-8}/\text{cm}^2$ per proton on target. The number of neutron targets within the fiducial volume is given by $T = 1.516 \times 10^{30}$.

Figure 7.17 shows the Data double differential cross section result and its corresponding projections with MC overlay.

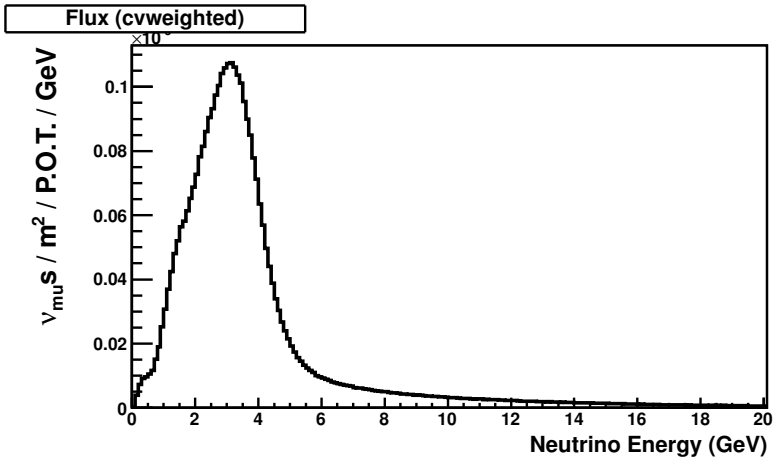

Figure 7.16: Neutrino Energy Flux in GeV.

Double Diff. Cross Section in Muon P_Z, P_T (GeV) bins ($\times 10^{-40}\text{cm}^2/\text{GeV}^2/\text{neutron}$)							
$P_Z \downarrow \backslash P_T \rightarrow$	0.000 - 0.125	0.125 - 0.250	0.250 - 0.375	0.375 - 0.500	0.500 - 0.750	0.750 - 1.000	1.000 - 1.500
1.50 - 2.50	3.04±0.22(0.43)	15.91±0.52(2.00)	33.77±0.83(4.56)	48.77±1.16(6.53)	48.74±1.15(6.80)	26.89±1.48(4.40)	4.82±0.80(0.88)
2.50 - 3.50	3.81±0.23(0.48)	17.71±0.50(1.96)	37.50±0.73(4.18)	50.78±0.90(5.59)	44.04±0.73(4.87)	20.73±0.70(2.59)	3.52±0.27(0.50)
3.50 - 4.50	1.76±0.15(0.20)	8.40±0.33(0.84)	17.43±0.46(1.79)	22.72±0.53(2.32)	18.23±0.39(1.87)	7.75±0.31(0.99)	1.60±0.12(0.27)
4.50 - 5.50	0.62±0.09(0.07)	2.87±0.18(0.29)	6.17±0.26(0.66)	8.32±0.30(0.87)	6.90±0.22(0.78)	3.51±0.18(0.52)	0.99±0.09(0.21)
5.50 - 7.50	0.40±0.05(0.05)	1.62±0.10(0.17)	3.12±0.13(0.35)	4.32±0.15(0.49)	3.72±0.12(0.45)	2.10±0.09(0.38)	0.77±0.06(0.17)
7.50 - 10.00	0.21±0.04(0.02)	0.80±0.06(0.09)	1.50±0.08(0.16)	2.18±0.10(0.23)	1.80±0.07(0.21)	0.92±0.05(0.14)	0.25±0.02(0.04)

Table 7.2: Double differential cross section $d^2\sigma/dP_{Z_\mu}dPT_\mu$ content values ± statistical (systematic) errors.

7.6 Systematic Errors

The cross section measurement is sensitive to different parameters in the simulation models and the reconstruction. The uncertainties on each of these parameters lead to a systematic error for the cross section.

The systematic errors are evaluated using the "Many Universes" method [101]. Given a certain uncertainty on a model or reconstruction parameter, the nominal value of such parameter

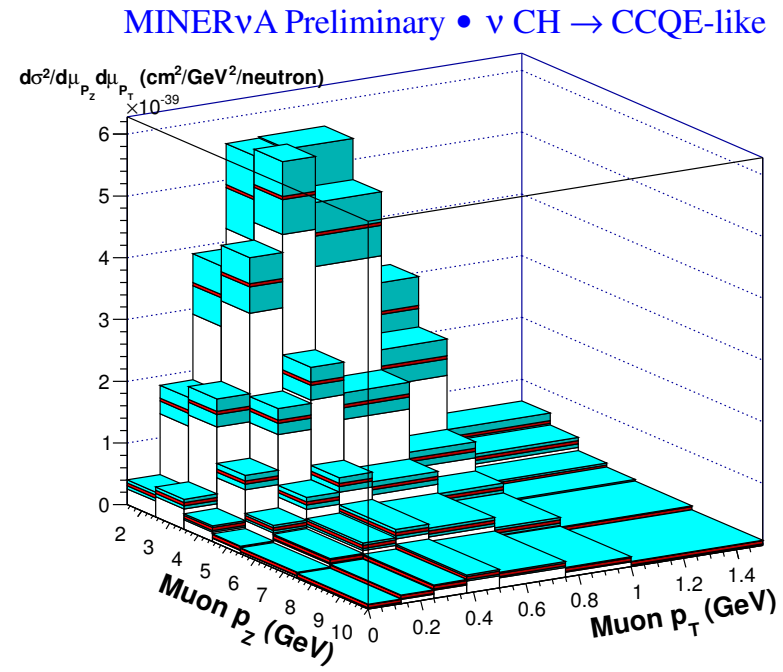

(a) DATA Double differential Cross Section.

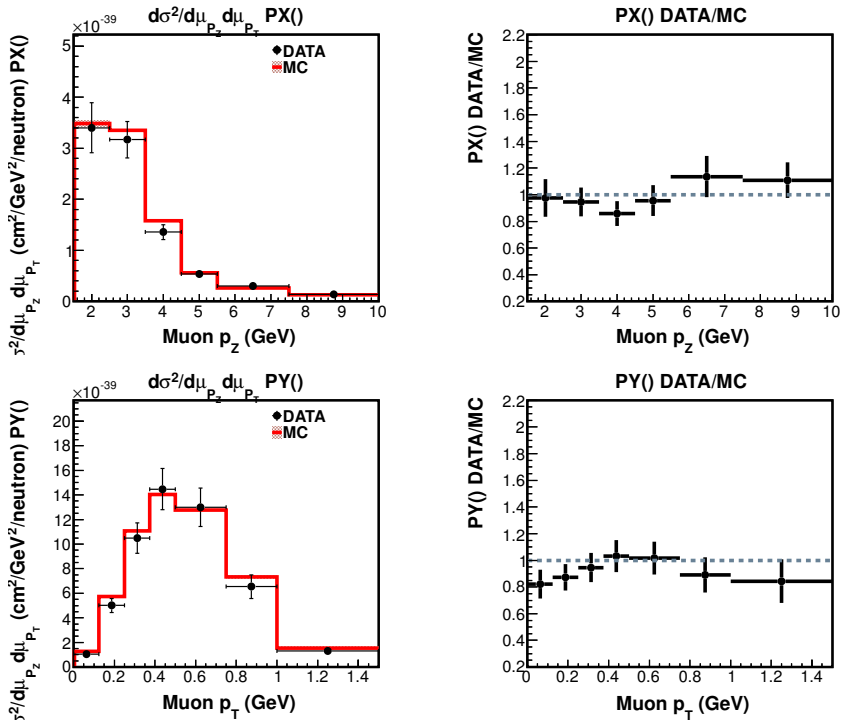

(b) Projections on P_{Z_μ} (left) and P_{T_μ} (right) with DATA/MC overlay.

Figure 7.17: Muon $P_Z - P_T$ Double differential Cross Section $\frac{d^2\sigma}{dP_{Z_\mu} dP_{T_\mu}}$.

is shifted by this uncertainty and the whole cross section is re-calculated in this new scenario. This new scenario is defined in the experiment as a "universe", and each universe cross section can be expressed as:

$$\left(\frac{d^2\sigma}{dP_{Z_\mu}dP_{T_\mu}}\right)_{i,universe} = \frac{\sum_j U_{ij}\left(N_{j,universe} - N^{bg}_{j,universe}\right)}{\epsilon_{i,universe}\ T\phi_{universe}\ (\Delta P_{T_\mu})_{i,universe}(\Delta P_{Z_\mu})_{i,universe}} \tag{7.10}$$

The equation 7.10 is the same equation as in 7.1, with the only difference that each of the components in the latest expression with the subscript *universe* can be impacted by these uncertainties.

There are different universes for each parameter shifted. If they are shifted once or twice, the $\pm 1\sigma$ uncertainties are used, otherwise 100 different shifts are selected from a Gaussian distribution with a mean equal to 0 and a width equal to σ.

Also, each universe has to pass the event selection criteria described in Section 6.3 in order to take into account the effect of such a shift in the selection itself.

For each error a covariance matrix is calculated using the information from these universes:

$$cov_{i,j} = \frac{1}{N}\sum_{k=1}^{N}(x_{ki} - \bar{x_i})(x_{kj} - \bar{x_j}) \tag{7.11}$$

where, *i,j* label the bins, k is the universe index, $\bar{x}$ represents the mean value of a particular bin.

The systematic uncertainty for a specific bin, is the square root of the covariance matrix

$$\sigma_i = \sqrt{cov(i,i)} \tag{7.12}$$

The shape component of that systematic uncertainty can be obtained by normalizing each universe to the area of the central value before calculating the covariance matrix.

The total systematic error is obtained from the square root of the sum of all covariance matrices, as expressed in Equation 7.13

$$\sigma_i^{total} = \sqrt{\sum_{j=1}^{N} cov_j(i,i)} \tag{7.13}$$

Where j is the index for the systematic error components, N is the total number of systematic errors, i is the bin in the distribution.

Figure 7.18 shows the systematic and statistical fractional errors projected on the P_T and P_Z axis. This shows that the biggest systematic error comes from the flux (about 9%). This is why future progress in the flux constrain methods described in Section 4.1 is so important for MINERνA .

Appendix C.1 has a summary of the fractional errors after each of the intermediate steps described in this section: background subtraction, unfolding, efficiency correction.

Appendix C.2 has a summary of the fractional errors for each error group component shown in Figure 7.18 and described from Section 7.6.1 to 7.6.5.

Table 7.2 has the numerical content for the double differential cross section in Muon P_Z, P_T (GeV) bins and its statistical (systematic) errors.

7.6.1 Flux

The flux errors come from uncertainties in the cross section hadron productions models, the focusing of these hadrons to the beamline, and the data constraint techniques described in Section 4.1. These uncertainties are divided in three categories:

Flux NA49

This is the uncertainty due to the hadron production constraint on the flux simulationof the NA49 Data (see Section 4.1.1). This uncertainty is equal to the experimental errors of the NA49 measurement and the uncertainties of scaling the NA49 data from 158 GeV/c to the proton beam energy (120 GeV/c) that is known to be negligible [102].

Flux Tertiary

The hadron production from the NuMI target for particles that are not constrained by data are taken into account in this uncertainty. Three different models are used to simulate this component: Geant4's implementation of QGSP_BERT [103], FTFP_BERT [104] and Fluka [82], as shown in Figure 7.19. The uncertainty is the maximum spread among these models.

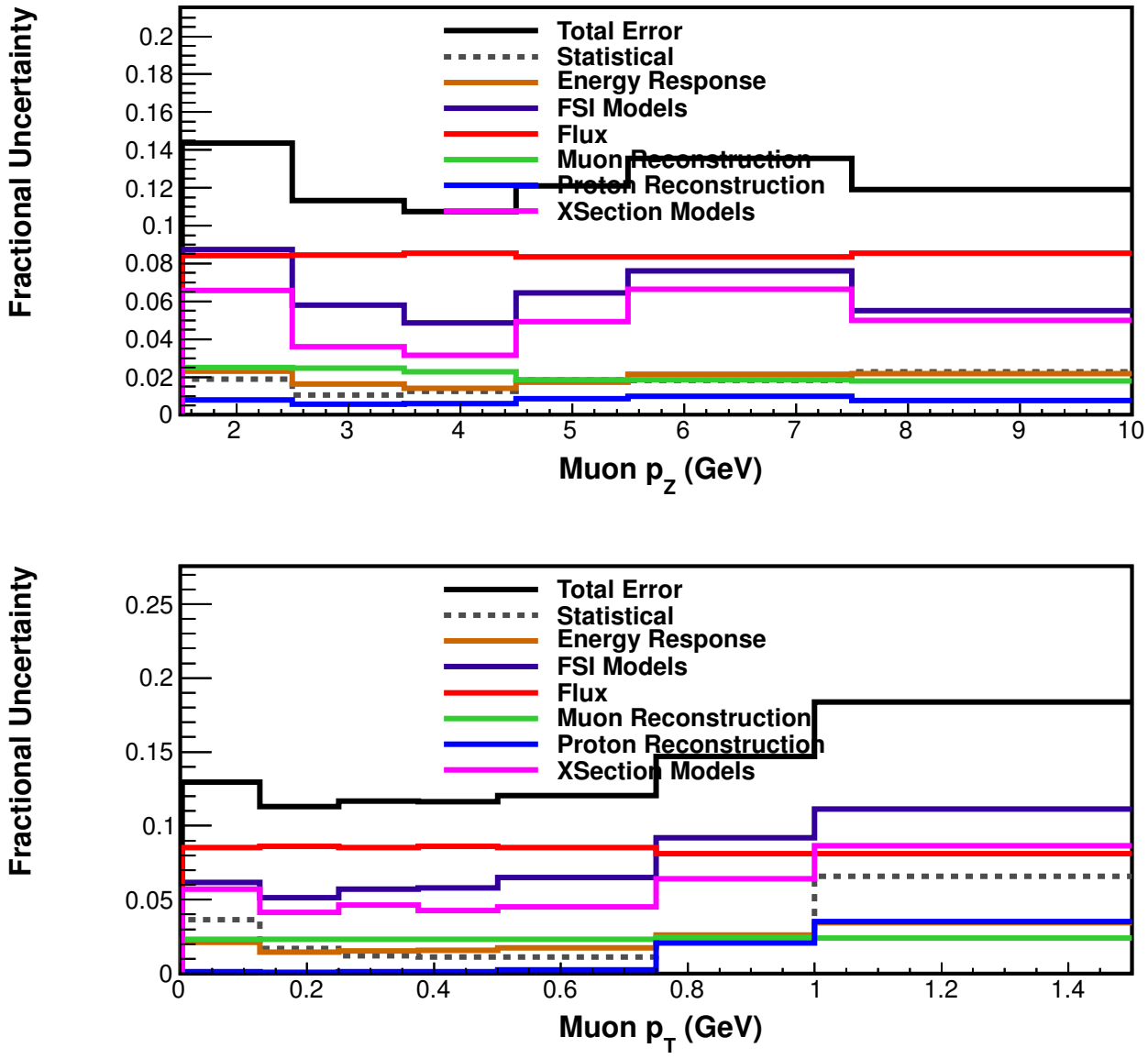

Figure 7.18: Error summary in Data for Muon P_T and P_Z cross section projections.

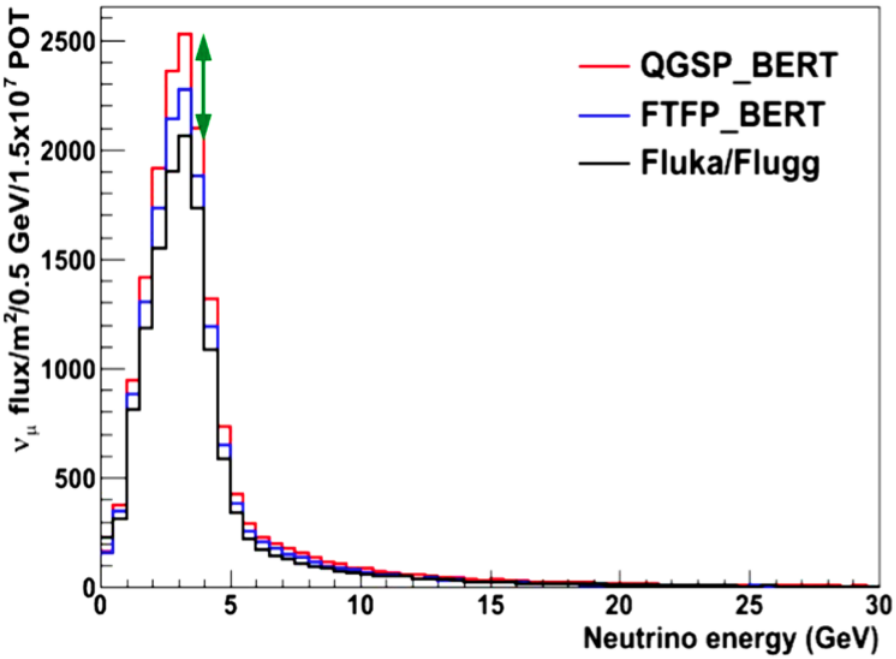

Figure 7.19: NuMI neutrino flux prediction using three different hadronic models. The green arrow represents the maximum spread between the peaks of these models. Plot by M.Kordosky from the MINERνA Collaboration.

Flux Beam Focus

These are the uncertainties associated with the proton beam and focusing system of the NuMI beamline such as the alignment and the magnetic field model in the horns. These have been measured by MINOS [105].

7.6.2 Cross Section and FSI Models

The cross section is sensitive to GENIE models because we rely on it for background subtraction, detector unfolding and efficiency correction. These uncertainties are measured using the GENIE reweighting infraestructure, which is used to vary several model parameters by $\pm 1\sigma$.

The parameters related to quasi-elastic models do not affect the calculation of efficiencies. All other parameters impact the background prediction.

Final state interactions affect the measurement because the recoil hadronic energy is used to enhance the signal region as described in Section 6.3.11. This is why the probability of final state particles to interact with the target is important. These probabilities are estimated with GENIE via Intranuke (see Section 4.3.2) and the uncertainties are measured with the GENIE reweighting infraestructure.

See Appendix D for a description of the main model parameters used for these uncertainties.

7.6.3 Muon Reconstruction

Uncertainties on the muon energy and scattering angle are taken into account. The muon angle uncertainty is 2 mrad. The Muon energy scale uncertainty is composed of three effects:

- **MINOS range measurement:** the error on reconstruction of the muon momentum by range is 2% [106]. This is due to the uncertainty in the detector mass, uncertainty in the dE/dx model and reconstruction's implementation of the geometry.
- **MINOS curvature measurement:** the uncertainty associated with the muon reconstructed by curvature as described in Section 5.3 is 2.5% for muons with momentum lower than 1 GeV/c and 0.6% for muons withmomentum above 1 GeV/c.
- **Energy loss in MINERνA :** an additional error due to uncertainties in the material assay and dE/dx model are also taken into account. The dE/dx model uncertainty is 30 MeV and the material assay uncertainty is 11 MeV.

7.6.4 Energy Response

As described in Section 6.3.11, the recoil energy is used as a function of Q^2 to enhance the quasi-elastic-like signal. This cut is sensitive to the observed scintillation light produced by the particles. Monte Carlo is used to identify each particle associated with the the recoil energy, and then its energy is varied according to the values in Table 7.3. See reference [107] for more details on these uncertainties.

Particle	Uncertainty
proton	3.5%
neutron ($E_{kin} < 50$MeV)	25%
neutron ($E_{kin} < 150$MeV)	10%
neutron ($E_{kin} > 150$MeV)	20%
muon	2.4%
$\gamma, \pi^0, e^{\pm}$	3%
$\pi^{\pm}, K$	5%
optical x-talk	20%
other	20%

Table 7.3: Detector Energy Response Uncertainties.

7.6.5 Proton Reconstruction

The dE/dx is used in order to identify proton (see Section 6.3.6) as part of one of the event selection criteria. Due to this fact, the analysis is sensitive to the proton particle reconstructed

momentum used for the particle identification. This is affected by Bethe Block calculation, detector mass model, absolute energy scale constant (MEU) and Birk's law.

7.6.5.1 Bethe-Block calculation

The Bethe-block equation [108] is used to calculate the average energy loss per material:

$$-\frac{dE}{dx} = Kz^2\frac{Z}{A}\frac{1}{\beta^2}\left(\frac{1}{2}ln\frac{2m_ec^2\beta^2\gamma^2T_max}{I^2} - \beta^2 - \frac{\delta(\beta\gamma)}{2}\right) \tag{7.14}$$

where the parameters are described in reference [108]. An uncertainty of 1% (3%) for a given pure(compound) material is applied based on several studies [109].

7.6.5.2 Absolute Energy Scale Constant (MEU)

The absolute energy scale calibration affects the dE/dX measurement. An uncertainty of 2.4% is applied to account for this.

7.6.5.3 Detector Mass Model

The energy reconstruction is sensitive to the path of the material that the particle trajectory traverses. The path dx of the material is scaled up and down on the thickness of the materials in the detector according to the values in Table 7.4.

Material	Uncertainty
Plastic Scintillator	1.4%
Iron	0.5%
Lead	1.3%

Table 7.4: Mass thickness uncertainty per material in the tracker fiducial region.

7.6.5.4 Birk's Law Quenching Parameter

Birk's empirical law is scaled by $(1 + k_B dE/dx)$ [110], where K_B is measured in the test beam detector to be 0.0905±0.012 mm/MeV. The value used in the simulation is $K_B = 0.133$mm/MeV [111], so the difference has to be taken into account in the form of a systematic. In order to do this, the energy of each hit on the hadron track candidate is adjusted to be consistent with the measured value of K_B and the modified energy loss profile is used by the dE/dx particle identification. For a shift δ in K_B, the uncertainty on the energy E_{hit} is given as [110]:

$$\Delta E_{hit} = -\frac{E_{hit}^2}{x_{hit}}\delta \tag{7.15}$$

where x_{hit} and E_{hit} are the path length and energy deposited by the Monte Carlo hit for a given particle and $\delta = -0.0545\text{m/GeV}$.

7.6.5.5 Other Systematics

There are other sources that contribute to the total systematic uncertainty:

- **Detector mass scale:** a flat correction of $\delta = \pm 1.4\%$ is taken into account for the detector mass scale.
- **Minerva and Minos Muon Reconstruction Efficiency:** the uncertainties in table 7.1 are considered.

CHAPTER 8

Final Results

The final double differential cross section $\frac{d^2\sigma}{dP_{Z_\mu} dP_{T_\mu}}$ and its respective projection on P_Z and P_T are shown in Figure 8.1. The red bars represent the central value and the surrounding lighter bands the statistical + systematic errors summed in quadrature. The numerical values are provided in Table 8.1.

The result presented is a measurement for neutrino energies between 1.5 and 10 GeV. The muon longitudinal momentum goes from 1.5 to 10 GeV. The 0-1.5 GeV region is ommited because those muons do not have enough momentum to travel through the MINOS Near Detector, which is one of the requirements in this analysis (See Section 6.3.2).

The transverse momentum goes from 0 to 1.5 GeV. Figure 2.7 shows neutrino energies from 0 to 10 GeV and four-momentum transfers from 0 to 2 GeV^2 (computed under the quasi-elastic assumption and from the muon kinematics as shown in Equations 2.60 and 2.61) are covered in this phase space. These are the neutrino energy limits and the kinematical region used in the first single differential cross sections $\frac{d\sigma}{dQ^2}$ published by MINERνA [64].

Details on the systematic errors are included in Section 7.6 and Appendix C.1.

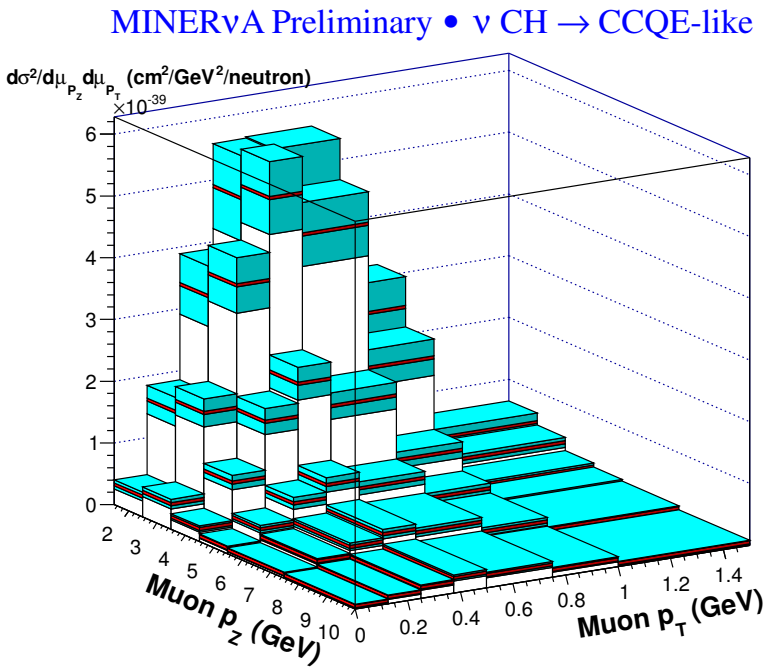

(a) DATA Double differential Cross Section

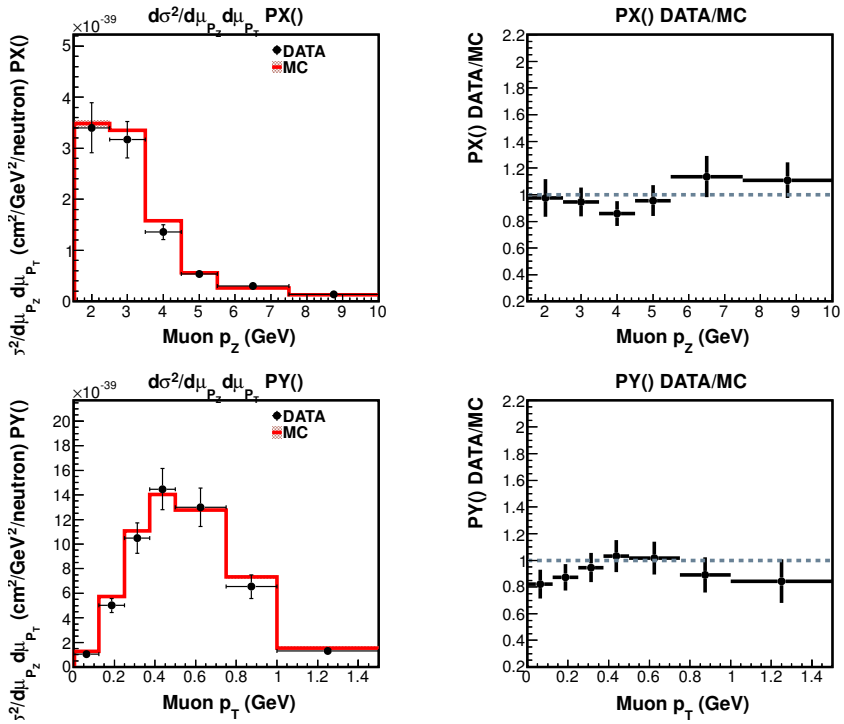

(b) Projections on P_{Z_μ} (left) and P_{T_μ} (right) with DATA/MC overlay

Figure 8.1: Muon $P_Z - P_T$ Double differential Cross Section $\frac{d^2\sigma}{dP_{Z_\mu} dP_{T_\mu}}$

Double Diff. Cross Section in Muon P_Z, P_T (GeV) bins ($\times 10^{-40}$cm^2/GeV^2/*neutron*)							
$P_Z \downarrow \backslash P_T \rightarrow$	0.000 - 0.125	0.125 - 0.250	0.250 - 0.375	0.375 - 0.500	0.500 - 0.750	0.750 - 1.000	1.000 - 1.500
1.50 - 2.50	3.04±0.22(0.43)	15.91±0.52(2.00)	33.77±0.83(4.56)	48.77±1.16(6.53)	48.74±1.15(6.80)	26.89±1.48(4.40)	4.82±0.80(0.88)
2.50 - 3.50	3.81±0.23(0.48)	17.71±0.50(1.96)	37.50±0.73(4.18)	50.78±0.90(5.59)	44.04±0.73(4.87)	20.73±0.70(2.59)	3.52±0.27(0.50)
3.50 - 4.50	1.76±0.15(0.20)	8.40±0.33(0.84)	17.43±0.46(1.79)	22.72±0.53(2.32)	18.23±0.39(1.87)	7.75±0.31(0.99)	1.60±0.12(0.27)
4.50 - 5.50	0.62±0.09(0.07)	2.87±0.18(0.29)	6.17±0.26(0.66)	8.32±0.30(0.87)	6.90±0.22(0.78)	3.51±0.18(0.52)	0.99±0.09(0.21)
5.50 - 7.50	0.40±0.05(0.05)	1.62±0.10(0.17)	3.12±0.13(0.35)	4.32±0.15(0.49)	3.72±0.12(0.45)	2.10±0.09(0.38)	0.77±0.06(0.17)
7.50 - 10.00	0.21±0.04(0.02)	0.80±0.06(0.09)	1.50±0.08(0.16)	2.18±0.10(0.23)	1.80±0.07(0.21)	0.92±0.05(0.14)	0.25±0.02(0.04)

Table 8.1: Double differential cross section $d^2\sigma/dP_{Z_\mu}dPT_\mu$ content values ± statistical(systematic) errors.

CHAPTER 9

Conclusions

This dissertation presents the first measurement of a double (flux-averaged) differential cross section, $d^2\sigma/dP_{Z_\mu}dP_{T_\mu}$ for muon neutrino charged-current quasi-elastic like interactions on a hydrocarbon (CH) at neutrino energies between 1.5 and 10 GeV.

The average neutrino energy provided by the NuMI beam facility is ∼3.5 GeV, and the data used by this analysis has been expanded with respect to the first publication [64] to use the whole neutrino data available by MINERνA in the low energy configuration that was taken between March 2010 and April 2012 (Section 6.1.2).

Although this is an analysis in terms of muon observables, the proton is also reconstructed and identified, and michel electrons are tagged and rejected from the event selection in order to improve the purity of the sample, which is estimated to be 74% (Section 6.3).

The study of this cross section in the form of a double differential cross section in terms of observable quantities (See Figure 7.17 and Table 7.2) makes this a minimally model dependent measurement.

In other words, the results in this dissertation are the most detailed quasi-elastic like cross section measurements in terms of muon observables in the MINERνA experiment so far, which makes it specially useful to be used for modern nuclear model comparisons and global fits, important for future neutrino oscillation experiments.

In the near future, models implemented in other modern event generators (i.e NuWro [112]) can be used to analyze which ones are most favored by the the cross section data presented in this phase space ($P_{Z_\mu} - P_{T_\mu}$).

APPENDIX A

Proton Range Score Cut

This apendix shows the proton range score for different ranges of Q^2 that was used to select the cuts shown in table 6.1.

For each Q^2 region the cut was chosen to keep about 80% of the proton events. For Q^2 from 0.8 to 2 GeV^2, there are many protons event at low proton range score values and the gain in purity is too low, so no cut was applied in that region.

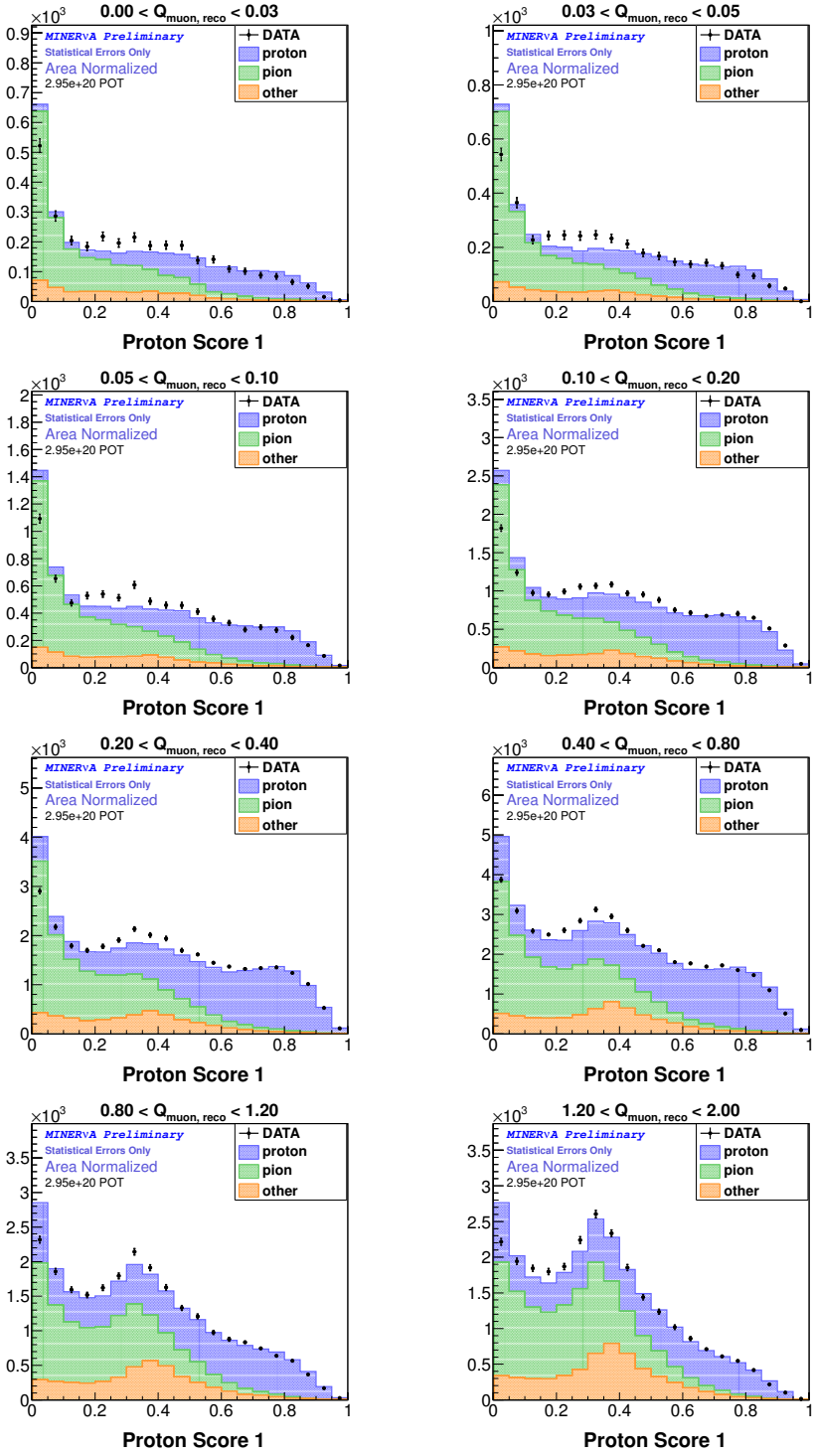

Figure A.1: Proton range score as a function of Q^2.

APPENDIX B

Recoil Energy cut to enhance the quasi-elastic-like signal

This apendix shows the different efficiency and purity values of recoil energy for different regions of Q^2. These values were used to estimate a parametrization of the non-vertex recoil as a function of the reconstructed Q^2 shown in Figure 6.6 (Section 6.3.11) for the sub-sample when only the muon is reconstructed (Figure B.1) and for the sub-sample when a muon and at least one proton candidate were reconstructed (Figure B.2). The cut is made on 92% of the efficiency plots. This enhances the quasi-elastic-like signal without significantly losing in the efficiency.

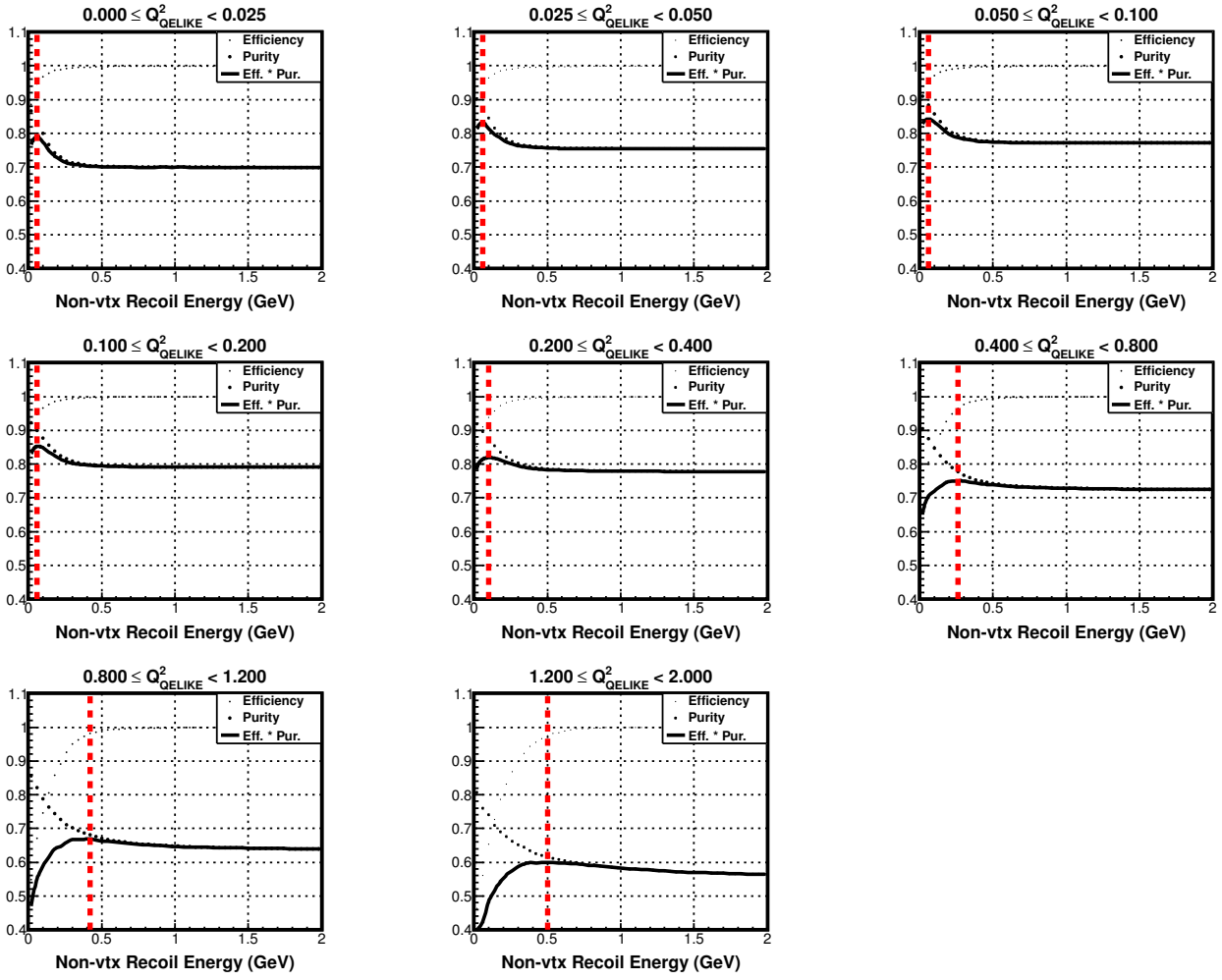

Figure B.1: Recoil Energy Cut for different ranges of Q^2. Events have only one reconstructed muon.

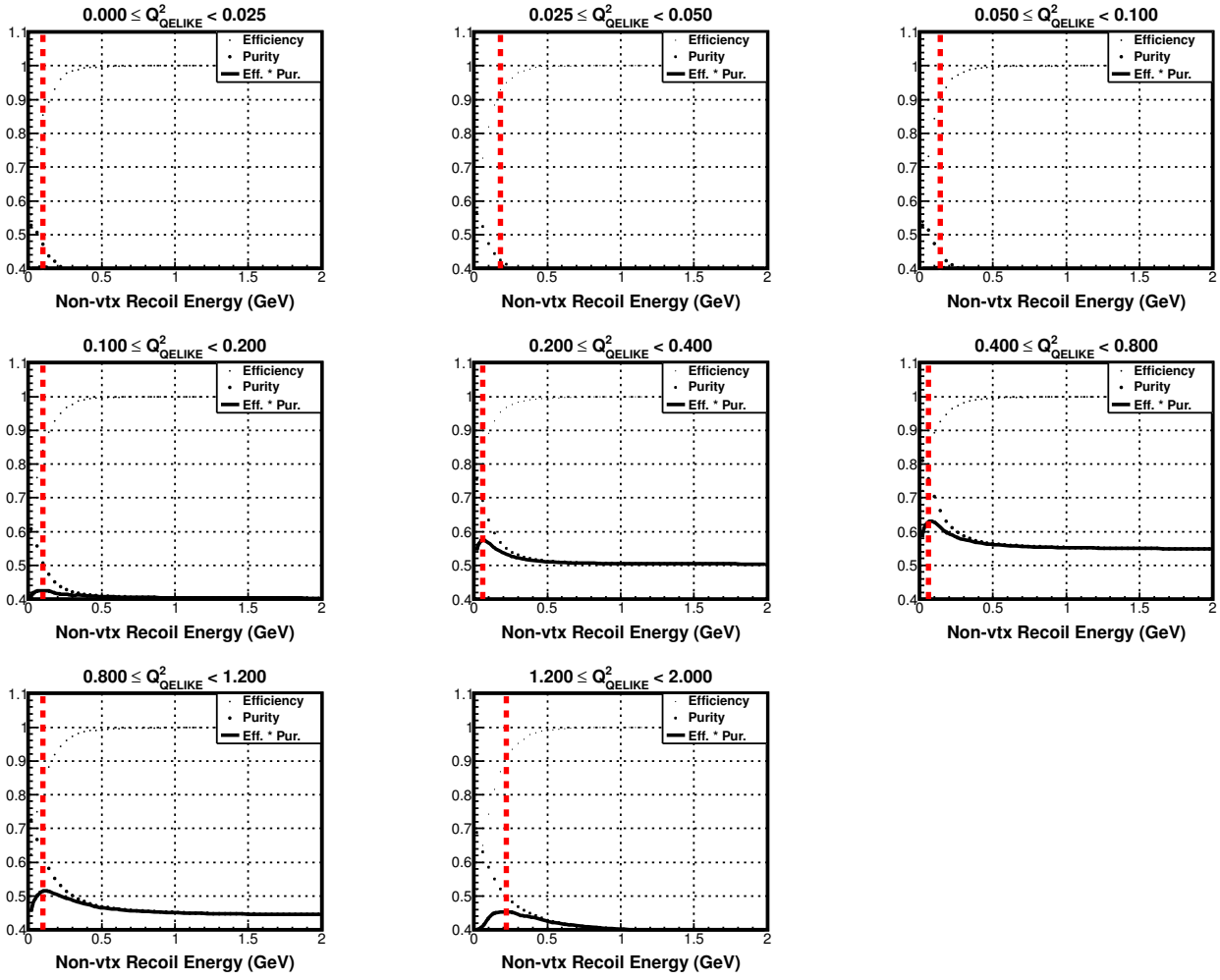

Figure B.2: Recoil Energy Cut for different ranges of Q^2. Events have one reconstructed muon and, at least, one reconstructed proton.

APPENDIX C

Systematic Errors Summaries

C.1 Systematic Error Groups after background subtraction, unfolding and efficiency correction

Section 7 shows the different steps needed to calculate a double differential cross section: Background Subtraction, Unfolding, Efficiency and Acceptance Correction and Flux and Number of neutron targets normalization.

Figure 7.18 in Section 7.6 shows the fractional systematic and statistical error summary for the double differential cross section. This appendix shows a summary of the fractional systematic and statistical errors after each of the intermediate steps before getting the cross section described in Sections 7.2, 7.3 and 7.4.

From Figure C.1 we can see that the Cross Section and FSI errors are the biggest systematic errors and the flux doesn't play a big role at this point. After the unfolding (Figure C.2), the statistical errors increase slightly due to the Bayesian technique error propagation (See reference [99]). After the Efficiency correction (Figure C.3), all systematic errors are exactly the same as in the final cross sections except for the flux. This is because the neutron target is a flat number for all universes, but the flux normalization has different universes for the flux uncertainties, making it bigger.

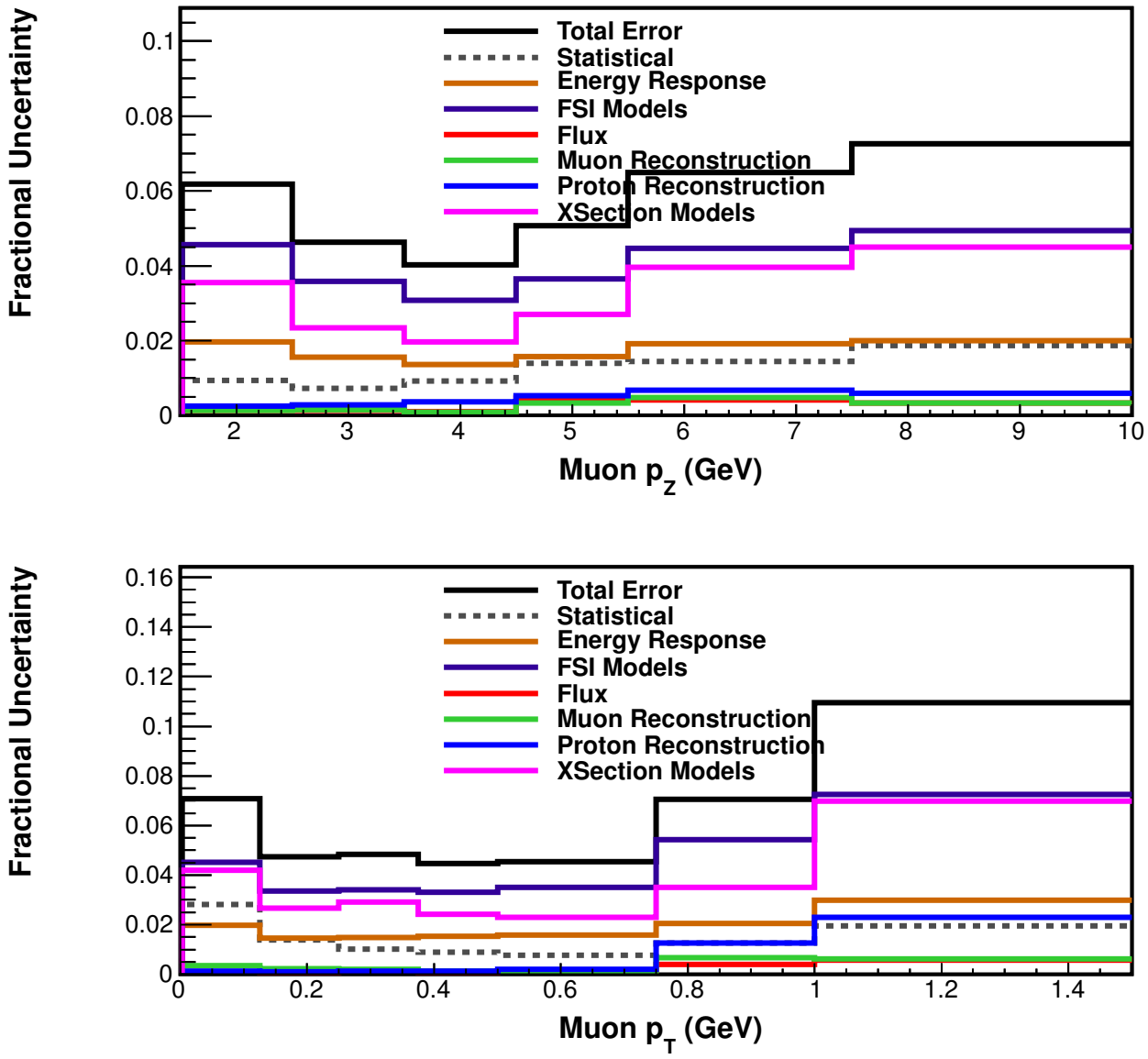

Figure C.1: Error summary in Data for Muon P_T and P_Z projections after background subtraction

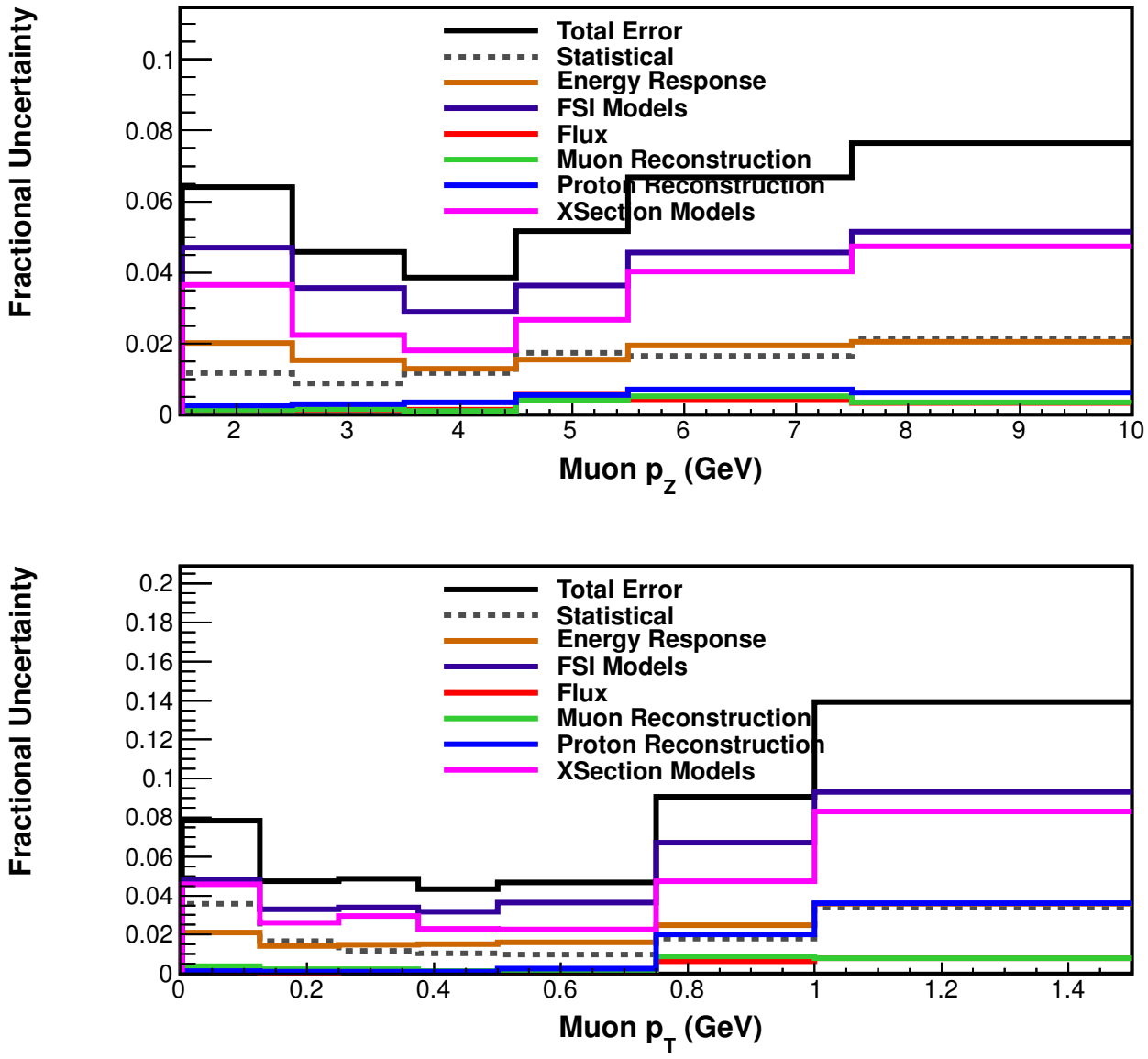

Figure C.2: Error summary in Data for Muon P_T and P_Z projections after unfolding

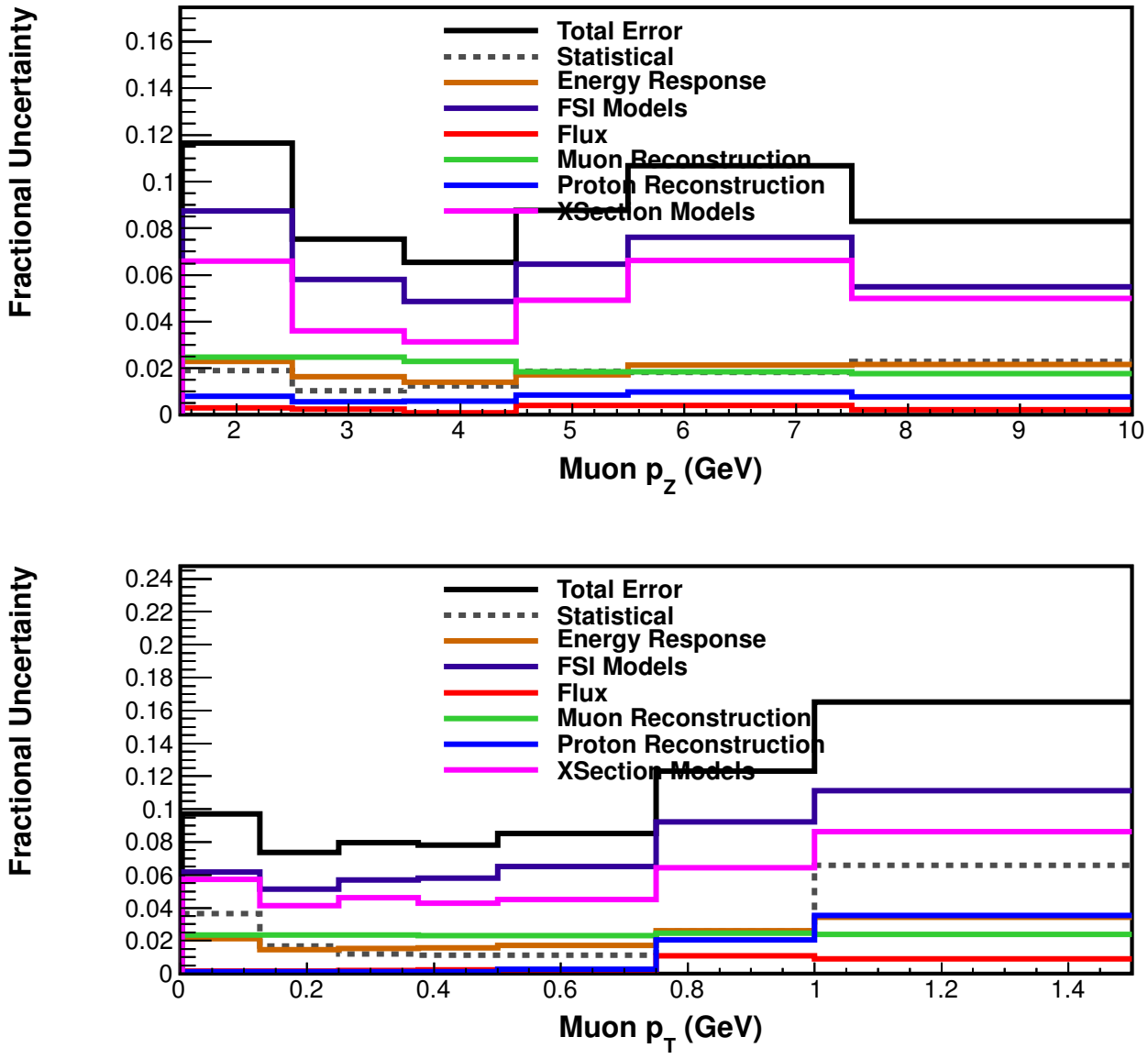

Figure C.3: Error summary in Data for Muon P_T and P_Z projections after Efficiency Correction

C.2 Systematic Error Group Components in the Cross Section

This section shows a summary of the cross section fractional errors for each error group component shown in Figure 7.18 and described from Section 7.6.1 to 7.6.5.

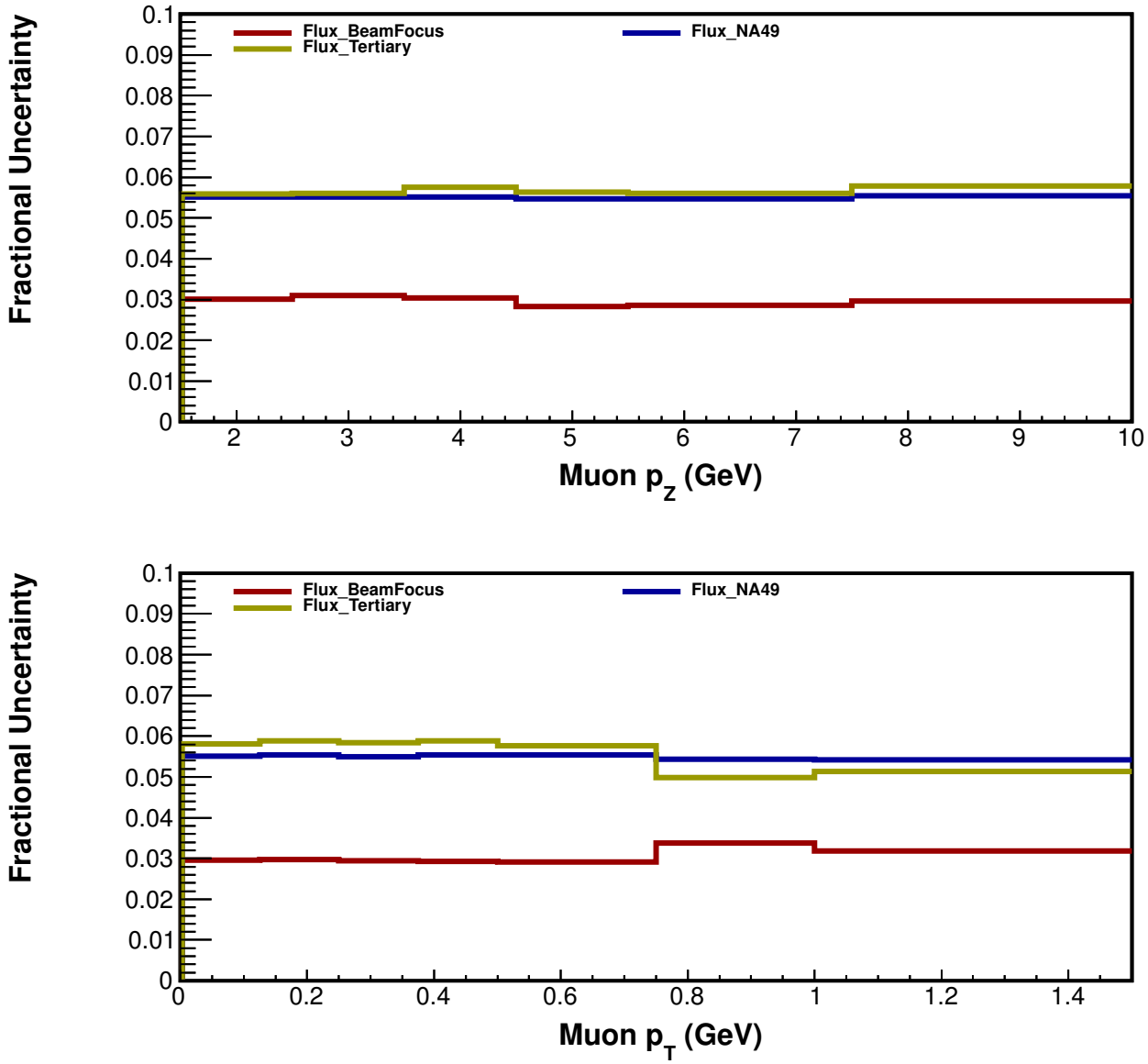

Figure C.4: Predicted neutrino flux error summary for Muon P_T and P_Z projections

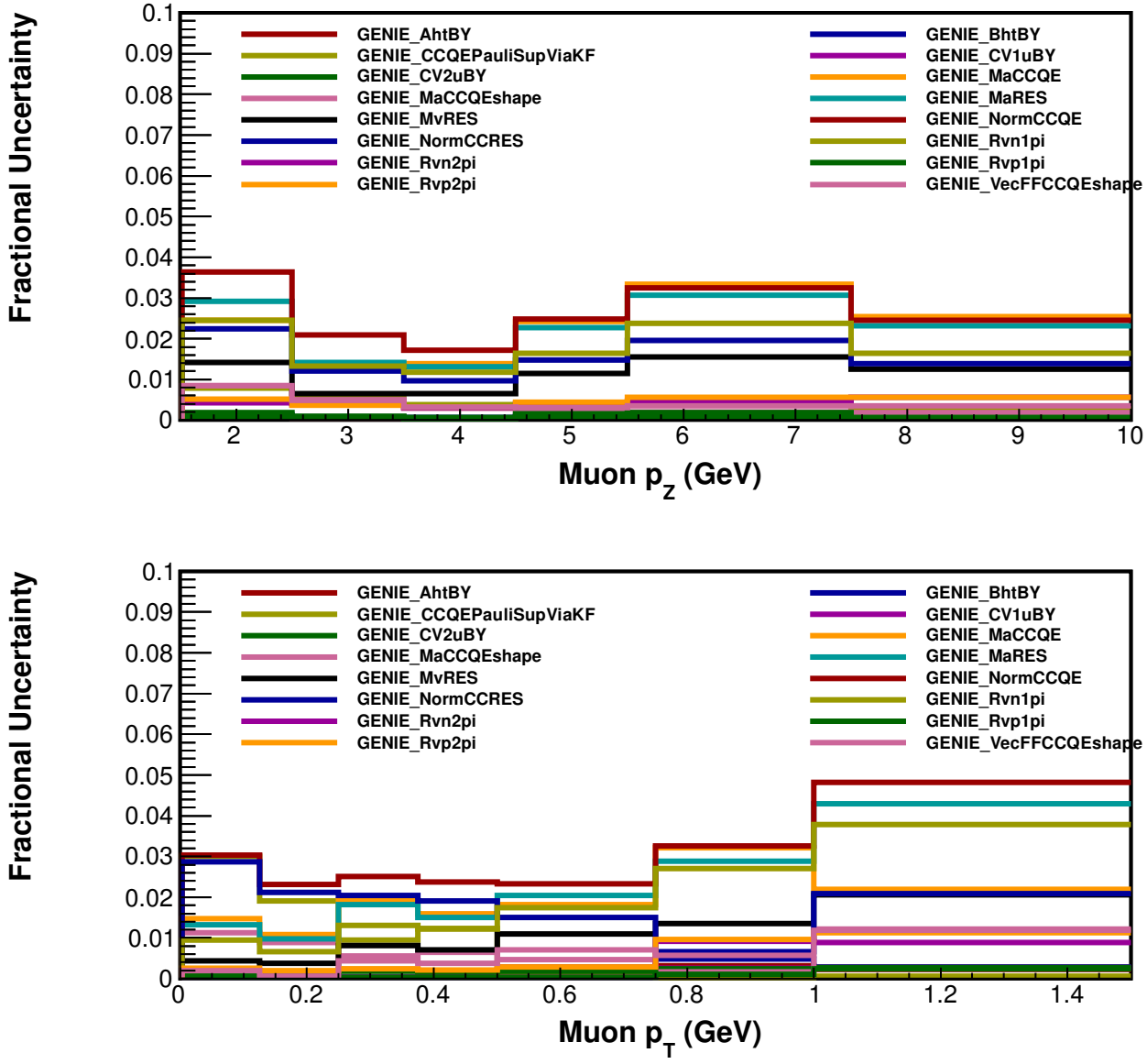

Figure C.5: Predicted Cross Section Models error summary for Muon P_T and P_Z projections

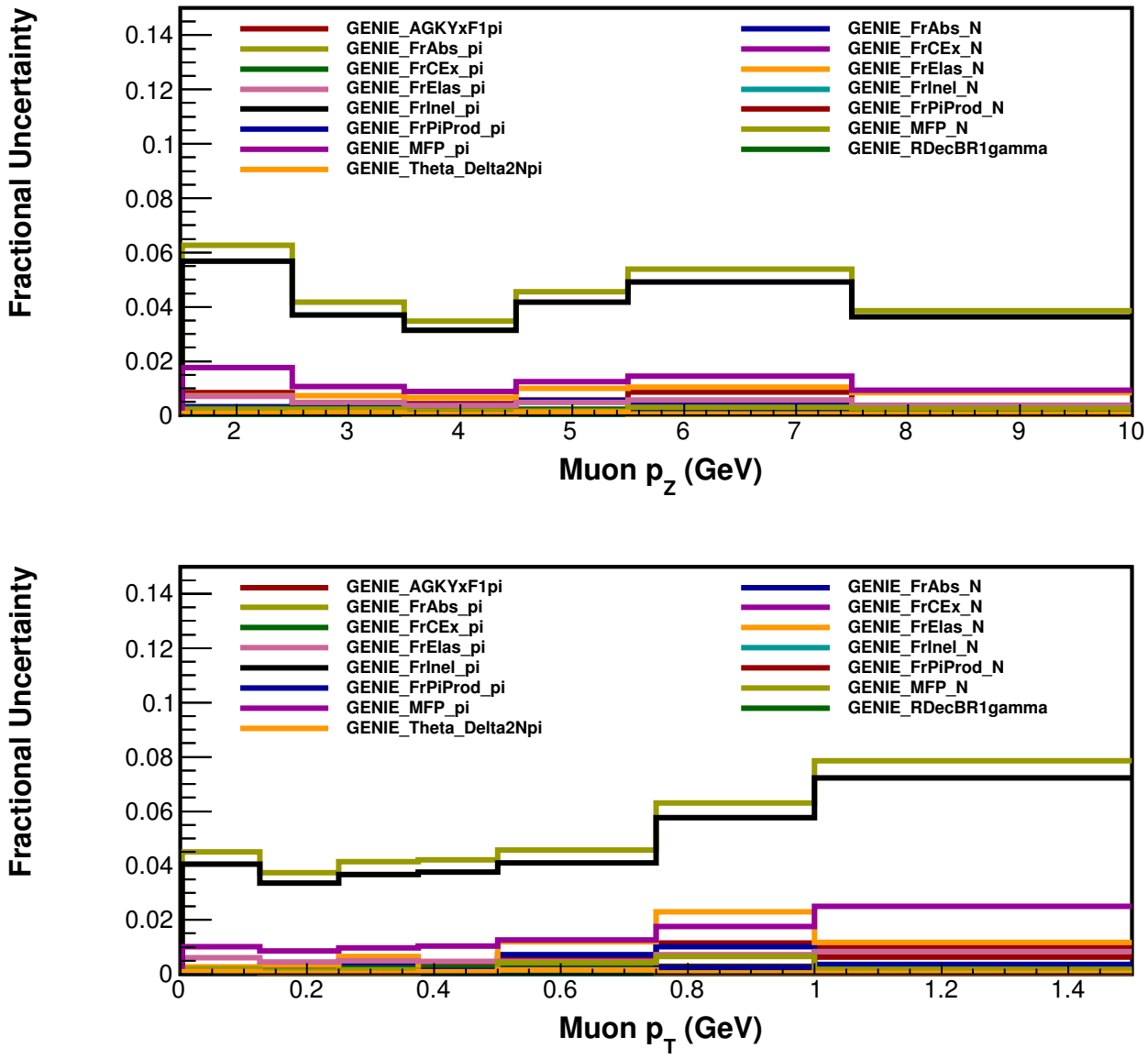

Figure C.6: Predicted Final State Interaction Models error summary for Muon P_T and P_Z projections

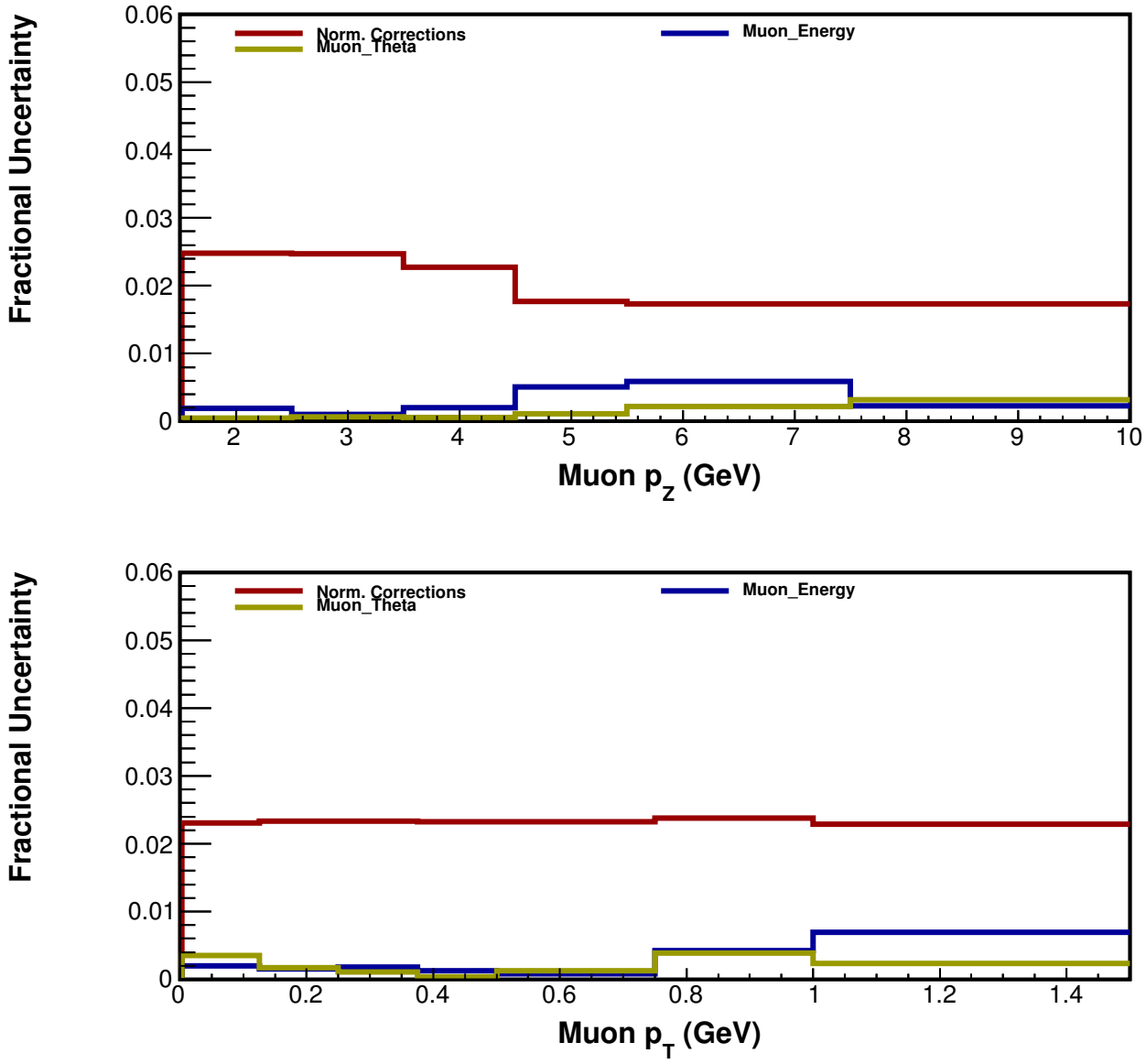

Figure C.7: Muon Energy, Angle and Normalization (described in section 7.6.5.5) error summaries for Muon P_T and P_Z projections

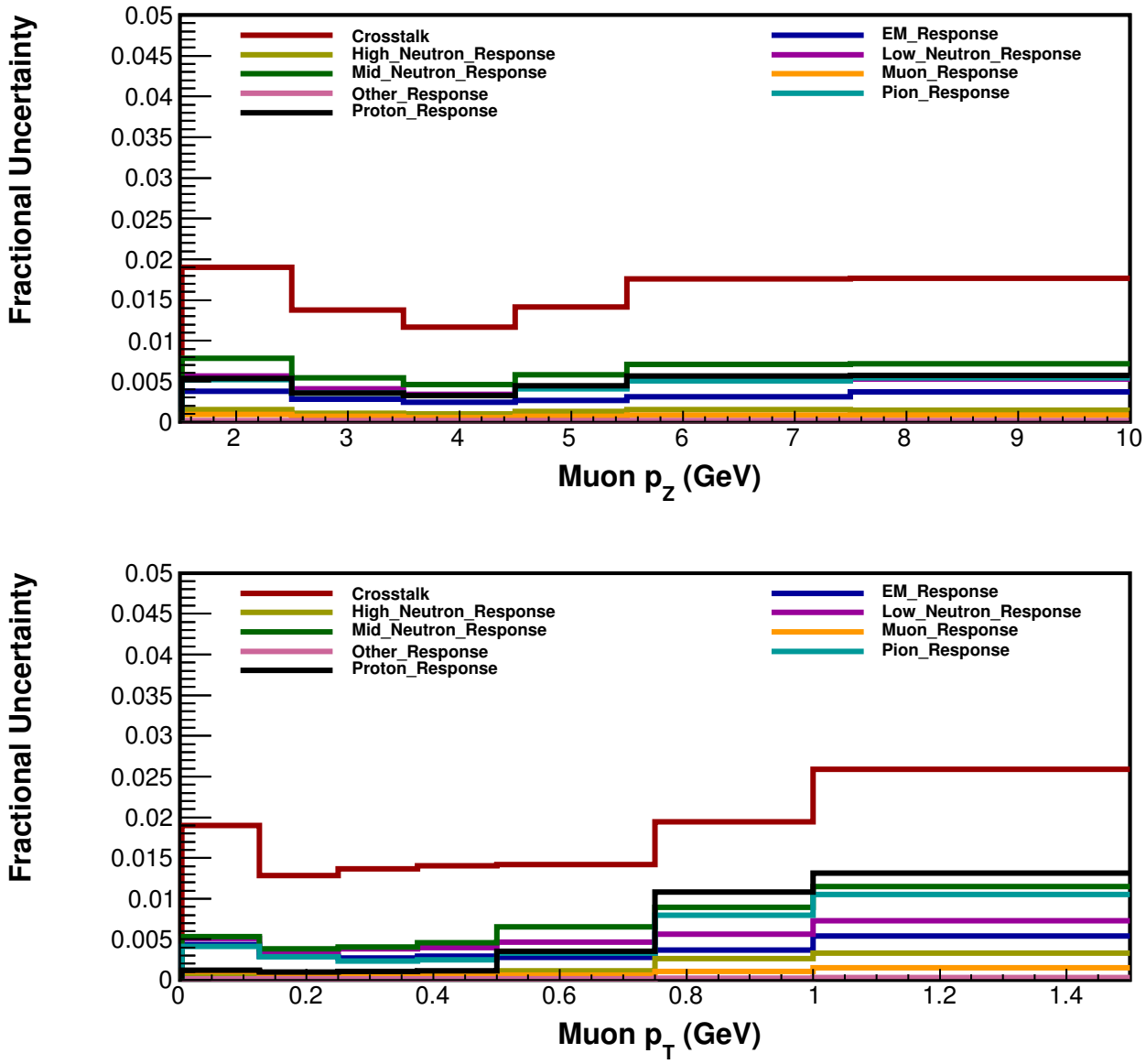

Figure C.8: Systematic uncertainties on the cross section for each particle's source which contributes to the systematic uncertainty on the detector response in the recoil energy for Muon P_T and P_Z projections

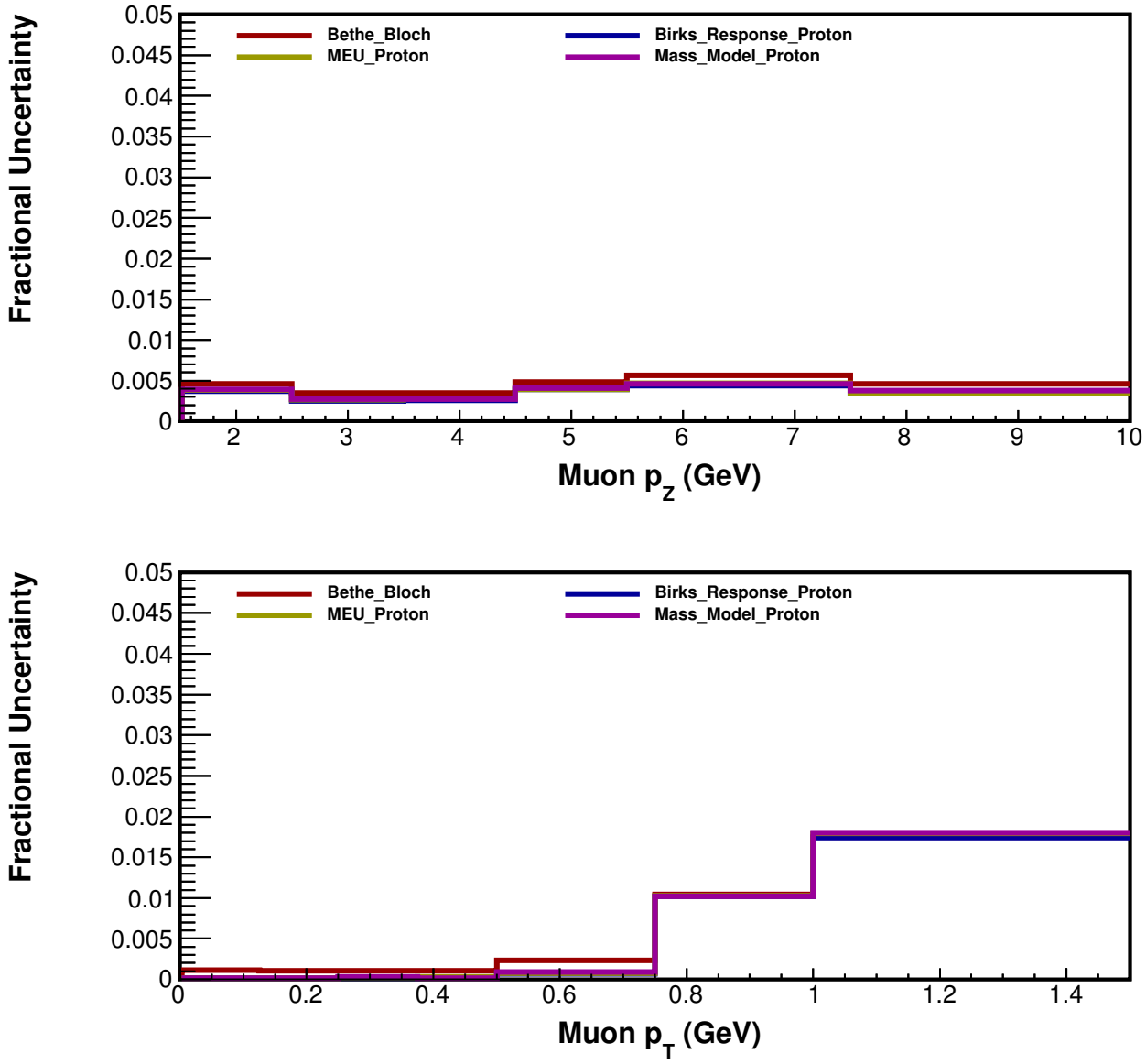

Figure C.9: Systematic uncertainties due to the various sources that contribute to the proton reconstruction systematic uncertainty for Muon P_T and P_Z projections

APPENDIX D

GENIE model parameters

This apendix provides a summary of the main reweightable uncertainties in GENIE. They are separated into uncertainties affecting the cross section model (Table D.1) and uncertainties affecting the neutrino-production of hadronic systems in nuclei (final state interactions, Table D.2).

GENIE Model Parameter	Knob Name	Description	1σ
Cross Section Models			
Modify Pauli blocking (CCQE) at low Q^2	CCQEPauliSupViaKF	Adjusts Pauli Blocking momentum cutoff	±30%
Eta (Elastic Scattering)	EtaNCEL	Adjusts eta in elastic scat. cross section	±30%
M_A (CCQE Scattering)	MaCCQE	Adjusts M_A in Llewellyn-Smith cross section, affecting shape and normalization	+25% −15%
M_A (Elastic Scattering)	MaNCEL	Adjusts M_A in elastic scat. cross section	±25%
M_A (Resonance Production)	MaRES	Adjusts M_A in Rein-Sehgal cross section, affecting shape and normalization	±20%
M_V (Resonance Production)	MvRES	Adjusts M_V in Rein-Sehgal cross section, afecting shape and normalization	±10%
CC Resonance Normalization	NormCCRES	Changes to normalization of CC Rein-Sehgal cross section	±20%
NC Resonance Normalization	NormNCRES	Changes the normalization of NC Rein-Sehgal cross section	±20%
1π production from $\nu/\hbar\nu p$ non-resonant interactions	Rvn1pi	Affects NC and CC production of single π FS from non-res inelastic (i.e Bodek-Yang) scattering	±50%
2π production from $\nu/\hbar\nu p$ non-resonant interactions	Rvn2pi	Affects NC and CC production of two π FS from non-res inelastic (i.e Bodek-Yang) scattering	±50%
1π production from $\nu p/\hbar\nu n$ non-resonant interactions	Rvp1pi	Affects NC and CC production of single π FS from non-res inelastic (i.e Bodek-Yang) scattering	±50%
2π production from $\nu p/\hbar\nu n$ non-resonant interactions	Rvp2pi	Affects NC and CC production of two π FS from non-res inelastic (i.e Bodek-Yang) scattering	±50%
Bodek-Yang parameter A_{HT}	AhtBY	tweak the Bodek-Yang parameter A_{HT}-inc. both shape and normalization effect	±25%
Bodek-Yang parameter B_{HT}	BhtBY	tweak the Bodek-Yang parameter B_{HT}-inc. both shape and normalization effect	±25%
Bodek-Yang parameter C_{v1u}	CV1uBY	tweak the Bodek-Yang parameterC_{v1u}-inc. both shape and normalization effect	±30%
Bodek-Yang parameter C_{v2u}	CV2uBY	tweak the Bodek-Yang parameterC_{v2u}-inc. both shape and normalization effect	±40%

Table D.1: Cross section model uncertainties

GENIE Model Parameter	Knob Name	Description	1σ
FSI Models			
AGKY hadronizatoin model -X_F distribution	AGKYxF1pi	tweak xF distribution for low multuplicity ($N+\pi$) DIS FS produced by AGKY	±20%
Nucleon fates - absorption	FrAbs_N	tweak absorption probability for nucleons, for given total rescattering probability	±20%
Pion fates - absorption	FrAbs_pi	tweak absoroption probability for pions, for given rescattering probability	±30%
Nucleon fates - charge exchange	FrCEx_N	tweak charge exchange probability for nucleons, for given total rescattering probability	±20%
Pion fates - charge exchange	FrCEx_pi	tweak charge exchange probability for pions, for given total rescattering probability	±50%
Nucleon fates - Elastic	FrElas_N	tweak elastic probability for nucleons, for given total rescattering probability	±30%
Pion fates - Elastic	FrElas_pi	tweak elastic probability for pions, for given total rescattering probability	±10%
Nucleon fates - Inelastic	FrInel_N	tweak inelastic probability for nuclons, for given total rescattering probability	±40%
Pion fates - Inelastic	FrInel_pi	tweak inelastic probability for pions, for given total rescattering probability	±40%
Nucleon fates - pion production	FrPiPron_N	tweak pion production probability for nucleons, for given total rescattering probability	±40%
Pion fates - pion production	FrPiProd_pi	tweak pion production probability for pions, for given total rescattering probability	±20%
Nucleon mean free path	MFP_N	tweak mean free path for nucleons	±20%
Pion mean free path	MFP_pi	tweak mean free path for pions	±20%
Resonance decay branching ratio to photon	RDecBR1gamma	tweak *Resonance* $\rightarrow X+$ gamma branching ratio, eg $\Delta^+(1232) \rightarrow p\gamma$	±50%

Table D.2: Final State Interaction model uncertainties

APPENDIX E

Summary of contributions to the MINERνA experiment

E.1 Special Runs

E.1.1 Introduction

As stated in Section 4.1 producing neutrinos of the same energy, but in different beam configurations, is one of the techniques used to constrain the flux in MINERνA . These flexible beam configurations are known as *Special Runs* and are used to tune the hadron production yields to match MINERνA data.

Moving the target with respect to the horns, as shown in Figure E.1 allows us to vary which pions are focused, hence helping to deconvolve systematics with respect to neutrino beam focusing and π/K production off target. Besides the target position, the horn current can also be changed to vary the transverse momentum spectrum. Figure E.2 shows the transverse and longitudinal momentum $P_T vs P_Z$ phase space for different special run configurations. Table E.1 summarizes the energy configuration according to the target-horn distance.

Target-Horn Distance	Energy Configuration
10 cm	Low Energy
100 cm	Medium Energy
250 cm	High Energy

Table E.1: A summary of energy configurations with respect to the distance between the target and Horn 1 shown in Figure E.1

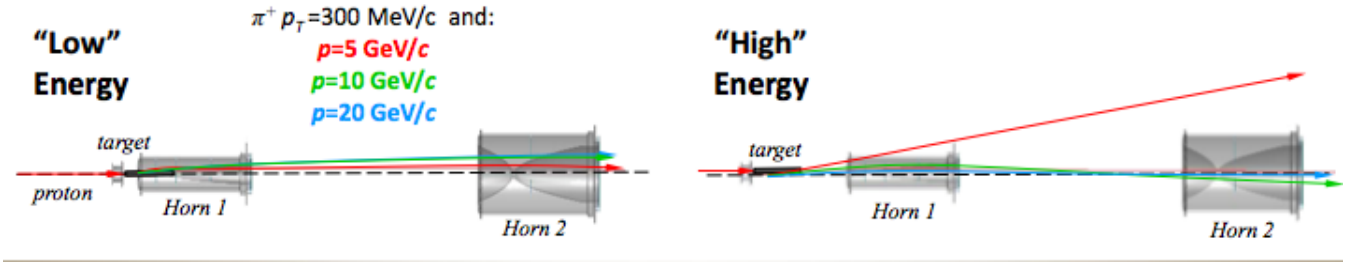

Figure E.1: Target configuration from low to high energy.

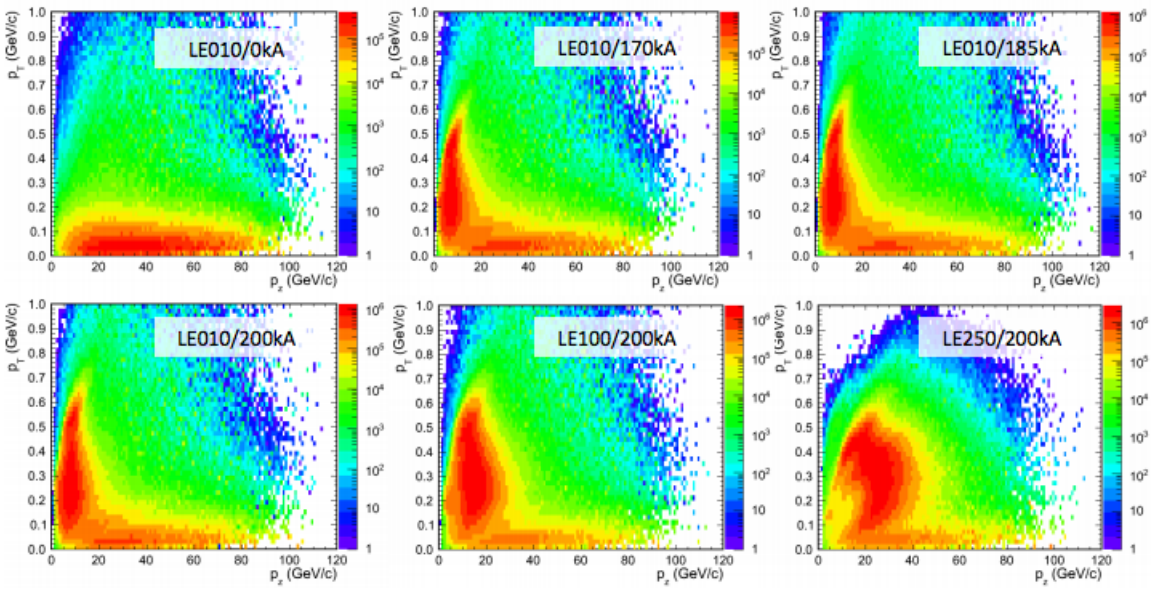

Figure E.2: $P_T vs P_Z$ phase space for different special run configurations.

E.1.2 Data Quality Checks

Figure 6.1 shows the neutrino data recorded by the MINERνA experiment between November of 2009 and April of 2012. There, you can see special runs data were taken in August 2010 and April, June and September 2011. These data need to be synchronized with MINOS and discarded were there could be potential problems between MINERνA and MINOS databases or readout problems. These studies were carried out during my stay in the experiment and can be seen in references [113, 114, 115, 116, 117].

The results of these studies validated the special runs data and allowed us to produce the neutrino energy for these configurations. Figure E.3 shows the neutrino energy for this special data. This is an actively referenced plot in the experiment.

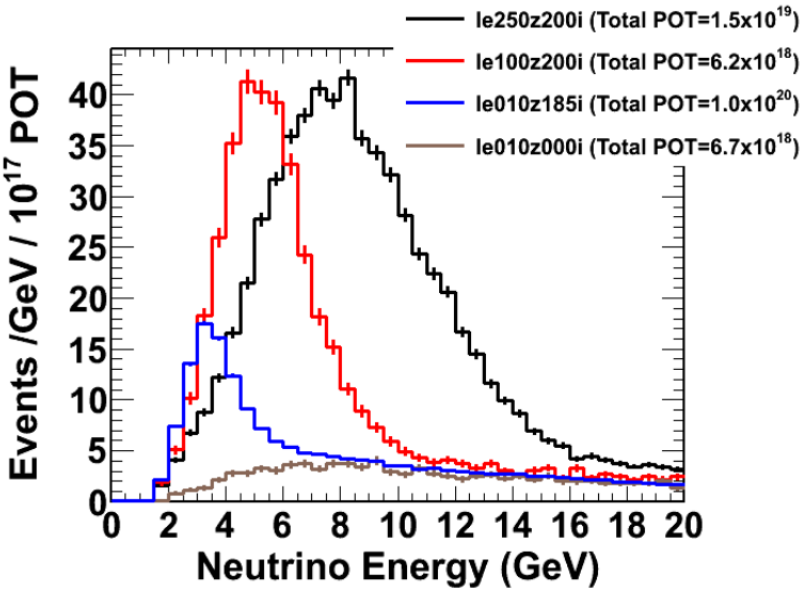

Figure E.3: Neutrino energy spectrum for special runs data.

E.2 Systematic Errors

The systematic errors in the experiment are calculated using the covariance matrices produced from the "Many Universes" method.

E.2.1 Many Universes Method

This is a method for varying model parameters with a known covariance matrix to produce an error band representing the effect of model uncertainties on any distribution influenced by the model. Each variation represents a universe in this method.

The influence can be whole (the model predicts all features of the distribution) or partial (the model only predicts some features). The influence can be direct (the model predicts the distribution) or indirect (the distribution is a function of the quantity that the model predicts).

See reference [101] for more details about this method.

E.2.2 The covariance Matrix

As mentioned in Section 7.6, there are different universes for each parameter shifted or variated. If they are shifted once or twice, the $\pm 1\sigma$ uncertainties are used, otherwise 100 different variations are selected from a Gaussian distribution with a mean equal to 0 and a width equal to σ.

For each error a covariance matrix is calculated using the information from these universes:

$$cov_{i,j} = \frac{1}{N}\sum_{k=1}^{N}(x_{ki} - \bar{x_i})(x_{kj} - \bar{x_j}) \tag{E.1}$$

After this, the square root values of the diagonal elements of this matrix is equivalent to the associated systematic error.

Covariance Calculation in the Minerva Framework

We use a a class called MnvH1D to calculate the covariance matrices on the fly. This class depends on other sub-classes that support these universes and, inside them, specific functions in order to calculate, store and delete these matrices were written as a contribution to the experiment. Details about this work can be seen in reference [118].

The covariance functions are used for the systematic errors.

Multidimensional Classes

Due to the fact that the experiment only supported the Many Universes method for one dimensional analyses and, since my analysis was a two-dimensional one, multiple classes in order to support this method and the covariance calculations in two and three dimensions were also written. Details of this work can be found in references [119, 120].

E.3 Unfolding

Section 7.3 describes the unfolding technique that uses the statistical relation between the true kinematic variable and the measured quantity to correct measured quantities that are smeared out due to limited measurement accuracy (finite resolution) of the detector,. This was implemented as a common Tool for multiple dimensions for the experiment during my stay.

The tool is able to unfold both the cv and the multiple universes that are used to estimate the systematic errors through the covariance matrix calculation. The following section briefly describes the technical details about this tool.

E.3.1 Introduction

Finite detector resolution and limited acceptance require particle physics experiments to apply unfolding methods. The UnfoldUtils package is an interface to RooUnfold[121] used at MINERνA to apply different unfolding algorithms for this purpose and incorporates the ability to use specific MINERνA classes such as MnvH1D so we can store the unfolded systematic error band universes too.

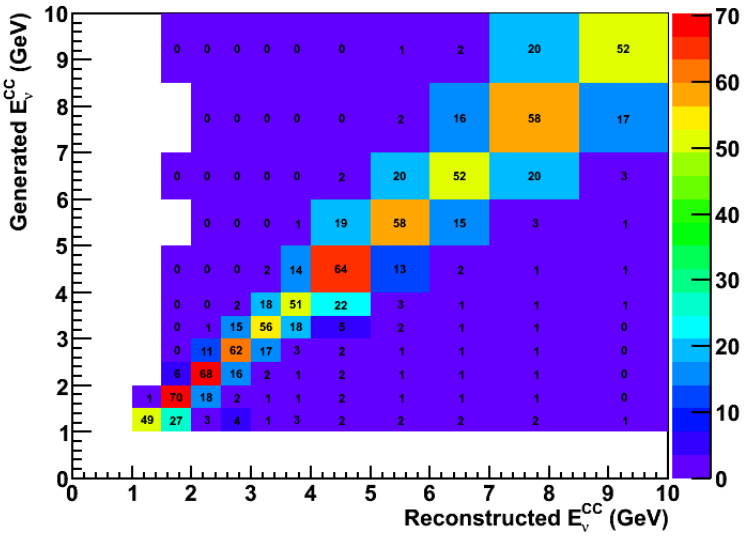

Figure E.4: Inclusive ν migration histogram in the tracker

The Migration Matrix

This is built from a two-dimensional histogram filled with the *True* values for the Y axis and the *Reconstructed* ones for the X axis (signal only).

The result shows how the spread from the reconstructed values is distributed around the True bins.

Figure E.4 shows a migration histogram example built from the CCInclusive Analysis on the Tracker for playlist 1.

E.3.2 Unfolding Methods

E.3.2.1 Iterative Bayes' theorem

This algorithm uses the method described by D'Agostini [99]. It uses the bayes' theorem repeatedly to invert the response matrix. The regularization parameter in this algorithm is the number of iterations.

Errors

The Unfolded distribution $\hat{n}(C_i)$ as the result of applying the unfolding matrix M_{ij} to the measurements $n(E_j)$ is given by:

$$\hat{n}(C_i) = \Sigma_{j=1}^{n_E} M_{ij} n(E_j)$$

Where:

- $\hat{n}(C_i)$: Unfolded Distribution
- M_{ij}: Unfolding Matrix
- $n(E_j)$: Folded Distribution

The error propagation in the RooUnfold Bayesian method is defined by :

$$\frac{\partial \hat{n}(C_i)}{\partial n(E_j)} = M_{ij} + \Sigma_{k=1}^{n_E} M_{ik} n(E_k) \left(\frac{1}{n_0(C_i)} \frac{\partial n_0(C_i)}{\partial n(E_j)} - \Sigma_{l=1}^{n_C} \frac{\epsilon_l}{n_0 C_l} \frac{\partial n_0(C_l)}{\partial n(E_j)} M_{lk} \right)$$

And the covariance matrix can be computed from the error propagation matrix :

$$V(\hat{n}(C_k), \hat{n}(C_l)) = \Sigma_{i,j=1}^{n_E} \frac{\partial \hat{n}(C_k)}{\partial n(E_i)} V(n(E_i), n(E_j)) \frac{\partial \hat{n}(C_l)}{\partial n(E_j)}$$

More detailed information can be found at [99].

E.3.2.2 Single Value Decomposition

The algorithm described by A. Hoecker and V. Kartvelishvili is implemented in TSVDUnfold, which is available at ROOT [122] and this package provides an interface to that class.

The unfolding procedure is based on singular value decomposition of the response matrix. The regularisation of the unfolding is implemented via a discrete minimum-curvature condition.

Errors

The algorithm description and error propagation is fully described in reference [123].

E.3.2.3 Bin by Bin

This method uses the algorithm described by G.Cowan in section 5 of [124]. This method is relatively simple and is based on multiplicative correction factors derived from the MonteCarlo by looking at each bin individually. True and Measured distributions must have the same binning

The estimator for bin i of the unfolded distribution is :

$$\hat{n}_i = C_i(n_i - \beta_i)$$

The term β_i means the distribution has been background subtracted already before applying the correction factors, and C_i is determined by the ratio:

$$C_i = \frac{\mu_i^{MC}}{\nu_i^{MC}}$$

Where μ^{MC} and ν_i^{MC} are obtained from the Montecarlo True and Reco Signal only.

E.3.2.4 Simple Inversion

This algorithm is described by G.Cowan in section 4 of [124]. It works simply by inverting the response matrix to get the unfolded distribution.

If the off-diagonal elements of the migration matrix is too large or the bins size too small compared to the measurement resolution, this method is not so accurate, which is why more effective methods are usually needed.

E.3.3 Using the UnfoldUtils Tool

The tool can currently unfold MnvH1D (and TH1D) histograms including their Universes using the same central value based Migration Histogram.

Aditionally, there are a couple specific functions for the ν-CCQEOneTrack and CCInclusive on the Tracker analyses with an extra option to unfold the universes using different migration histograms generated for each universe.

The steps necessary to use the UnfoldUtils Package are the following:

1. Get, compile UnfoldUtils package and include the package into your CMT requirements file.

2. Make sure to include the MnvUnfold header file to your analysis script.

   ```
   #include "MinervaUnfold/MnvUnfold.h"
   ```

3. If you use a Makefile, be sure to set your INCLUDE and LDLIBS variables properly, so it can find UnfoldUtils. There is a python script that generates the Makefile at `$UNFOLDUTILS/scripts/GenerateMakefile.py`

4. An object needs to be created in order to use MnvUnfold functions, where the first parameter will be a MnVH1D/TH1D pointing initially to NULL, which will contain the unfolded distribution.

```
MinervaUnfold::MnvUnfold unfold;
MnvH1D *h_unfolded = NULL; //point to NULL

unfold.UnfoldHisto( h_unfolded,   //MnvH1D unfolded output
    h_migration, //TH2D
    h_folded,   // Data
    RooUnfold::kBayes, // Method Others: kSVD, kInvert, kBinByBin
    2., // Regularization parameter
    true //Unfold Universes in MnvH1D too
    );
```

Here:

- `h_unfolded`: Unfolded Variable
- `h_migration`: Migration TH2D histogram
- `h_folded`: Distribution to unfold
- `RooUnfold::kBayes` : Bayesian Unfolding Method. Other methods available are:
  - `RooUnfold::kSVD` : Singular Value Decomposition Method
  - `RooUnfold::kInvert`: Simple Inversion Matrix Method
  - `RooUnfold::kBinByBin`: Bin by Bin Method
- `2.` : Regularization Parameter (applicable for Bayes and SVD methods)
- `true` : Unfold MnvH1D systematic universes using `h_migration` too.

More details on the Tool can be found in references [125, 126, 127].

Bibliography

[1] MINERvA Collaboration, Design, Calibration and Performance of the MINERvA Detector, Nucl. Inst. and Meth. A743 (2014) 130.

[2] Proposal to perform a High Statistics Neutrino Scattering Experiment using a fine-grained detector in the NUMI beam

[3] von Bayer, O. Hahn, L. Meitner, Phys. Zeitschrift, 12, January, 1911, p. 378

[4] Chadwick, J., Verh. Deutsch. Phys. Ges., 16, 383 (1914)

[5] C.D. Ellis, B.A. Wooster, The average energy of desintegration of Radium E,Proc. Roy. Soc. A117(1927) 109-123

[6] B. Pontecorvo, "Mesonium and anti-mesonium". Zh. Eksp. Teor. Fiz. 33, 549–551. reproduced and translated in Sov. Phys. JETP 6, 429 (1957).

[7] Z. Maki, M. Nakagawa, and S. Sakata, "Remarks on the Unified Model of Elementary Particles". Progress of Theoretical Physics 28, 870 (1962)

[8] B. Pontecorvo, "Neutrino Experiments and the Problem of Conservation of Leptonic Charge". Zh. Eksp. Teor. Fiz. 53, 1717. reproduced and translated in Sov. Phys. JETP 26, 984 (1968).

[9] Brookhaven's Alternating Gradient Synchroton, Science 5 December 1958: Vol. 128 no. 3336 pp. 1393-1401.

[10] F. J. Hasert *et al.* (Gargamelle),"Observation of neutrino-like interactions without muon or electron in the Gargamelle neutrino experiment", Phys. Lett. **B46** (1973) 138.

[11] M. L. Perl,"The Discovery of the tau lepton", In *Stanford 1992, The rise of the standard model* 79-100

[12] K. Kodama *et al.* [DONUT Collaboration], "Observation of tau neutrino interactions", Phys. Lett. B **504**, 218 (2001).

[13] http://www.fnal.gov/

[14] ALEPH Collaboration:D. Decamp et al., "Determination of the Number of Light Neutrino Species", Phys. Lett. B 231(1989)519.

[15] Delphi Collaboration:P.A. Aarnio et al.,"Measurement of the Mass and Width of the Z0 Paricle from Multi-Hadronic Final States Produced in the e+ e- Annihilation", Phys. Lett. B 231 (1989)539.

[16] L3 Collaboration:B. Adeva et al.,"A Determination of the Properties of the Neutral Intermediate Vector Boson Z0", phys. Lett. B 231 (1989)509.

[17] OPAL Collaboration:M.Z. Akrawy et al.,"Measurement of the Z0 Mass and Width with the OPAL Detector at LEP", Phys. Lett. B bf 231 (1989)530.

[18] C. Athanassopoulos et ala., "Candidate Events in a Search for Anti-Muon-Neutrino - Anti-Electron-Neutrino Oscillations", Phys. Rev. Lett. 75, 2650, 1995.

[19] Tina J. Leitner, "Neutrino Interactions with Nucleons and Nuclei",(2005).

[20] C.S. Wu et al., Phys. Rev. 105 (1957)1413.

[21] M. Goldhaber, L. Grodzins, and A.W. Sunyar, Helicity of neutrinos, Phys. Rev. 109 (1958)1015.

[22] E. K. Akhmedov, 1997, hep-ph/9705451, Fourth International Solar Neutrino Conference, Heidelberg, Germany, 8–11 Apr 1997.

[23] R. Davis, "A review of the Homestake solar neutrino experiment,", Prog. Nucl. Phys. 32, p13 (1994).

[24] K. Lande, Proceedings of Neutrino 96, p25.

[25] V. N. Gavrin, "Solar neutrino and Cr-51 results from SAGE", Proceedings of Neutrino 96, p14.

[26] P. Anselmann et al., "Solar neutrinos observed by GALLEX at Gran Sasso", Phys. Lett. B285 (1992) 376-389

[27] K. Abe et al. (Super-Kamiokande Collaboration), Solar neutrino results in Super-Kamiokande-I, Phys.Rev.D73:112001,(2006).

[28] SNO Collaboration, "Independent Measurement of the Total Active 8B Solar Neutrino Flux Using an Array of He3 Proportional Counters at the Sudbury Neutrino Observatory", Phys. Rev. Lett. 101, 111301(2008).

[29] W.N. Cottingham and D.A Greenwood, "An Introduction to the Standard Model of Particle Physics", Second Editions, Cambridge University, xv,42 (2001).

[30] T. Kajita et. al., Proceedings of Neutrino 98 ,Nucl.Phys.Proc.Suppl. 77 (1999) Takayama, Japan, June 4-9, 1998.

[31] R. M. Bionta et. al., Phys. Rev. Lett. 58, p1494 (1987)

[32] W. W. M. Allison et. al., Phys. Lett. B391, p491 (1997)

[33] Ch. Berger et. al., Phys. Lett. B227, p489 (1994).

[34] M. Aglietta et. al., Europhys. Lett. 8, p611 (1989).

[35] T. Kajita, "Atmospheric neutrinos", New J. Phys. **6** (2004) 194.

[36] The Super-Kamiokande Collaboration, "Evidence for oscillation of atmospheric neutrinos", Phys. Rev. Lett. 81 (1998) 1562-1567

[37] D. Perkins, "Introduction to High Energy Physics", 4th edition, Cambridge University Press, 246 (2000).

[38] K. Zuber, "Neutrino Physics", Institute of Physics Publishing Bristol and Philadelphia, Oxford, 22,32,57(2004).

[39] A. Thomas and W. Weise, "The structure of the nucleon", Wiley-VCH, 8 (2001).

[40] D. Griffits, "Introduction to Elementary Particles", John Wiley and Sons, Inc, (1987).

[41] “Introduction to Particle Physics”, C.J. Solano Salinas, K. Hurtado, C. Romero. AIP Conf.Proc.1123:13-29,2009.

[42] C. Giunti and C. Kim, "Fundamentals of Neutrino Physics and Astrophysics",193 (2007).

[43] J. L. Hewett *et al.*, "Fundamental Physics at the Intensity Frontier", arXiv:1205.2671[hep-ex].

[44] R. Placakyte,"Parton Distribution Functions", arXiv:1111.5452 [hep-ph].

[45] D. Rein and L. M. Sehgal,"Neutrino Excitation of Baryon Resonances and Single Pion Production", Annals Phys. **133** (1981) 79.

[46] P.A Rodriguez, "Comparing pion production models to MiniBooNE data", arXiv:1402.4709 [hep-ex]

[47] V. T. McGary,"NC Coherent pi0 Production in the MiniBooNE Antineutrino Data", arXiv:0806.2347 [hep-ex].

[48] C. H. Llewellyn Smith, Phys. Rep., 3, 261, 1972.

[49] S. K. Singh and E. Oset, "Quasielastic neutrino (anti-neutrino) reactions in nuclei and the axial vector form-factor of the nucleon", Nucl. Phys. A542 (1992) 587–615.

[50] S. Galster et al., "Elastic electron - deuteron scattering and the electric neutron form-factor at four momentum transfers 5-fm**-2 ¡ q**2 ¡ 14-fm**-2", Nucl. Phys. B32 (1971) 221–237.

[51] Nambu, Yoichiro,"Axial Vector Current Conservation in Weak Interactions", Phys. Rev. Lett. V4 (1960)

[52] H. S. Budd, A. Bodek, and J. Arrington, "Modeling quasi-elastic form factors for electron and neutrino scattering," arXiv:hep-ex/0308005.

[53] V. Bernard, L. Elouadrhiri and U. G. Meissner, "Axial Structure of the Nucleon", J. Phys. G28, R1 (2002), hep-ph/0107088.

[54] Shneor R, et al. Phys. Rev. Lett. 99:072501 (2007)

[55] Sargsian MM, et al. Phys. Rev. C 71:044615 (2005)

[56] Schiavilla R, et al. Phys. Rev. Lett. 98:132501 (2007)

[57] H. Gallagher, G. Garver and G.P.Zeller, "Neutrino-Nucleus Interactions", Annual Review of Nuclear and Particle Science 2011. 61:355–78.

[58] M.B. Barbaro. "Nuclear effects in charged-current quasielastic neutrino- nucleus scattering". J.Phys.Conf.Ser. 336:012024 (2011).

[59] Singh, S. K., and E. Oset, 1992, Nucl. Phys. A542, 587.

[60] Aguilar-Arevalo, A., et al., 2010a, Phys. Rev. D 81, 092005.

[61] Lyubushkin, V., et al., 2009, Eur. Phys. J. C 63, 355.

[62] J. A. Formaggio and G. P. Zeller,"From eV to EeV: Neutrino Cross Sections Across Energy Scales", Rev. Mod. Phys. **84**, 1307 (2012), arXiv:1305.7513 [hep-ex].

[63] A. A. Aguilar-Arevalo et al. (MiniBooNE Collaboration), "First measurement of the muon neutrino charged current quasielastic double differential cross section", Phys. Rev. D 81, 092005 – Published 28 May 2010.

[64] A. Fiorentini et. all (MINERνA Collaboration), "Measurement of Muon Neutrino Quasi-Elastic Scattering on a Hydrocarbon Target at Enu $\tilde{3}$.5 GeV", Phys. Rev. Lett. 111, 022502 (2013).

[65] J. Hylen et al., NuMI Technical Design Handbook, Internal NuMI report (2003).

[66] , S. E. Kopp,"The NuMI beam at FNAL and its use for cross-section measurements", arXiv:0709.2737 [hep-ex].

[67] MINOS Collaboration:D.G. Michael et al., Observation of Muon Neutrino Disappearance with the MINOS Detector in the NuMI Neutrino Beam, Phys. Rev. Lett. 97 (2006)191801.

[68] A. Fiorentini, "The MINERvA Detector", Eighth International Workshop on Neutrino proceedings,2012

[69] Photomultiplier Tubes, Hamamatsu Handbook, Third Edition (2007).

[70] Berkeley Laboratory, "Nuclear Science—A Guide to the Nuclear Science Wall Chart", http://www.lbl.gov/abc/wallchart/teachersguide/pdf/Chap11.pdf

[71] J. Estrada, C. Garcia, B. Hoeneisen and P. Rubinov,"MCM II and the Trip Chip", August 2002, FERMILAB-TM-2226.

[72] G.N. Perdue et al. (MINERvA collaboration), "The MINERvA data acquisition system and infrastructure", Nucl. Inst. and Met., Phys. Res. Sect. A, 694(0):179 – 192, (2012). 30.

[73] Geant4 Collaboration, Summary of Hadronic Processes, Models and Cross Sections for Physics List FTFP Model (2012).

[74] Geant4 Collaboration, Summary of Hadronic Processes, Models and Cross Sections for Physics List Bertini Cascade (2012).

[75] A. Heikkinen, N. Stepanov and J. P. Wellisch, "Bertini intranuclear cascade implementation in GEANT4", eConf C **0303241**, MOMT008 (2003), arXiv:0306008

[76] Vladimir UZHINSKY et/ al, "Development of the Fritiof Model in Geant4", Joint International Conference on Supercomputing in Nuclear Applications and Monte Carlo 2010, http://geant4.web.cern.ch/geant4/results/papers/Fritiof-MC2010.pdf

[77] S. Kopp et al, Nucl. Instr. Meth., 568, 503-519 (2006)

[78] J. Park, "Neutrino-Electron Scattering in MINERvA for Constraining the NuMI Neutrino Flux", MINERvA Internal Note No. 041 (2013)

[79] A. Bodek et al., "Methods to Determine Neutrino Flux at Low Energies: Investigations of the low ν Method", Eur.Phys.J C72:1973 (2012)

[80] C. Alt *et al.* [NA49 Collaboration],"Inclusive production of charged pions in p+C collisions at 158-GeV/c beam momentum", Eur. Phys. J. C **49**, 897 (2007)

[81] D. S. Barton et al., "Experimental study of the A dependence of inclusive hadron fragmentation", Phys. Rev. D 27, 2580 (1983)

[82] A. Fasso, A. Ferrari, S. Roesler, P. R. Sala, F. Ballarini, A. Ottolenghi, G. Battistoni and F. Cerutti *et al.*,"The Physics models of FLUKA: Status and recent developments", eConf C **0303241**, MOMT005 (2003)

[83] R. Bradford, A. Bodek, H. S. Budd, and J. Arrington, "A new parameterization of the nucleon elastic form factors", Nucl. Phys. Proc. Suppl., vol. 159, pp. 127–132, 2006.

[84] R. P. Feynman, M. Kislinger and F. Ravndal, "Current matrix elements from a relativistic quark model ", Phys. Rev. D3, 2706 (1971).

[85] K. S. Kuzmin, V. V. Lyubushkin, and V. A. Naumov, "Axial masses in quasielastic neutrino scattering and single-pion neutrinoproduction on nucleons and nuclei", Acta Phys. Polon., vol. B37, pp. 2337–2348, 2006.

[86] C. Andreopoulos, A. Bell, D. Bhattacharya, F. Cavanna, J. Dobson, S. Dytman, H. Gallagher and P. Guzowski *et al.*, "The GENIE Neutrino Monte Carlo Generator", Nucl. Instrum. Meth. A **614**, 87 (2010)

[87] A. Bodek and U. K. Yang, "Higher twist, w scaling, and effective LO PDFs for lepton scattering in the few GeV region", J. Phys., vol. G29, pp. 1899–1906, 2003.

[88] M. Gluck, E. Reya, and A. Vogt, "Dynamical parton distributions revisited", Eur. Phys. J., vol. C5, pp. 461–470, 1998.

[89] R. Gran, J. Nieves, F. Sanchez and M. J. Vicente Vacas, "Neutrino-nucleus quasi-elastic and 2p2h interactions up to 10 GeV", Phys. Rev. D **88**, 113007 (2013)

[90] H. Gallagher, "The neugen neutrino event generator", Nucl. Phys. Proc. Suppl., vol. 112, pp. 188– 194, 2002.

[91] R. Luchsinger and C. Grab., "Vertex reconstruction by means of the method of Kalman filtering", Computer Physics Communications, Volume 76, Issue 3, August 1993, Pages 263–280.

[92] K. Hurtado, Master Thesis:"Calibración del detector MINERvA mediante la detección de muones", p25.

[93] MINERvA Collaboration, Design, Calibration and Performance of the MINERvA Detector, Nucl. Inst. and Meth. A743 (2014) 130.

[94] Belkov Ar. "Implementation of the Hough Transform for 3D Track Reconstruction in Drift Chambers, "Actual Problems of High Energy Physics", August 7-16, 2001.

[95] W. Fetscher and H.-J. Gerber, "Muon Decay Parameters", Particle Data Group Reviews (2011)

[96] C. Andreopoulos, A. Bell, D. Bhattacharya, F. Cavanna, J. Dobson, S. Dytman, H. Gallagher and P. Guzowski *et al.*, "The GENIE Neutrino Monte Carlo Generator", Nucl. Instrum. Meth. A **614**, 87 (2010)

[97] S. Agostinelli et. al., "Geant4 simulation toolkit", Nuclear Instruments and Methods in Physics Research Section A: Accelerators, Spectrometers, Detectors and Associated Equipment, Volume 506 Number 3 p250-303 (2003).

[98] The MINERνA Technical Design Report, Colaboración MINERνA , FERMILAB-DESIGN-2006-01, MINERVA-DOCUMENT-700, 2006. 252pp.

[99] G. D'Agostini, A multidimensional unfolding method based on Bayes' theorem, Nuclear Instruments and Methods in Physics Research Section A: Accelerators, Spectrometers, Detectors and Associated Equipment, Volume 362, Issues 2–3, 15 August 1995, Pages 487-498.

[100] D.W. Schmitz, G.A. Fiorentini, T. Le, L. Rakotondravohitra, and B.G. Tice, "Reconstruction efficiency corrections for the titan production pass", MINERvA Internal Note TN16 (2013).

[101] M. Kordosky. "Error bands from the many universes method",MINERvA Internal Note docdb-7433 (2012).

[102] J. Wolcott. "Uncertainties due to feynman scaling of na49 data to numi energy", MINERvA Internal Note 015 (2013).

[103] Geant4 Collaboration, Summary of Hadronic Processes, Models and Cross Sections for Physics List QGSP_BERT (2012).

[104] Geant4 Collaboration, Summary of Hadronic Processes, Models and Cross Sections for Physics List FTFP_BERT (2012).

[105] Ž. Pavlović, "Observation of disappearance of muon neutrinos in the NuMI beam", Ph.D. thesis, FERMILAB-THESIS-2008-59, University of Texas at Austin, (2008). 99, 100, 101 (2008).

[106] D.G. Michael et al. (MINOS collaboration). The Magnetized steel and scintillator calorimeters of the MINOS experiment. Nucl. Inst. and Meth., Phys. Res. Sect. A, 596:190–228 (2008).

[107] R. Gran., "Test Beam calorimetry note". Minerva Internal Note TN45 (2013).

[108] J. Beringer et al., Passage of particles through matter, Particle Data Group Review (2009). http://pdg.lbl.gov/2009/reviews/rpp2009-rev-passage-particles-matter.pdf

[109] T. Walton, Muon Energy Scale Systematics, Minerva Internal Note docdb-7595 (2012).

[110] B. Eberly, Birk's systematics, Minerva Internal Note 9526 (2013).

[111] R. Gran., "Birk's law parameter from minerva testbeam data". Minerva Internal Note TN37 (2013).

[112] T. Golan, J. T. Sobczyk and J. Zmuda, "NuWro: the Wroclaw Monte Carlo Generator of Neutrino Interactions", Nucl. Phys. Proc. Suppl. **229-232**, 499 (2012).

[113] K. Hurtado, Special Runs, Minerva Internal Note docdb-7067 (2012).

[114] K. Hurtado, Special Runs Update: Playlist 1,3 and 12 , Minerva Internal Note docdb-7103 (2012).

[115] K. Hurtado, Special Runs Plots for Approval, Minerva Internal Note docdb-7218 (2012).

[116] K. Hurtado, Special Runs Update: Playlist 2, Minerva Internal Note docdb-7255 (2012).

[117] K. Hurtado, Special Runs Update: pHE peaks, Minerva Internal Note docdb-7452 (2012).

[118] K. Hurtado, Applying Covariance/Correlation Matrices in our Systematic Error Classes, Minerva Internal Note docdb-7916 (2012).

[119] K. Hurtado, MnvH2D, Minerva Internal Note docdb-8463 (2012).

[120] K. Hurtado, MnvH3D, Minerva Internal Note docdb-8773 (2012).

[121] T. Adye, Unfolding algorithms and tests using RooUnfold, [arXiv:1105.1160] (2011).

[122] SVD Approach to Data Unfolding, Nucl.Instrum.Meth.A372:469-481,1996.

[123] Andreas Höcker, Vakhtang Kartvelishvili, SVD approach to data unfolding, Nuclear Instruments and Methods in Physics Research Section A: Accelerators, Spectrometers, Detectors and Associated Equipment, Volume 372, Issue 3, 1 April 1996, Pages 469-481, ISSN 0168-9002, 10.1016/0168-9002(95)01478-0.

[124] G. Cowan, A Survey Of Unfolding Methods For Particle Physics, Conf. Proc. C **0203181**, 248 (2002).

[125] K. Hurtado, Unfolding Techniques in CCQE OneTrack / CCInclusive, Minerva Internal Note docdb-8049 (2013).

[126] K. Hurtado, Unfolding Machinery update, Minerva Internal Note docdb-8084 (2013).

[127] K. Hurtado, Unfolding at Minerva, Minerva Internal Technical Note 014 (2013).

[128] "MINERvA, a neutrino nucleus interaction experiment", C.J. Solano Salinas *et al.* AIP Conf.Proc.947:239-244,2007.

[129] Particle Data Group, J. Phys. G: Nucl. Part. Phys. (2006).

[130] MINOS Collaboration, "The magnetized steel and scintillator calorimeters of the MINOS experiment", Nuclear Instruments and Methods in Physics Research Section A, Volume 596, Issue 2, p. 190-228.

Glossary

A

ASIC

Application-Specific Integrated Circuit.

C

CBPF

Centro Brasileiro de Pesquisas Físicas.

CCDIS

Charged current deep inelastic scattering.

CCQE

Charged current quasi-elastic.

CCRES

Charged current resonance.

CERN

European Council for Nuclear Research.

CRIM

CROC Interface Module.

CROC

Chain Readout Controller.

D

DAQ

Data Acquisition.

E

ECAL

Electromagnetic Calorimeter.

F

FEB

Front End Board.

FERMILAB

Fermi National Accelerator Laboratory.

G

GEANT

Geometry ANd Tracking.

GENIE

Generates Events for neutrino Interaction Experiments.

H

HCAL

Hadronic Calorimeter.

I

ID

Inner Detector.

M

MAPMT

Multi Anode Photomultipler tube.

MC

Monte Carlo.

MEC

Meson Exchange Currents.

MEU

Muon Energy Unit.

MINERVA

Main Injector Experiment $\nu - A$.

MiniBooNE

Mini Booster Neutrino Experiment.

MINOS

Main Injector Neutrino Oscillation Search.

N

NOMAD

Neutrino Oscillation MAgnetic Detector.

NOvA

NuMI Off-Axis ν_e Appearance.

NuMI

Neutrinos at the Main Injector.

O

OD

Outer Detector.

P

PCAC

Partially Conserved Vector Current.

PCI

Peripheral Component Interconnected.

PID

Particle Identification.

PMT

Photomultipler tube.

Q

QCD

Quantum Chromodynamics.

S

SRC

Short Range Correlations.

V

VME

Versa Module Europe.